Formulation of Stress Concentration Factors for Concrete-filled Steel Tubular (CFST) T- and K-joints under Various Loading Conditions

March 2019

Graduate School of Engineering

Nagasaki University

Jian ZHENG

ACKNOWLEDGEMENT

ABSTRACT

After the construction of the first concrete-filled steel tubular (CFST) arch bridge, Wangcang East River Bridge in 1990, CFST trussed arch bridges have become very popular, and more than 400 CFST arch bridges have been constructed in the last 25 years in China. Their arch ribs can be categorized into solid type and trussed type, and the latter accounts for about 38%. The trussed arch ribs consist of concrete-filled circular chords and circular hollow braces generally connected with full penetration butt welds to form CFST joint, including T-joints, Y-joints, K-joints, N-joints and so on. The filled-in concrete delays bucking of steel tube, and improves its compressive strength and ductility. However, the intersection with full penetration butt welds in CFST joint can be the weak part in the whole structure since the axial stiffness of brace is much larger than the radial stiffness of chord tube, which leads to high stress concentration around the chord-brace intersection. In fact, the fatigue cracks seriously damaging the structural safety were found in the chord-brace intersection of a half-through CFST trussed arch bridge in China. Furthermore, very limited researches have been conducted on the fatigue problem of CFST joints. Some issues of the existing researches for CFST T- and K-joints were given as follows.

(1) The existing researches considered that filled-concrete can improves the local stiffness at the chord-brace intersection of CFST T-joints and its effect can be equivalent to the increase of chord wall thickness. They proposed a determination method of the equivalent chord wall thickness to use the existing SCF formulae for circular hollow section (CHS) T-joints. However, the SCFs calculated by the method were generally larger than the experimental investigation, especially under axial compressive force in the brace. In addition, the validity range of diameter to thickness ratio of chord (2γ) in the method does not match its practical range of bridge structures. Furthermore, the influence of relative chord length (α) on SCFs is not investigated.

(2) The SCF formulae for CFST K-joints have been not proposed because of few studies devoted to the SCFs determination. Moreover, the validity ranges of diameter to thickness ratio of chord (2γ) and thickness ratio (τ) do not match the practical ranges of bridge structures.

In this dissertation, in order to simplify SCF calculations and provide a reference for fatigue evaluation of CFST T- and K-joints, the author tries to solve the problems aiming at proposing the SCFs formulae of CFST T- and K-joints under various loading condition. It is composed of six chapters as described as follows.

In Chapter 1, it gives the background and objectives of the research together with an overview of the major previous research works conducted in the related research filed. Then the layout of the dissertation is given.

In Chapter 2, a large amount of data about 119 CFST trussed arch bridges in China were collected by literature review and website investigation, first. The geometric parameters statistics on CFST K-joints were analyzed in terms of diameter ratio (β), diameter to thickness of chord (2γ), thickness ratio (τ), the eccentric ratio (ρ) and the angle (θ) between the axis of the chord and brace. The practical ranges of each key geometric parameter were provided for the numerical parameter analysis.

In Chapter 3, the published experiments relating to the studies on SCFs of CFST T-joints under axial force in the brace and in-plane bending in the brace, and the strain distribution along chord-brace intersection of CFST K-joints were outlined first. Then FE models to replicate the SCFs of CFST T-joints and the strain distribution along the intersection of CFST K-joints were developed. By comparing the experimental results with that calculated by FE analysis, the accuracy of the FE modeling to determine SCFs for CFST T- and K-joints was confirmed. The FE modeling can be provided for parametric analysis.

In Chapter 4, it focuses on the SCFs of CFST T-joints under various loading conditions. The loading conditions include that axial force in the brace, in-plane bending in the brace, out-of-plane bending in the brace and the force in the chord. Extensive parametric analyses considering the influences of diameter ratio (β), diameter to thickness of chord (2γ), thickness ratio (τ) and relative chord length (α). Then, based on the parametric analysis results, a series of SCF formulae of CFST T-joints subjected to various loading conditions were proposed as functions of key non-dimensional geometric parameters. Finally, the accuracy of the formulae was verified by comparing the SCFs obtained by the formulae and FE analysis.

In Chapter 5, the local FE models were employed to preliminary reveal the influences of key geometric parameters on SCFs of CFST K-joints under the axial forces

caused by the loading of a fatigue vehicle. The loading conditions include that basic balanced axial forces, axial compression in the chord and in-plane bending in the chord for the parametric analysis. Extensive parametric analyses considering the influences of diameter ratio (β), diameter to thickness of chord (2γ), thickness ratio (τ) and the angle (θ) between the axis of the chord and brace. Then, based on the parametric analysis results, a series of SCF formulae of CFST K-joints subjected to various loading conditions were proposed as functions of four key geometric parameters. Finally, the accuracy of the formulae was verified by comparing with the FE results.

In Chapter 6, the main conclusions of each chapter are summarized. The points that need to be conducted in the further work are also pointed out.

CONTENTS

LIST OF TABLE

LIST OF FIGURE

CHAPTER 1

Introduction

1.1 Background

After the construction of the first CFST arch bridge, Wangcang East River Bridge in 1990, CFST trussed arch bridges have become very popular, and more than 400 CFST arch bridges have been constructed in the last 35 years in China [1, 2, 3]. Their arch ribs can be categorized into solid type and trussed type, and the latter accounts for about 38% [4]. The trussed arch ribs consist of concrete-filled circular chords and circular hollow braces generally connected with full penetration butt welds to form CFST joint, including T-joints, Y-joints, K-joints, N-joints and so on. The filled-in concrete delays bucking of steel tube, and improves its compressive strength and ductility. Moreover, the CFST joints can enhance the performance of stability for the arch ribs.

However, the chord-brace intersection with full penetration butt welds in CFST joints can be the weak part in the whole structure since the axial stiffness of brace is much larger than the radial stiffness of chord tube, which leads to high stress concentration around the chord-brace intersection. The initial imperfection of weld bead around the chord-brace intersection can be another reason for the fatigue damage in CFST joints under the cyclic fatigue loading. In fact, the fatigue cracks seriously damaging the structural safety were found in the chord-brace intersection of a half-through CFST trussed arch bridge (see **Fig. 1.1**) in 2013, China, which was built in 1998 [5]. One example of the fatigue cracks is shown in **Fig. 1.2**.

In recent years, the fatigue problem of welded tubular joints in CFST structures has been highlighted and attracted extensive attentions in China [6]. However, very limited researches have been conducted on the fatigue problem of CFST joints. In addition, the Chinese code (JTG/T D65-06-2015) only gives the allowable value of nominal stress amplitude for the fatigue checking calculation of CFST joints [7]. Many research issues to be conducted still remain in the fatigue problem of CFST joints, especially the stress concentration factors (SCFs) formulae by hot spot stress (HSS) method. There has not been many studies on the SCFs formulae of CFST joints to date and the appropriate SCFs formulae for them are rarely found in literatures and design codes.

Fig. 1.1 CFST trussed arch bridge

Fig. 1.2 Fatigue crack

1.2 Literature Review

So far, many studies to evaluate the fatigue life of various types of circular hollow section (CHS) or rectangular hollow section (RHS) joints have been carried out by many researchers, such as Kuang et al. [8], Efthymiou and Durkin [9], Hellier et al. [10], Smedley and Fisher [11], Mashiri et al. [12] and Zhao et al. [13]. The evaluation methods of fatigue performance have been extensively adopted in many current national and international design codes, such as in CIDECT [14], IIW [15], API [16], AWS [17], ABS [18], DNV [19], SAA [20] and JSSC [21].

1.2.1 Evaluation methods of fatigue life

At present, the four frequently used evaluation methods of fatigue life in welded tubular joints includes that nominal stress method, HSS method, notch stress method and fracture mechanics method [22]. The nominal stress method is the most widely used since its used simplicity, but it is over-conservative. The HSS method is the most recommended method. The notch stress method and fracture mechanics method have not been adopted in the current design codes since the complex usability and great research difficulty.

The stress distribution over the plate thickness is non-linear in the vicinity of notches in welded steel joints, as shown in **Fig. 1.3** [15]. The stress components of the notch stress σ_{ln} are [23]: membrane stress σ_{mem}, shell bending stress σ_{ben} and non-linear stress peak σ_{nlp}. The membrane stress σ_{mem} is equal to the average stress calculated through the thickness of the plate, it is constant through the thickness. The shell bending stress σ_{ben} is linearly distributed through the thickness of the plate. The non-linear stress peak σ_{nlp} is the remaining component of the stress.
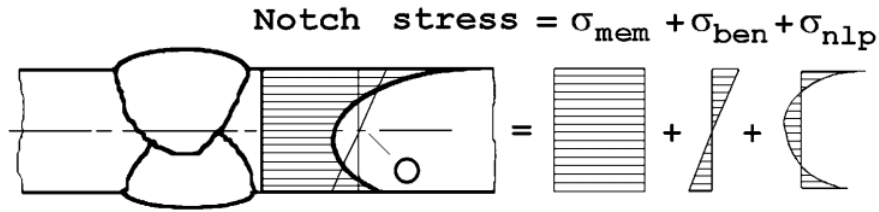
Fig. 1.3 Non-linear stress distribution separated to stress components

1.2.1.1 Nominal stress method

The nominal stress (σ_n) [24] can be calculated using the simple beam theory and the superposition principle without consideration of the localized weld effect and geometric discontinuity. It can be calculated with the plane cross-section assumption under the external loads (the axial force and bending moment) by using elementary theories of structural mechanics based on linear-elastic behavior, a simple equation is shown in Eq. (1.1). The nominal stress amplitude ($\Delta\sigma_n$) is used for the evaluation criteria of fatigue life in welded tubular joints. Then fatigue life can be evaluated by using the fatigue resistance *S-N* curves of classified structural details (*S* is the allowable value of nominal stress amplitude, N is the number of fatigue loading circles). *S-N* curves were obtained based on large numbers of fatigue experiments, the typical *S-N* curves for tubular joints in current design codes were experimentally proposed in the early 1970s [25, 26].

$$\sigma_n = \frac{P}{A} \pm \frac{M}{W} \tag{1.1}$$

Where, *P* is the applied axial force, *A* is the area of cross-section, *M* is the applied bending moment, *W* is the section modulus of cross-section.

The nominal stress method still has the following shortcomings [22].

(1) Fatigue strength determined with *S-N* curves on the basis of nominal stress is over-conservative. It adopts the most conservative *S-N* curve to evaluate the fatigue strength for the same type of tubular joints, regardless of the difference of geometric parameters. The influence of geometric parameters is neglected, which significantly underestimates the fatigue strength for some tubular joints.

(2) Value position of the nominal stress is unspecified. Van Wingerde [27] indicated that the value position of the nominal stress can be from 2*b* to 2.5*b* (*b* is width of chord or brace) away from tube end and chord-brace intersection in RHS joints. However, the corresponding provision is not given in current specifications. If the value position

selection is not proper, the evaluation of fatigue life will have large difference.

1.2.1.2 HSS method [14, 15]

The HSS (σ_h) (also called geometric stress) method relates the fatigue life of a joint to the so-called HSS at the joint rather than the nominal stress. It takes the uneven stress distribution around the perimeter of the joint into account directly. The HSS range includes the influences of the geometry and type of load but excludes the effects related to fabrication such as the configuration of the weld (flat, convex, concave) and the local condition of the weld toe (radius of weld toe, undercut, etc.). The HSS includes all stress raising effects of a structural (or geometric) detail excluding all stress concentrations due to the local weld profile itself. Therefore, as shown in **Fig. 1.3**, the membrane stress σ_{mem} and the shell bending stress σ_{ben} are included in the HSS, but the non-linear stress peak σ_{nlp} caused by the local notch, i.e. the weld toe, is excluded from the HSS.

The stress concentration factors (SCFs) for HSS can be defined as the ratio between the HSS at the joint and the nominal stress in the member due to a basic member load which caused this HSS. It has to be determined at the weld toe position from the stress field outside the region influenced by the local weld toe geometry.

The typical stress distribution along the direction perpendicular to the weld toe is shown in **Fig. 1.4**. The HSS can be determined using reference points and extrapolation method to the weld toe at the hot spot in consideration. The HSS has to be determined at the weld toe position from the stress field outside the region influenced by the local weld toe geometry. The location from which the stresses have to be extrapolated, the so-called "extrapolation region", depends on the dimensions of the joint and on the position around the intersection. The extrapolation methods for HSS calculation in tubular joints consists of linear extrapolation and quadratic extrapolation, CHS joints and RHS joints generally use linear extrapolation and quadratic extrapolation based on a lot of existing test research, respectively [22]. For joints in CHS, the linear extrapolation method can be used since the gradient is nearly linear [28]. For joints in RHS, the quadratic extrapolation method is required because of the strong non-linear strain distribution observed [27].
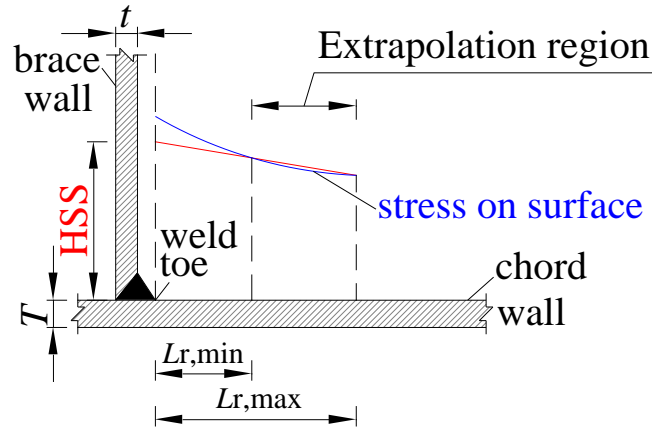
Fig. 1.4 Definition of HSS

The boundaries of extrapolation region for CHS and RHS joints defined in CIDECT Design Guide [14] are listed in **Table 1.1**. The recommendations for extrapolation in IIW [15] are summarized as follows.

(1) The stresses on two reference points $0.4T$ (t) and 1.0 T (t) are used in the linear extrapolation.

$$\sigma_h = 1.67\sigma_{0.4} - 0.67\sigma_{1.0} \tag{1.2}$$

(2) The stresses on three reference points $0.4T$ (t), $0.9T$ (t) and 1.4 T (t) are used in the quadratic extrapolation under the cases of pronounced non-linear structural stress increase to the hot spot.

$$\sigma_h = 2.52\sigma_{0.4} - 2.24\sigma_{0.9} + 0.72\sigma_{1.4} \tag{1.3}$$

The recommendations for extrapolation from Fricke [29] are summarized as follows.

(1) The stresses on two reference points $0.5T$ (t) and 1.5 T (t) are used in the linear extrapolation.

$$\sigma_h = 1.5\sigma_{0.5} - 0.5\sigma_{1.5} \tag{1.4}$$

(2) The stresses on three reference points $0.5T$ (t), $1.5T$ (t) and 2.5 T (t) are used in the quadratic extrapolation under the cases of pronounced non-linear structural stress increase to the hot spot.

$$\sigma_h = 1.875\sigma_{0.5} - 1.25\sigma_{1.5} + 0.375\sigma_{2.5} \tag{1.5}$$

Table 1.1 Boundaries of extrapolation region

Distance from weld toe		Chord		Brace
		Saddle	Crown	Saddle / Crown
CHS joints	Lr,min	\multicolumn{2}{c}{$0.4T$, but ≥ 4 mm}	$0.4t$, but ≥ 4 mm
	Lr,max	$0.045D$	$0.4\sqrt[4]{0.25DTdt}$	$0.65\sqrt{0.5dt}$
		but $\geq Lr$,min $+ 0.6t$	
RHS joints	Lr,min	\multicolumn{2}{c}{$0.4T$, but ≥ 4 mm}	$0.4t$, but ≥ 4 mm
	Lr,max	\multicolumn{2}{c}{Lr,min $+ T$}	Lr,min $+ t$

Remark: D is the diameter of chord, T is the thickness of chord, d is the diameter of brace, t is the thickness of brace.

The experimental method and Finite element (FE) analysis have been carried out to determine the HSS for tubular joints. Different views exist with regard to which stress component should be used to determine the SCF: the principal stress or a stress perpendicular to the weld toe [14]. The principal stress is used in IIW [15], Den [30] and EC3 [31], whereas the stress perpendicular to the weld toe is used in AWS [17] and API [16]. The differences between the two stresses become less significant near the weld toe [32, 33]. Strain perpendicular to the weld toe can be measured by simple strain gauges instead of strain gauge rosettes which are required to determine the principal strains. The use of stresses (strains) perpendicular to the weld toe is recommended.

The HSS method has the advantage compared with the nominal stress method [22, 34]: The HSS method can express the influences of geometric parameters on the fatigue life of tubular joints. It has different HSS range with different parametric combination under the same nominal stress range. Therefore, the HSS method has become the international mainstream method since the above advantage so as to be adopted by CIDECT, IIW, EC3, AWS, API, etc.

1.2.1.3 Notch stress method

Effective notch stress (σ_{ln}) (see **Fig. 1.3**) is the total stress at the root of a notch, obtained assuming linear elastic material behavior. To take account of the statistical nature and scatter of weld shape parameters, as well as of the non-linear material behavior at the notch root, the real weld contour is replaced by an effective one. For structural

steels and aluminium an effective notch root radius of $r = 1$ mm has been verified to give consistent results. For fatigue assessment, the effective notch stress is compared with a common fatigue resistance curve [15].

The fatigue assessment using notch stress method is similar to that under the nominal stress method or the HSS method, the notch stress range at weld toe is determined and then the fatigue life is evaluated by using the corresponding S-N curves in terms to the notch stress concept [35, 36, 37, 38]. The effective notch stress at weld toe is generally obtained by FE analysis. The HSS can be determined by the extrapolation method, but the notch stress can be directly obatained at weld toe since the influence of welding shape needs to be included [22]. Therefore, the notch stress is larger than HSS, i.e. the SCF in terms to notch stress is larger than that in terms to HSS. Van Wingerde [27] presented that the SCF in terms to notch stress under different welding type can be calculated by multiplying by the increasing coefficient on the basis of the SCF in terms to HSS.

The notch stress is difficult to calcluted with sufficient accuracy since the complexity of welding structures. The influences of the welding shape including the length, angle, radian of weld leg are difficult to obtain uniformly. Therefore, the uniform method to determine the notch stress still needs to be further improved [22].

1.2.1.4 Fracture mechanics method

Fracture mechanics principles are applicable only to fatigue if a crack or a crack-like flaw is present [39]. Fracture mechanics analysis and crack propagation simulations are conducted to evaluate the fatigue crack growth life of welded joints [40, 41, 42].

In order to assess the fatigue life based on the fracture mechanics, Paris [43] introduced the relationship between rate of crack propagation (da/dN) and range of stress intensity factor (ΔK), based on applied cyclic stress range. The Paris power law has the simple form:

$$\frac{da}{dN} = C\Delta K^n \tag{1.6}$$

$$N = \int_{a_i}^{a_f} \frac{da}{C(\Delta K)^n} \tag{1.7}$$

Where, C and n are material constants which are found experimentally by measuring the rate of growth of a crack under known loading in a simple test specimen. N is the cyclic number of fatigue life. a_i is the initial crack length. a_f is the critical crack length.

Fig. 1.5 is a schematic representation of the fatigue crack propagation. Zone I is

threshold value of ΔK approached stage, Zone II is the fatigue crack propagation, Zone III is the conditions for final fracture approached.
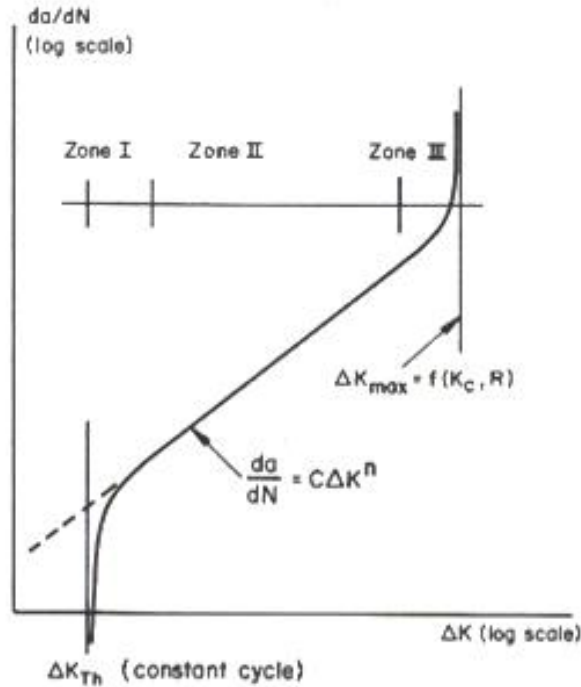
Fig. 1.5 Fracture mechanics representation

1.2.2 SCFs at typical tubular joints

The HSS method requires an accurate prediction of SCFs. Toprac and Beale [44] presented the earliest set of parametric equations to determine SCF in simple tubular joints using a limited steel joints database. During the past 50 years, several parametric equations have been proposed by many researchers for determining the HSS.

1.2.2.1 Hollow section tubular joints [22, 45]

A brief summarization of the commonly used SCF parametric equation for hollow tubular joints is illustrated in **Table 1.2**, which is provided with an emphasis on the definition of HSS and their range of applicability.

Table 1.2 SCFs parametric equations for hollow section tubular joints

Ref. No.	Joint types	Cross-section	Derived from	Time
[8, 46]	T/Y, K and KT	CHS	FEA	1975, 1977

[47, 48]	T/Y, K, X and KT	CHS	Test	1978, 1981
[9, 14]	T/Y, K and X	CHS	FEA	1985, 1988
[28]	T/Y, K, X, TT, XX and KK	CHS	FEA	1994
[49]	Space joints	CHS, RHS	FEA	1996
[50, 51]	K and Space joints	CHS	FEA	1997, 2000
[10, 52]	T/Y	CHS	FEA	1990
[53, 54]	T/Y and X	CHS	FEA	1996, 1999
[55, 56]	K and KT	CHS	FEA and Test	1997, 1998
[57, 58]	T/Y, X, K and KK	CHS, RHS	FEA and Test	1996, 2001
[59]	XX	CHS	FEA	2000
[60]	K and N	CHS	FEA and Test	2003
[61]	K	CHS	FEA and Test	2009
[27]	T/Y and X	RHS	FEA and Test	1992
[62]	K	RHS	FEA and Test	1996

On the basis of the traditional hollow section tubular joints some researchers presented various new-type joints, including CHS-RHS joints, square bird-beak joints and diamond bird-beak joints. The schematic diagrams of new-type joints are shown in **Fig. 1.6**. The summary of SCF researches on new-type joints is illustrated in **Table 1.3**.
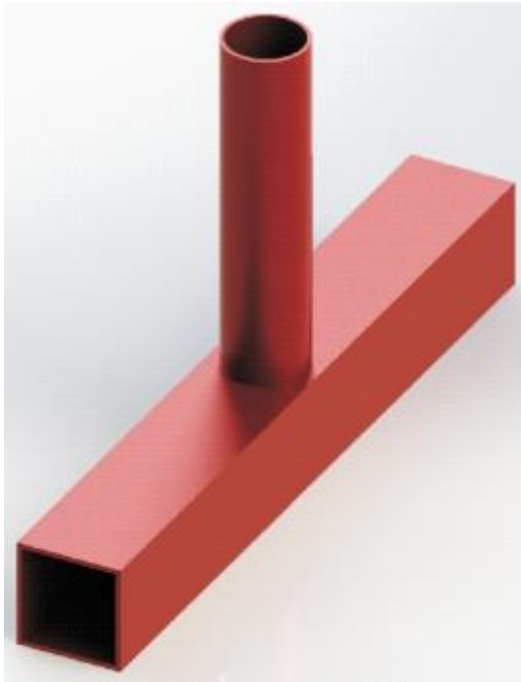
(a) CHS-RHS joint   (b) Square bird-beak joint

(c) Diamond bird-beak joint

Fig. 1.6 Structures of new-type joints

Table 1.3 Summary of SCF researches on new-type joints

Ref. No.	Joint types	Loading condition	Analysis method	Time
[63]	CHS-RHS T-joints	Axial force in brace	Test	1998
[64]		Out-of-plane bending in brace		2003
[65]		Axial force in brace, In-plane bending in brace		2003
[66]		In-plane bending in brace		2004
[67]		Axial force in brace, In-plane bending in brace	Test and FEA	2012
[68]	CHS-RHS Y-joints	Axial force in brace	FEA	2018
[69]	Square bird-beak T-joints	Axial force in brace	Test	2015
[70]			FEA	
[71]		Out-of-plane bending in brace	Test	
[72, 73]	Diamond bird-beak T-joints	Axial force in brace	Test	2014, 2016
[74]		Axial force in brace, In-plane bending in brace, Axial force in chord, In-plane bending in chord	FEA	2015

1.2.2.2 CFST joints [22]

Very limited studies have been conducted on the SCF formulae of CFST joints. Tong et al. [75] experimentally investigated the SCFs of CFST K-joints, and revealed that they have more uniform distribution and obviously smaller values than CHS K-joints.

Mashiri [76] found that the SCFs of CFST T-joint are generally lower than those of CHS T-joint under in-plane bending in the brace. By means of static test for CFST T-joints, Wang [77, 78], Chen [79, 80] and Xu [81] determined the SCFs and compared them with those estimated by some existing formulae for CHS T-joints. Udomworarat et al. [82, 83] revealed that CFST K-joints have more smaller SCFs than that in CHS K-joints by using the experimental and FE methods. Huang et al. [84] also experimentally found that CFST K-joints have significantly more uniform and with lower peak strain than those in CHS K-joints with the same geometry by comparison of their principle strain distributions around the chord-brace intersections. The filled-concrete contributing to reduce the SCFs for tubular joints was supported by some other researches on the comparison of SCFs between CFST joints and CHS joint joints with various types of tubular joints, such as in [85，86]. The summary of SCF researches on CFST joints is illustrated in **Table 1.4**. The summary of SCF researches on CFST joints stiffened with PBL is illustrated in **Table 1.5**.

Table 1.4 Summary of SCF researches on CFST joints

Ref. No.	Joint types	Loading condition	Analysis method	Time
[77-81, 87]	Circular T	Axial force in brace	Test	2008 - 2015
[88，89]		Axial force in brace, In-plane bending in brace	FEA	2014, 2015
[90]		Axial force in brace, In-plane bending in brace, Out-of-plane bending in brace	Test	1993
[91]		Axial tension in brace	FEA	2018
[6，92]	Circular Y	Axial force in brace	Test, FEA	2012, 2013
[85]	Circular N	Axial force in brace	FEA	2014
[75, 82, 83]	Circular K	Axial force in brace	Test	2000 - 2008
[76]	Rectangular T	In-plane bending in brace	Test	2010

[86]		Axial force in brace	Test, FEA	2017
[64]	Rectangular X	Axial force in brace, Axial force in chord, In-plane bending in brace, In-plane bending in chord	FEA	2003

Table 1.5 Summary of SCF researches on CFST joints stiffened with PBL

Ref. No.	Joint types	Loading condition	Analysis method	Time
[83]	Circular K	Axial force in brace	Test, FEA	2002
[93]	Rectangular T	Axial force in brace, In-plane bending in brace, Out-of-plane bending in brace	FEA	2014
[86]	Rectangular X	Axial force in brace	Test	2017
[94, 95]			FEA	

1.3 Objectives and Layout of the Dissertation

The main objective of the research carried out in this dissertation is mainly aiming to formulate the parametric formulae for determining the SCFs of CFST T- and K-joints under various loading conditions. The dissertation is composed of six chapters as described below.

In Chapter 1, it gives the background and objectives of the research together with an overview of the major previous research works conducted in the related research filed. Then the layout of the dissertation is given.

In Chapter 2, a large amount of data about 119 CFST trussed arch bridges in China were collected by literature review and website investigation, first. The geometric parameters statistics on CFST K-joints were analyzed in terms of diameter ratio (β),

diameter to thickness of chord (2γ), thickness ratio (τ), the eccentric ratio (ρ) and the angle (θ) between the axis of the chord and brace. The practical ranges of each key geometric parameter were provided for the numerical parameter analysis.

In Chapter 3, the published experiments relating to the studies on SCFs of CFST T-joints under axial force in the brace and in-plane bending in the brace, and the strain distribution along chord-brace intersection of CFST K-joints were outlined first. Then FE models to replicate the SCFs of CFST T-joints and the strain distribution along the intersection of CFST K-joints were developed. By comparing the experimental results with that calculated by FE analysis, the accuracy of the FE modeling to determine SCFs for CFST T- and K-joints was confirmed. The FE modeling can be provided for parametric analysis.

In Chapter 4, it focuses on the SCFs of CFST T-joints under various loading conditions. The loading conditions include that axial force in the brace, in-plane bending in the brace, out-of-plane bending in the brace and the force in the chord. Extensive parametric analyses considering the influences of diameter ratio (β), diameter to thickness of chord (2γ), thickness ratio (τ) and relative chord length (α). Then, based on the parametric analysis results, a series of SCF formulae of CFST T-joints subjected to various loading conditions were proposed as functions of key non-dimensional geometric parameters. Finally, the accuracy of the formulae was verified by comparing the SCFs obtained by the formulae and FE analysis.

In Chapter 5, the local FE models were employed to preliminary reveal the influences of key geometric parameters on SCFs of CFST K-joints under the axial forces caused by the loading of a fatigue vehicle. The loading conditions include that basic balanced axial forces, axial compression in the chord and in-plane bending in the chord for the parametric analysis. Extensive parametric analyses considering the influences of diameter ratio (β), diameter to thickness of chord (2γ), thickness ratio (τ) and the angle (θ) between the axis of the chord and brace. Then, based on the parametric analysis results, a series of SCF formulae of CFST K-joints subjected to various loading conditions were proposed as functions of four key geometric parameters. Finally, the accuracy of the formulae was verified by comparing with the FE results.

In Chapter 6, the main conclusions of each chapter are summarized. The points that need to be conducted in the further work are also pointed out.

Layout of this dissertation is shown in **Fig. 1.7**.
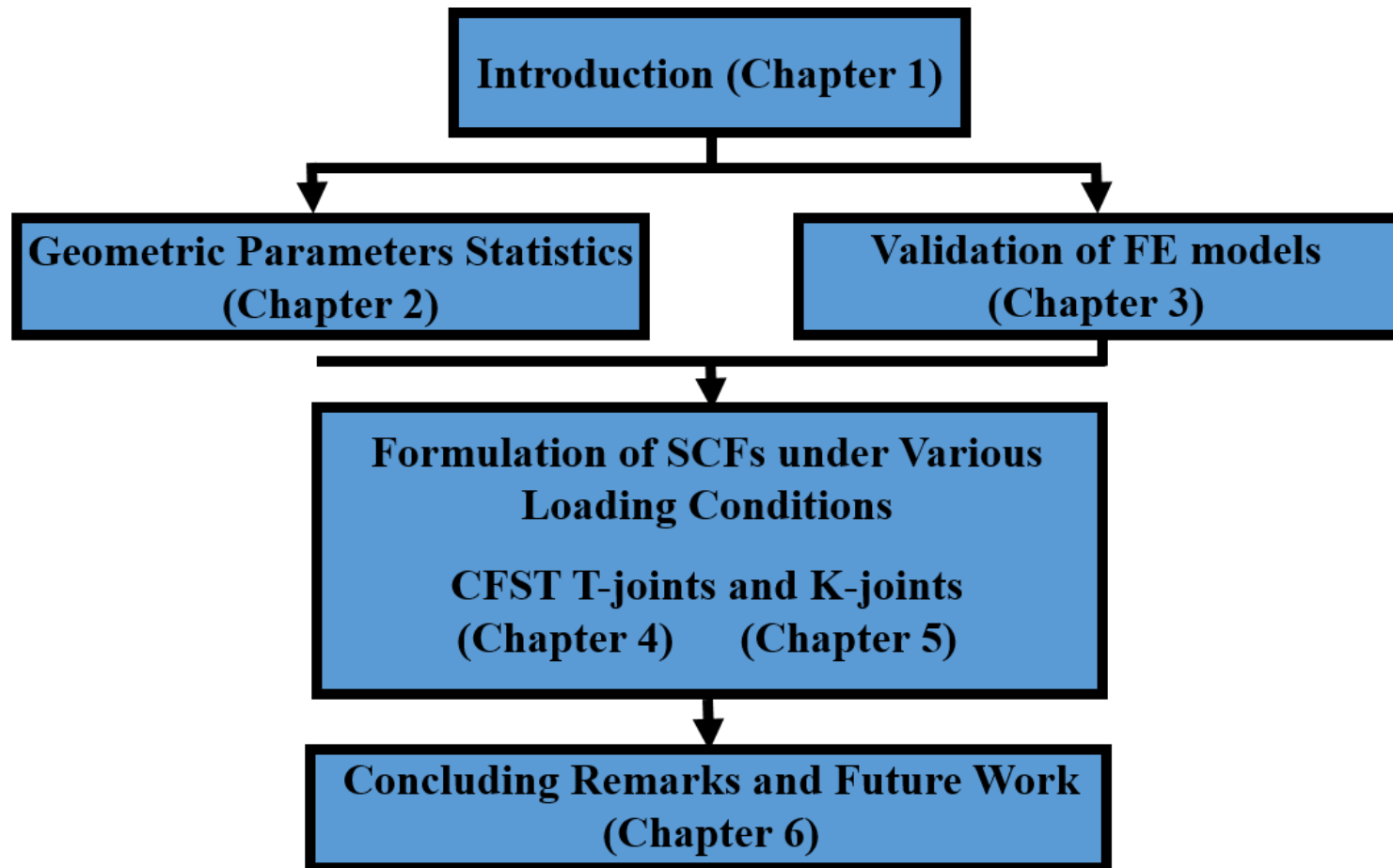
Fig. 1.7 Layout of the dissertation

CHAPTER 2

Geometric Parameters Statistics of CFST K-joints in

China

2.1 Introduction

Concrete-filled steel tubular (CFST) arch bridges have been designed and constructed for about 35 years in China since the first CFST arch bridge, Wangcang East River Bridge, was completed in 1990. Many CFST arch bridges have been constructed with various structure types by using a variety of construction methods. However, the quick construction of CFST arch bridges in China is still worth knowing of fatigue problem in the CFST joints of trussed bridges for engineers.

Fatigue life of tubular joints is commonly related to the stress concentration factors (SCFs) at the weld toes of the chord-brace intersection. So far, many existing studies mentioned in Chapter 1 for SCFs of circular hollow section (CHS) joints present that the SCFs are related to the influences of geometric parameters. Therefore, this chapter revealed the practical ranges of each key geometric parameter so as to provide the research foundation.

In this chapter, a large amount of data about 119 CFST trussed arch bridges in China were collected by literature review [96] and website investigation. The structural types of studied bridges and structural types of CFST K-joints are analyzed firstly. The geometric parameters statistics on CFST K-joints were analyzed in terms of diameter ratio (β), diameter to thickness of chord (2γ), thickness ratio (τ), the eccentric ratio (ρ) and the angle (θ) between the axis of the chord and brace. They were analyzed to demonstrate their ranges, the practical ranges of each key geometric parameter were also provided for the numerical parameter analysis.

2.2 Outline of bridges

Among 119 CFST trussed arch bridges, there are 16 deck bridges, 48 half-through bridges, 27 fly-bird bridges, 13 rigid-frame through tied bridges and 15 through arch-beam bridges. The cross-section of CFST trussed arch ribs is categorized into four-limbs, transverse dumbbell, two-limbs, three-limbs and six-limbs, as shown in **Fig. 2.1**. Their distributions are illustrated in **Fig. 2.2**. Four-limbs and transverse dumbbell are mainly used in CFST trussed arch bridges, which account for 83.2% of the total bridges.

(a) Four-limbs   (b) Transverse dumbbell

(c) Two-limbs   (d) Three limbs   (e) Six-limbs
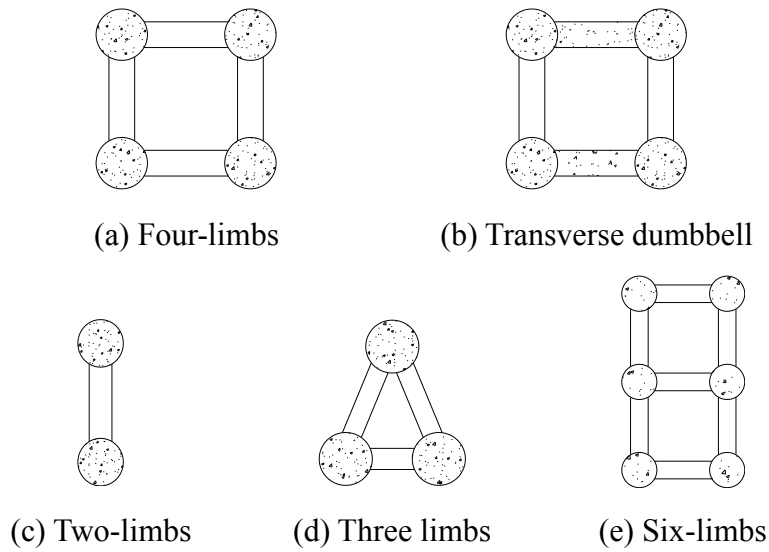
Fig. 2.1 Cross-sections of arch ribs

Transverse dumbbell
33.6%

Two-limbs
8.4%

Three-limbs
6.7%

Six-limbs
1.7%

Four-limbs
49.6%
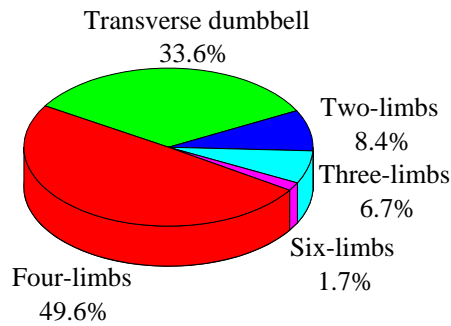
Fig. 2.2 Cross-section distributions

2.3 Structural types of CFST K-joints

The structural type of CFST joint in the bridges mainly adopted K-joints. The connection between the brace and concrete-filled chord tube are almost full penetration weld, as shown in **Fig. 2.3(a)**, which accounts for 95.8% of the total. The other two types are gusset plate bolted K-joint and full penetration welded K-joint with inner headed studs, as shown in **Fig. 2.3(b)** and **(c)**, respectively.

Since most joints are full penetration welded K-joints, the information of this joint type was used for the following analysis to demonstrate the range of each geometric parameter. Unless particularly stated in this dissertation, the studied joints are full penetration welded CFST joints.

(a) Full penetration welded K-joint   (b) Gusset plate bolted K-joint

(c) Full penetration welded K-joint with inner headed studs
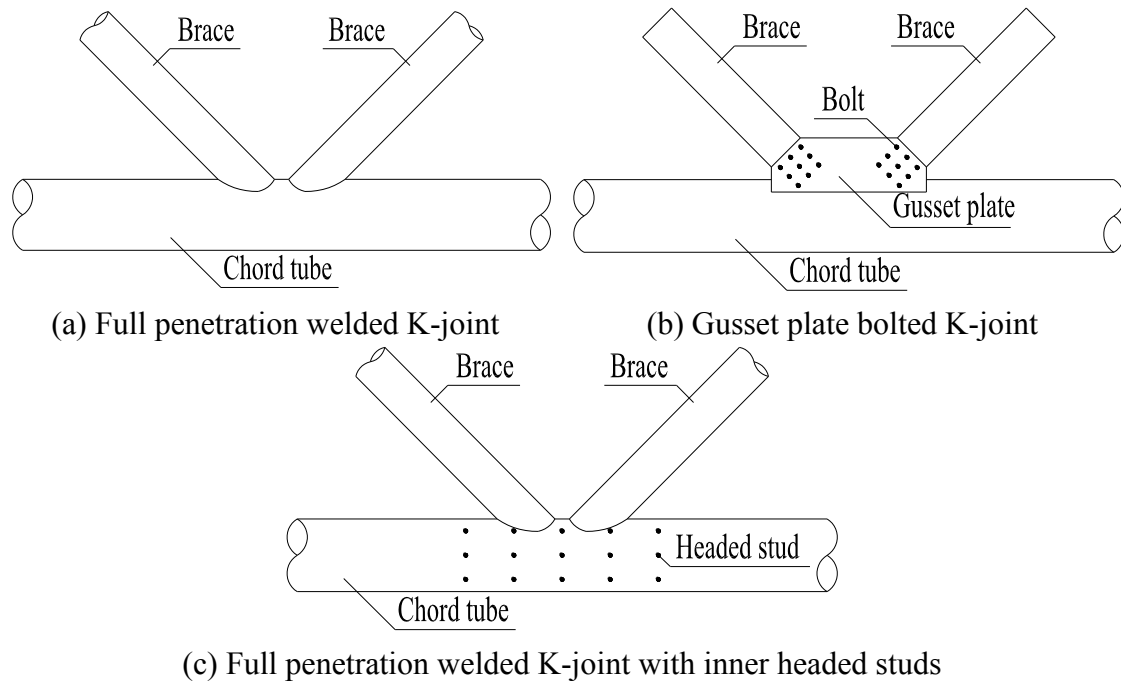
Fig. 2.3 Structural types of CFST K-joints

2.4 Geometric parameters statistics

The stress concentration factors (SCFs) of uniplanar circular hollow section (CHS) K-joints with no eccentricity and equal braces were formulated by using the diameter ratio β ($= d/D$), diameter to thickness ratio of chord 2γ ($= D/T$), thickness ratio τ ($= t/T$) and the angle θ between the axis of the chord and brace [14]. Moreover, the eccentricity ratio ρ ($= e/D$) may also affect the SCFs of tubular joints. $\rho > 0$ represents the cross-point of adjacent braces located under the axis of chord, $\rho = 0$ represents the cross-point of adjacent braces located at the axis of chord, $\rho < 0$ represents the cross-point of adjacent braces located above the axis of chord. The geometric parameters are shown in **Fig. 2.4**. Therefore, the statistical demonstration of practical ranges for geometric parameters in CFST K-joints was conducted based on the above-mentioned five non-dimensional parameters.
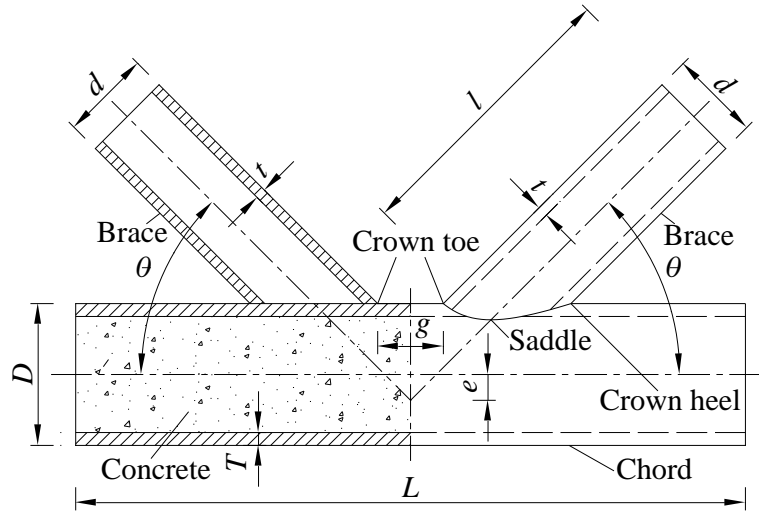
Fig. 2.4 Geometric parameters of CFST K-joints

Distributions of β-value, γ-value and τ-value are illustrated in **Figs. 2.5–2.7**, respectively. The serial number is numbered based on the above-mentioned five bridge structural types (deck type, half-through type, fly-bird type, rigid-frame through tied type and through arch-beam type) and their span length in sequence. They show that the β-value is mainly varied from 0.30 to 0.60, and the maximum and minimum β-values are 0.72 and 0.12, respectively. Moreover, $\beta = [0.3, 0.6]$ accounts for about 94%. The γ-value is mainly varied from 20 to 40, and the maximum and minimum γ-values are 42.50 and 17.14, respectively. The maximum and minimum τ-values are 1.00 and 0.40, respectively.
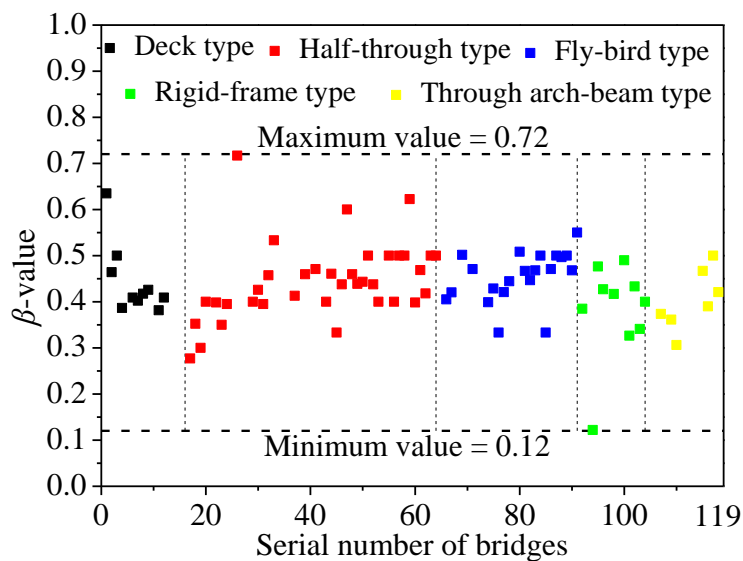
Fig. 2.5 Distribution of β-value
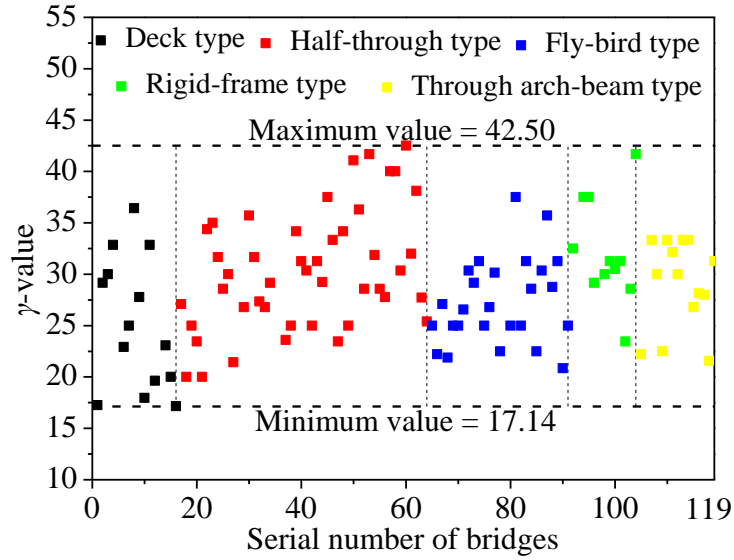
Fig. 2.6 Distribution of γ-value
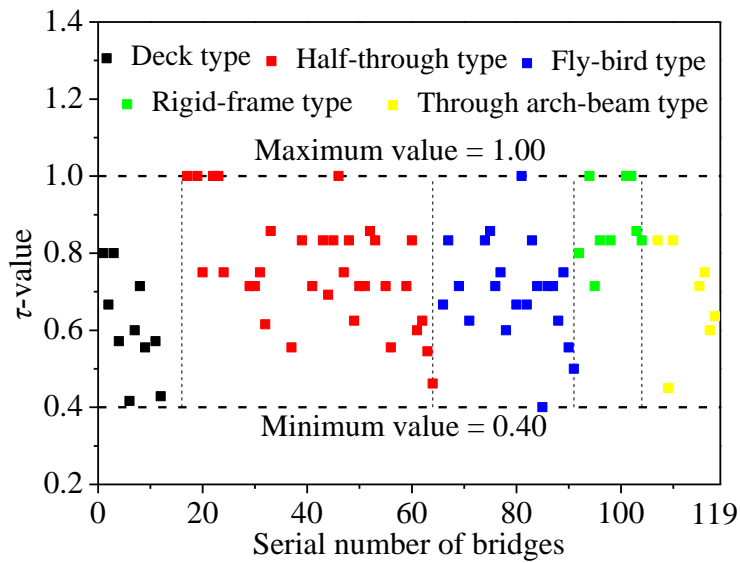
Fig. 2.7 Distribution of τ-value

For the range of θ- and ρ-values, they would be determined by relevant standard because they are not provided in the literatures. The θ-value and the angle between two axes of adjacent braces should be not less than 30° to prevent serious welding difficulties at crown heel location [97]. The maximum θ-value in the parametric formulas for CHS K-joint is 60° [14], thus the range of θ-value would be [30°, 60°]. In addition, the ρ-value would be [-0.55, +0.25] referring to the corresponding value of CHS K-joint, which should satisfy that $g \geq 2t$ [14].

2.5 Summary

The geometric parameters statistics of CFST K-joints were collected and analyzed using literature review and website investigation. The main conclusions of this work can be summarized as follows.

(1) CFST K-joints were adopted in CFST trussed arch bridges. The arch ribs can be categorized into four-limbs, transverse dumbbell, two-limbs, three-limbs and six-limbs. Four-limbs and transverse dumbbell are mainly used in CFST trussed arch bridges, which account for 83.2% of the total bridges.

(2) The structural types of CFST K-joints include that full penetration welded CFST K-joint, gusset plate bolted CFST K-joint and full penetration welded CFST K-joint with inner headed studs. Full penetration welded CFST K-joint accounts for 95.8% of the total bridges, which was regarded as the object of statistics.

(3) The practical ranges of β-, 2γ-, τ-, θ- and ρ-values are [0.3, 0.6], [40, 80], [0.4, 1.0], [30°, 60°] and [-0.55, +0.25], respectively.

CHAPTER 3

Validation of Numerical Replication for the Experimental Studies on SCFs of CFST T- and K-joints

3.1 Introduction

With the construction development of circular hollow section (CHS) structures, extensive works relating to fatigue research of CHS joints, experimental methods and numerical analysis have been conducted to determine the stress concentration factors (SCFs) for various types of CHS joints. However, very limited numerical determinations of SCFs for concrete-filled steel tubular (CFST) joints have been conducted. The SCFs of CFST joints can be influenced by many geometric parameters. The multiplicity of geometric parameters needs large amount finite element (FE) models to formulate a series of simple and widely applicable formulae for the determination of SCFs in CFST joints. Therefore, the FE modeling for CFST joints needs to be validated by comparison with the experiments first.

In this chapter, the replication of FE models to evaluate the SCFs of CFST T-joint and the principle strain distribution around the chord-brace intersection were developed first. After validating them by the comparison with existing experimental results, they would be provided for parametric analysis.

3.2 Validation of FE modeling for CFST T-joints

3.2.1 Summary of experimental studies on SCFs of CFST T-joints

Fig. 3.1 shows a schematic diagram of a CFST T-joint, the joint is made up of a hollow brace and a concrete-filled chord. T is the thickness of chord, D is the diameter of chord, t is the thickness of brace, d is the diameter of brace, L is the length of chord, l is the length of brace.
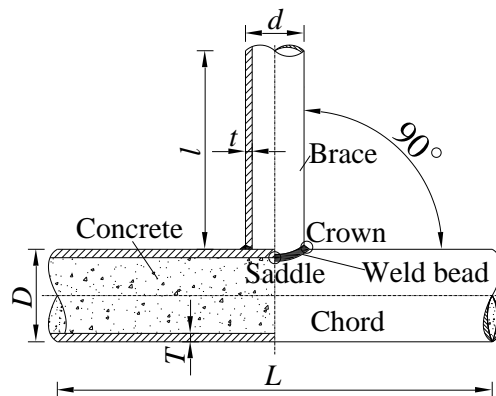
Fig. 3.1 Geometric parameters of CFST T-joints

26

The experiments to determine SCFs for CFST T-joints with different geometric parameters were carried out and published in [77, 78, 79, 80, 81]. The axial tension or compression were applied to the brace end. The published specimens subjected to the in-plane bending in the brace were also carried out. The in-plane bending around the chord-brace intersection was caused by the applied in-plane horizontal force in the brace end. The loading methods are shown in **Fig. 3.2**. One end of chord was fixed, and another end was pin-rolled in [79, 80]. Both ends of chord were fixed in [81], and pin-rolled in [77, 78].

The specimens were designed as shown in **Table 3.1** to evaluate the influence of different dimensionless geometric parameters, i.e. diameter ratio β ($= d/D$), diameter to thickness ratio of chord 2γ ($= D/T$) and thickness ratio τ ($= t/T$). The axial compressive or tensile force was applied to the hollow brace, which was fully welded at a right angle to the continuous concrete-filled chord. The static tests within elastic range were performed to obtain the HSS and the SCFs at weld toe of the specimens were determined.
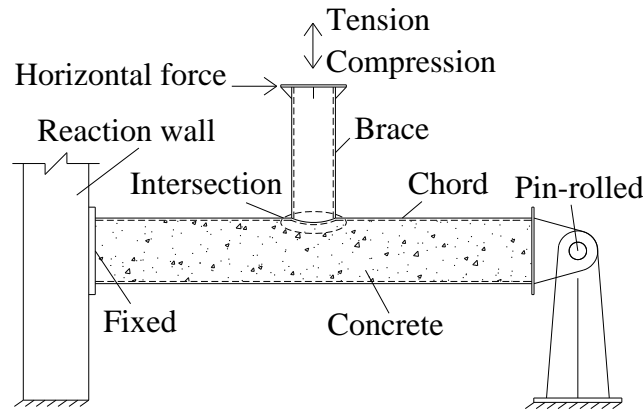
(a) Loading method in [79, 80]
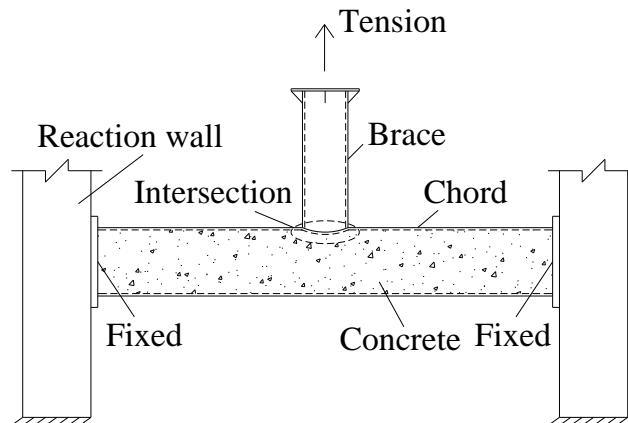
(b) Loading method in [77, 78]

27
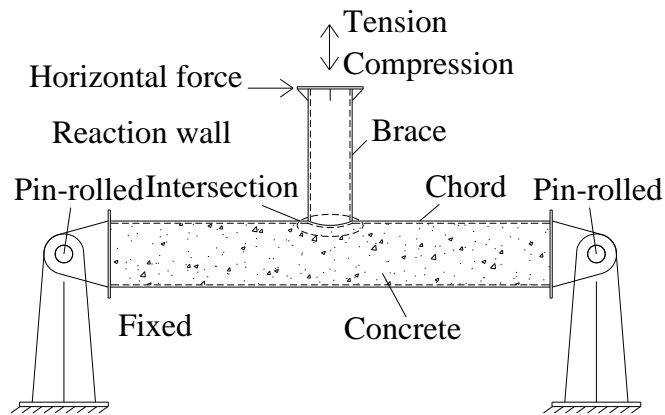
(c) Loading method in [81]

Fig. 3.2 Loading methods in literatures

Table 3.1 Details of test specimens of CFST T-joints

Ref. No.	Specimen	D (mm)	T (mm)	d (mm)	t (mm)	β	2γ	τ
[79, 80]	CS-203-133AX	203	8.45	133	6.80	0.66	24.02	0.80
	CS-203-159AX	203	8.42	159	6.81	0.78	24.11	0.81
[81]	T-300-4	299.84	4.19	132.78	6.08	0.443	75	1.5
	T-300-4R	300.11	4.18	133.25	6.08	0.443	75	1.5
	T-300-5	300.46	5.01	132.66	6.08	0.443	60	1.2
[77, 78]	CFCHS-1	245	8	133	8	0.54	30.62	1.00
	CFCHS-2	180	6	133	6	0.74	30.00	1.00
	CFCHS-3	133	4.5	133	4.5	1.00	29.56	1.00
	CFCHS-4	245	8	133	6	0.54	30.62	0.75
	CFCHS-5	245	8	133	4.5	0.54	30.62	0.56
	CFCHS-6	245	8	133	8	0.54	30.62	1.00
	CFCHS-7	245	8	133	8	0.54	30.62	1.00
	CFCHS-8	203	8	140	8	0.69	25.38	1.00
	CFCHS-9	203	10	140	10	0.69	20.30	1.00
	CFCHS-10	203	12	140	12	0.69	16.92	1.00

28

3.2.2 FE models

The general purpose FE analysis software MSC.Marc was applied for the numerical investigation on SCF distribution of CFST T-joint under axial force in the brace. Since the measured HSS was much lower than yield stress in the experiment, linear elastic analysis in terms of material properties was conducted. The values of Young's modulus and Poisson's ratio were set to those shown in the article, as summarized in **Table 3.2**.

Table 3.2 Details of test specimens of CFST T-joints

Ref. No.	Steel tube and weld bead		Concrete	
	Young's modulus (MPa)	Poisson's ratio	Young's modulus (MPa)	Poisson's ratio
[79, 80, 81]	200,000	0.3	37,420	0.2
[77, 78]	205,000	0.3	34,500	0.2

If the steel tube was modeled by shell element, it becomes difficult to model the weld bead and make good contact behavior between steel tube and concrete. Therefore, the linear full-integration eight-node hexahedron solid element was used for whole model, i.e. steel tube, concrete and weld bead. The leg sizes of weld bead at the brace and chord were set to t and $0.5t$ (t: the wall thickness of brace), respectively, according to AWS code [17].

Since the mesh size needs to be small enough to get the accurate HSS, fine mesh should be used around the intersection. The mesh dimensions of $0.5T$ to $0.5t$ around focused areas were suggested for solid element [98]. The influence of mesh size around the chord-brace intersection on the SCFs is examined in 3.2.4.

The behavior of the interface between chord tube and concrete can be simulated by "Glue" or "Touch" function. "Glue" function assumes that contact bodies tie together without any relative displacements. "Touch" function allows contact bodies to touch and separate each other in normal direction, and slide with the friction behavior in tangential direction. The function to be used is determined in 3.2.5. The whole FE model and local mesh around the intersection are shown in **Fig. 3.3**.
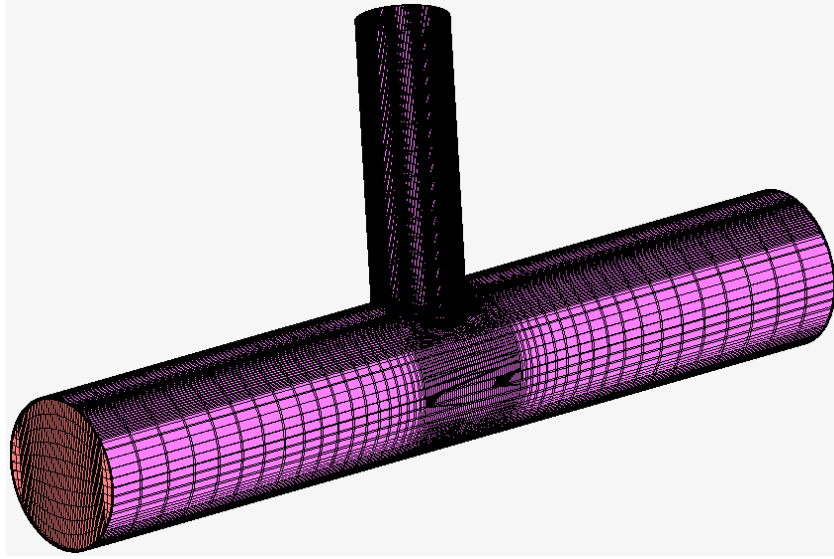
(a) FE model
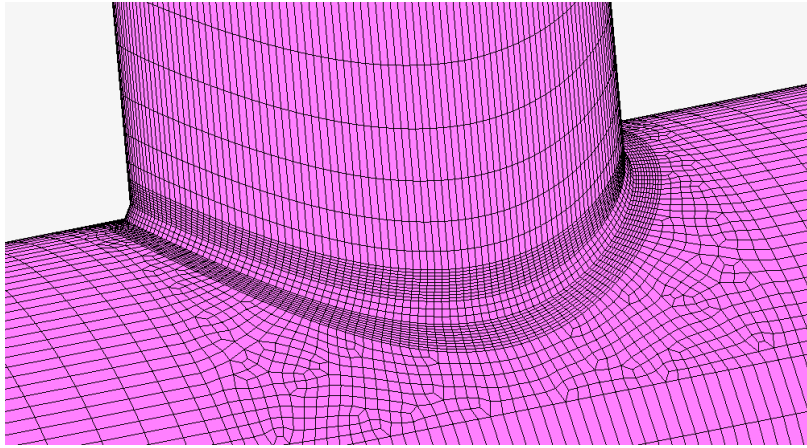
(b) Local mesh around the intersection

Fig. 3.3 FE model and local mesh of CFST T-joint

3.2.3 Hot spot stress (HSS) calculation

The HSS around the chord-brace intersection was obtained numerically by linear extrapolation. The positions of two nodes for HSS calculation is shown in **Fig. 3.4** and **Table 3.3** [14]. The positions are arbitrarily determined in this region since the stress distribution is almost linear. In this study, the positions of 1st and 2nd nodes are approximately $0.4T$ (but ≥ 4 mm) and $1.0T$ away from the weld toe, respectively. The SCF is generally defined as the ratio of the HSS at the joint to the nominal stress in the member due to the basic member load causing this HSS [14].

The nominal stress of the brace subjected to the axial force F was determined using

a simple formula ($\sigma_n = F/A$), where A is the cross-sectional area of the brace [77, 78], which was used for SCF calculation in this study. The nominal stresses under bending moment in the brace (M_b), axial compression in the chord (F_c) and bending moment in the chord (M_c) were determined as M_b/W_b, F_c/A_c and M_c/W, respectively [77, 78]. M_b is the applied bending moment in the brace, obtained as the product of the applied in-plane horizontal load F_b at the brace end and the distance from the loading point to the chord-brace intersection. W_b is the section modulus of the brace. A_c and W are the area and section modulus of the equivalent steel tube section of the concrete-filled chord, respectively.
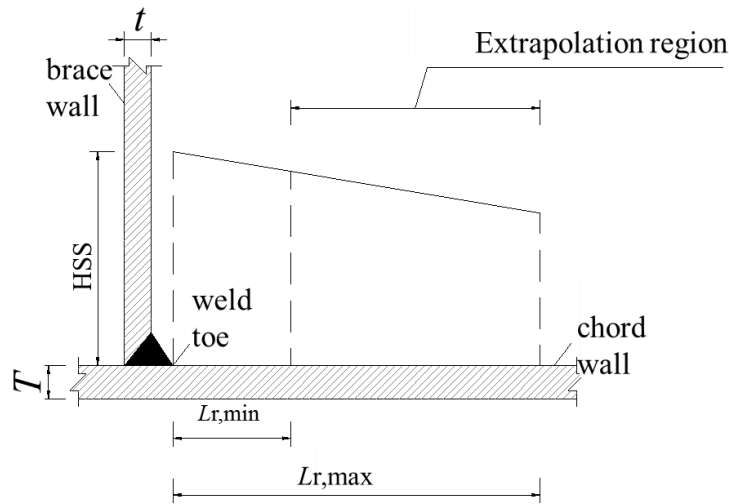
Fig. 3.4 Definition of extrapolation region

Table 3.3 Boundaries of extrapolation region

Distance from weld toe	Chord		Brace
	Saddle	Crown	Saddle / Crown
Lr,min [*)	0.4T		0.4t
Lr,max [**)	0.045D	$0.4\sqrt[4]{0.25DTdt}$	$0.65\sqrt{0.5dt}$

[*) Minimum value for Lr,min is 4mm, [**) Minimum value for Lr,max is Lr,min $+ 0.6t$.

3.2.4 Mesh size around chord-brace intersection

In order to determine the mesh size around the intersection, its influence on SCFs

was examined. The three mesh conditions listed in **Table 3.4** were considered to calculate the SCFs of CFCHS-4 specimen in [77, 78]. The influence of mesh size on SCFs for location CC under tensile or compressive axial force in the brace is shown in **Fig. 3.5**. It shows that the SCFs gradually increase as the mesh size decreases. Considering the balance between calculation accuracy and efficiency, the mesh size of approximately 2 mm was adopted in the parametric analysis.

Table 3.4 The mesh conditions

Mesh condition	Mesh size of solid element around intersection	Mesh layers in the thickness direction of steel tube
1 mm	Approximately 1 mm	Determining so that the edge length ratio of elements around the intersection is approximately 1.
2 mm	Approximately 2 mm	
$0.5T$ ($0.5t$)	4 mm (3 mm)	Two layers
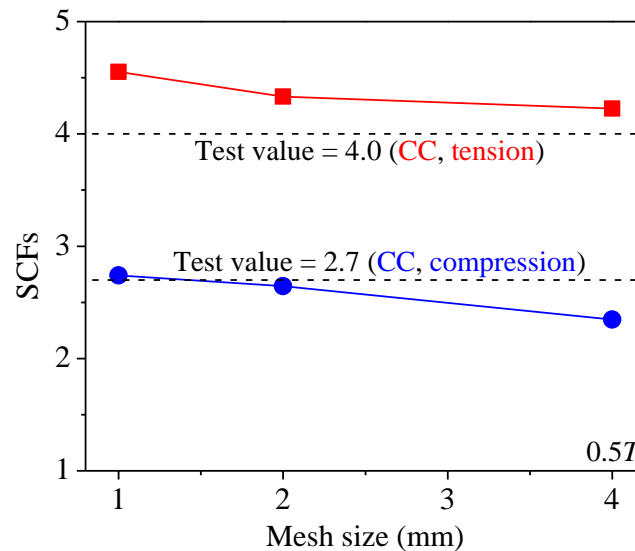
Fig. 3.5 Influence of mesh size on SCFs

3.2.5 Modeling of chord tube-concrete interface

The friction coefficient (μ) between concrete and steel is from 0.2 to 0.6 in general [99]. The SCFs at the chord crown under tensile force in the brace obtained by FE analysis with "Glue" and "Touch" functions assuming different friction coefficient in the range

are compared with the test result of T-300-4 specimen [81] in **Fig. 3.6**. It shows that the SCFs calculated with "Glue" function are much lower than test result. However, the SCFs calculated with "Touch" function show good agreement with the test result and friction coefficient has almost no influence on the SCFs. Therefore, "Touch" function with $\mu = 0.3$ was arbitrarily adopted in this study.
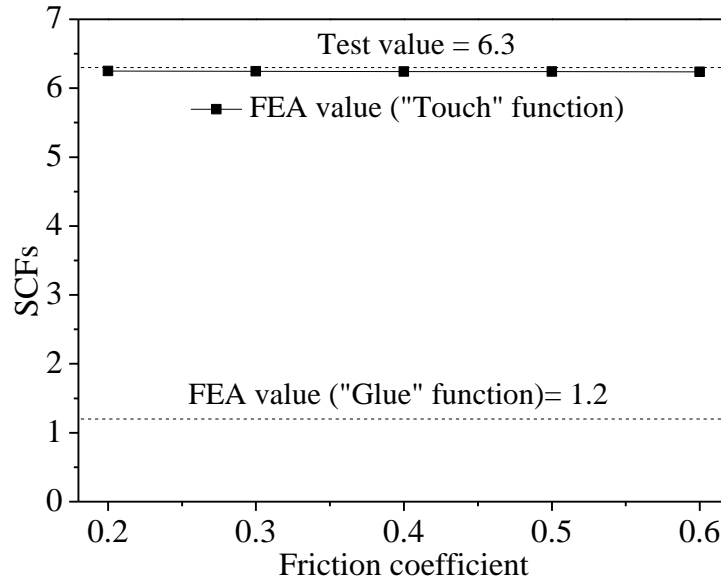
Fig. 3.6 Comparison of SCFs between "Touch" and "Glue" functions

The relative deformations between chord and concrete around the chord-brace intersection are shown in **Fig. 3.7**. It is confirmed that total cross-section of chord and concrete bears the axial force in the brace with "Glue" function, while employing "Touch" function leads to separation between chord and filled-concrete around intersection.

(a) "Glue" function   (b) "Touch" function
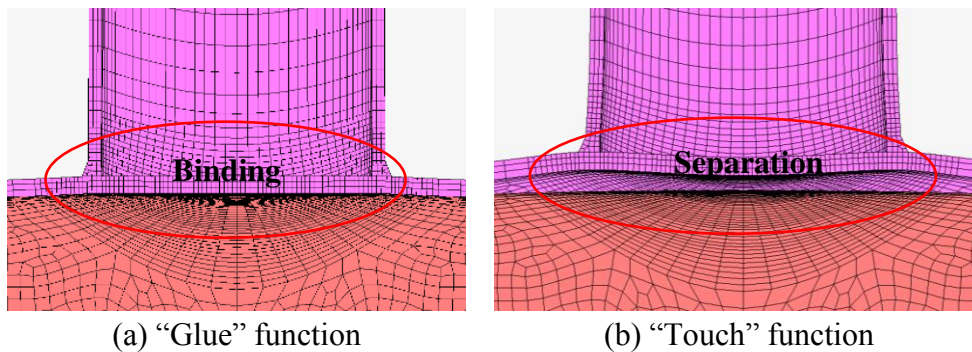
Fig. 3.7 Comparison of deformation

3.2.6 Validation of the FE models

(1) Under axial force in the brace

　　Fig. 3.8 shows a comparison of SCF distributions between FE analysis (SCF_{FEA}) and experiment (SCF_{Test}) for CFCHS-4 specimen under axial force in the brace in [77, 78]. The developed FE model reproduces not only similar distribution but also similar magnitudes in SCFs.

(a) CFCHS-4 (tension)　　　　　　　(b) CFCHS-4 (compression)
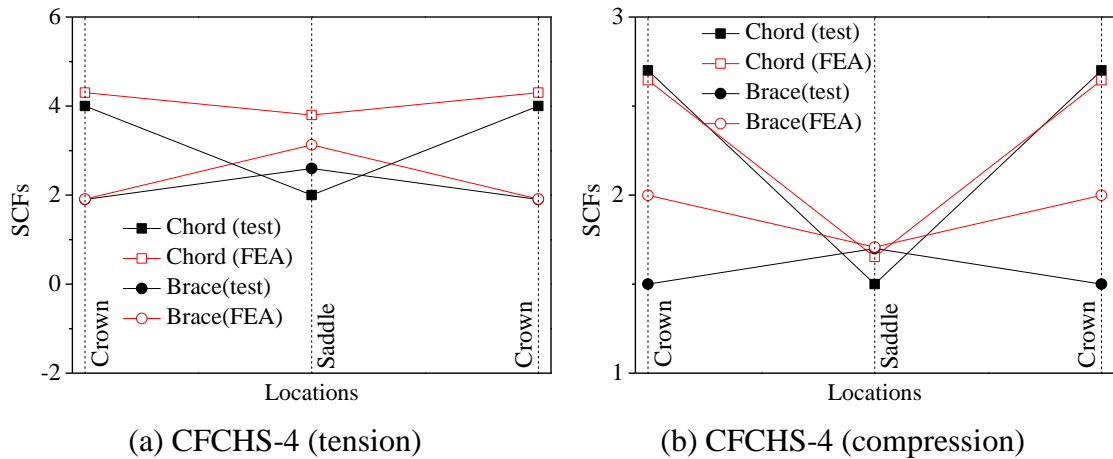
Fig. 3.8 Comparison on SCFs distribution

　　Comparisons between the SCF_{FEA} and SCF_{Test} in four locations (chord saddle CS, chord crown CC, brace saddle BS and brace crown BC) and the maximum SCFs among four locations in each specimen are shown in **Fig. 3.9** for all specimens under axial force in the brace. The averages of SCF_{FEA} to SCF_{Test} ratio of the locations CS, CC, BS, BC and maximum SCFs location under tensile condition are 1.22, 0.95, 0.98, 0.79 and 0.97, respectively, and those under compressive condition are 0.96, 0.86, 0.86, 0.68 and 0.86, respectively. The SCF_{FEA} under tensile condition shows good agreement with the SCF_{Test} although they show larger deviation under compressive condition. The external surface of filled-concrete might have much smaller Young's modulus than design value in the actual specimen due to imperfect construction such as incomplete filling and generation of laitance. It would cause the larger measured SCFs than the calculated SCFs in FE model under compressive condition. However, it would hardly affect the measured SCFs under tensile condition because of the separation between chord tube and concrete around the intersection. Consequently, such difference in deviation has occurred between tensile and compressive conditions.

34

In order to examine the influence of such imperfect construction on the SCFs, CFCHS-4 specimen was analyzed assuming 0.5 and 0.1 times of Young's modulus for the concrete elements up to approximately 10mm deep from the surface. **Table 3.5** summarizes the results. It shows the great and slight influences of imperfect construction on the SCFs under compressive and tensile conditions, respectively. In other words, larger SCFs can be obtained under compression in the test if there is such imperfect construction.

The deviation of SCF_{FEA} at location BC is large not only under compressive condition, but also under tensile condition compared with the other locations. Therefore, it can be thought that some fabrication errors exist in the brace. For example, its plate thickness or diameter is less than design value and the angle between chord and brace is not 90°.

Based on the above discussions, it can be concluded that the developed FE models can predict the SCF distribution of CFST T-joint under axial force in the brace with sufficient accuracy.

(a) CS   (b) CC

(c) BS   (d) BC
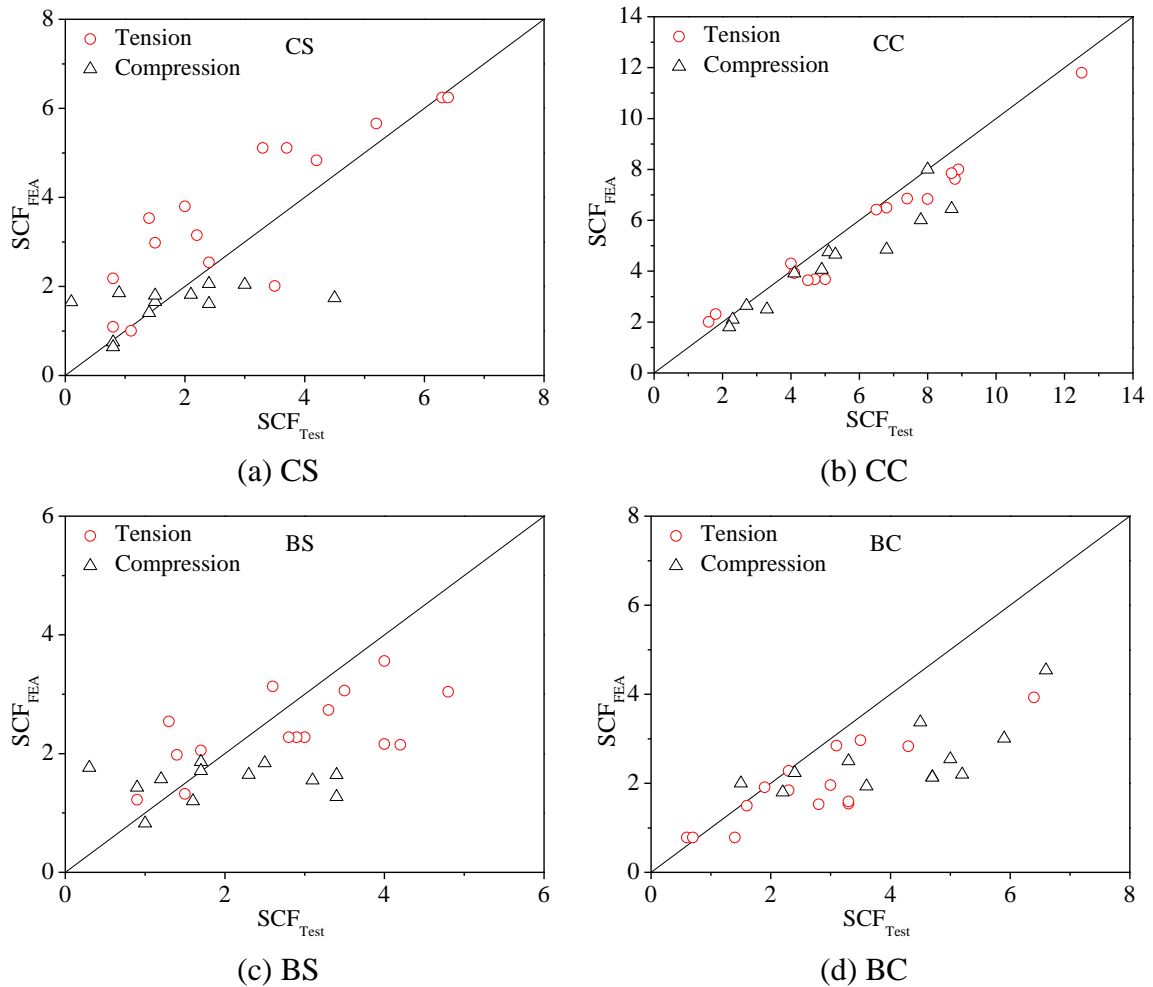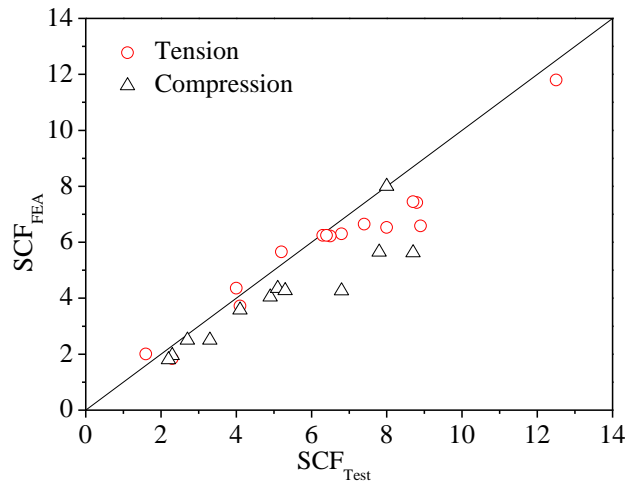
(e) Maximum SCFs

Fig. 3.9 Comparison on SCF_{FEA} with SCF_{Test} under axial force in the brace

Table 3.5 Influence of Young's modulus of concrete surface on SCFs

Young's modulus	Conditions	SCFs			
		CC	CS	BC	BS
0.1E_c	Tension	4.60	3.73	1.76	3.10
	Compression	4.05	1.98	2.58	1.75
0.5E_c	Tension	4.56	3.62	1.75	2.87
	Compression	2.98	1.56	2.16	1.48
1.0E_c	Tension	4.33	3.49	1.72	2.78
	Compression	2.44	1.38	1.97	1.43

(2) Under in-plane bending in the brace

Comparisons of SCFs at four locations (locations CC and BC on both tensile and compressive sides) between FE analysis (SCF_{FEA}) and the published tests (SCF_{Test}) are shown in **Fig. 3.10**. There is good agreement between the numerical results and the published experiments. This validates the models for the calculation of SCFs for CFST T-joints under IPB in the brace. Similar validations cannot be carried out for other loading conditions since there are no available test results with which the FE results can be compared.
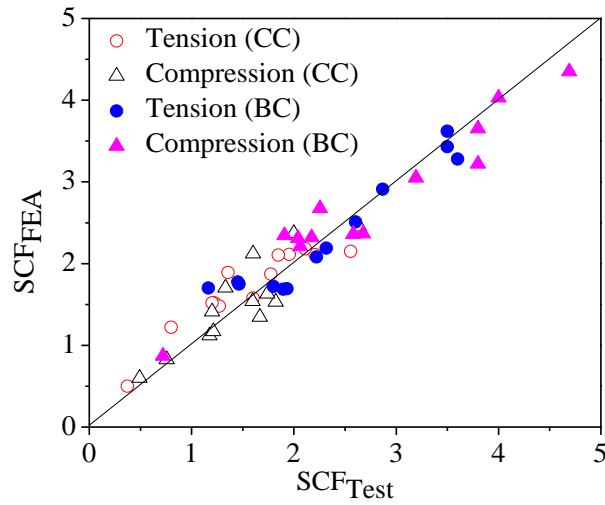
Fig. 3.10 Comparison of SCF$_{FEA}$ with SCF$_{Test}$ under in-plane bending in the brace

3.3 Validation of FE modeling for CFST K-joints

3.3.1 Summary of experimental studies

Fig. 3.11 shows a schematic diagram of a CFST K-joint, the joint is made up of two hollow braces and a concrete-filled chord. T is the thickness of chord, D is the diameter of chord, t is the thickness of brace, d is the diameter of brace, L is the length of chord, l is the length of brace, θ is the angle between the axis of the chord and brace. Moreover, e is the eccentricity between the cross-point of the adjacent brace axis and the chord axis, g is the gap between crown toes of adjacent braces.
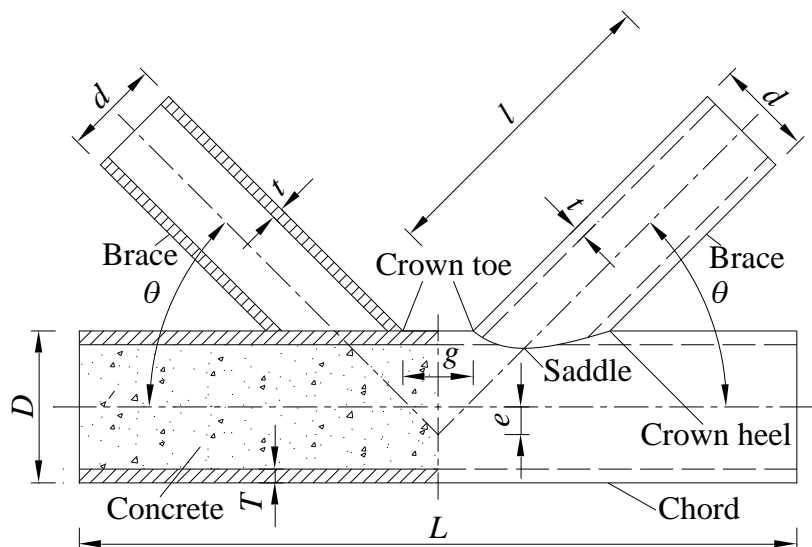
Fig. 3.11 Geometric parameters of CFST K-joints

The experiments to investigate the SCF distribution along chord-brace intersection of CFST K-joints were carried out in Zhejiang University and published in [81]. The geometry and material properties of CFST K-joints specimens are listed in **Table 3.6**. The weld profile with full penetration was determined and specimen preparation was carried out in accordance with the American Welding Society (AWS) specification [17]. They were tested with one brace in axial tension, while another brace was fixed on the test rig by bolts in the end. Both ends of the chord were fixed by bolts for all test specimens. The loading method is shown in **Fig. 3.12**.

The specimens were loaded within elastic range to obtain the SCF distribution along the brace-chord intersections. Strain gauges were placed around the intersection to measure the strains perpendicular and parallel to the weld toe in the test specimens. The arrangement of strain gauges followed the linear extrapolation region recommended by CIDECT Design Guide [14]. The measured strains were used to determine hot spot strains, which were converted to the SCFs based on the provision in [16].

Table 3.6 Geometry and material properties of CFST K-joints specimens

Geometry										
	Chord			Brace			Geometric parameters			
Specimen	Steel grade	D (mm)	T (mm)	Steel grade	d (mm)	t (mm)	θ (deg.)	β	2γ	τ
K-300-4	Q235	300.24	4.18	Q345	132.71	6.08	45	0.443	75	1.5
K-300-4R	Q235	300.11	4.18	Q345	133.25	6.08	45	0.443	75	1.5
K-300-5	Q235	300.32	5.02	Q345	132.98	6.06	45	0.443	60	1.2
Material properties										
Material		Young's modulus (MPa)			Poisson's ratio					
Steel	Q235	197000			0.3					
	Q345	199000			0.3					
Concrete		37420			0.2					
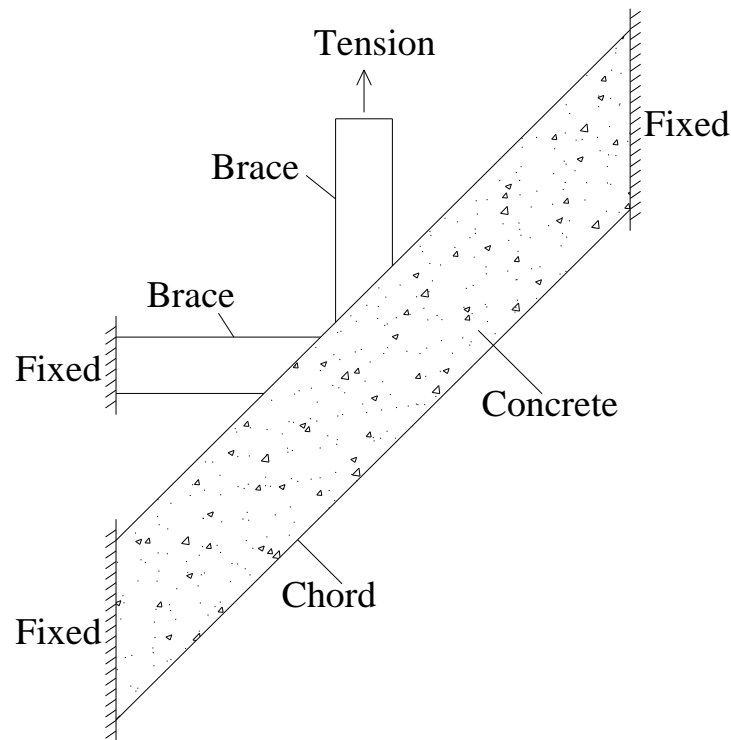
Fig. 3.12 Test loading method

3.3.2 FE models

The numerical replication on SCF distribution around the chord-brace intersection of CFST K-joint specimens was carried out with FE analysis software MSC.Marc. The analysis assuming the linear elastic material and nonlinear contact properties was executed to replicate the experiments. Whole components, i.e. steel tube, filled-concrete and weld bead, were modelled by eight-node hexahedron solid element with the function of "assumed strain", which can avoid the one order element shear locking caused by full-integration. The axial tension were applied to the end in the vertical brace. The material properties in the verification models are given in **Table 3.6**.

The dimensions of weld leg were set to t and $0.5t$ on the brace and chord sides, respectively, according to AWS specifications [17]. Around the chord-brace intersection, edge length of the elements was set to approximately 2 mm. The tubes were divided into elements in the thickness direction so as to make their edge length ratio approximately 1. These mesh specifications and generation process around the intersection are validated for the calculation of HSS around the intersection of CFST T-joints. Around the intersection in the models with full penetration welds, elements of weld bead share the

nodes on interfacing areas with the elements of both chord and braces.

"Touch" function was employed for the simulation of the contact behavior between steel pipe and in-filled concrete in the verification models, which allows them to touch and separate each other in normal direction, and to slide with friction behavior in tangential direction. In a structural analysis of MSC.Marc [100], "touch" function triggers the local application of a nonpenetration constraint still allowing relative sliding of the contact bodies in the contact interface. The nonpenetration constraint is applied through a tying or boundary condition on the displacement components normal to the contact surfaces. No bonding force between contact bodies was assumed in separation. The friction coefficient (μ) between concrete and steel is from 0.2 to 0.6 in general [99], and it does not significantly change the HSS around the intersection of CFST T-joints. Therefore, it was arbitrarily set to 0.3 as the previous study.

Fig. 3.13 shows the FE meshes of whole model and mesh details around the intersection. The ends of concrete-filled chord and horizontal brace are fixed. "RBE2" function in MSC.Marc was adopted to set the boundary conditions and loads, which defines a rigid kinematic link between a single retained node with dependent degrees of freedom specified at an arbitrary number of tied nodes [101]. The tied nodes are the nodes at the end of tube, and the retained node is the independent one at the center of the tube end section. The boundary conditions and loads were directly applied to the retained node.
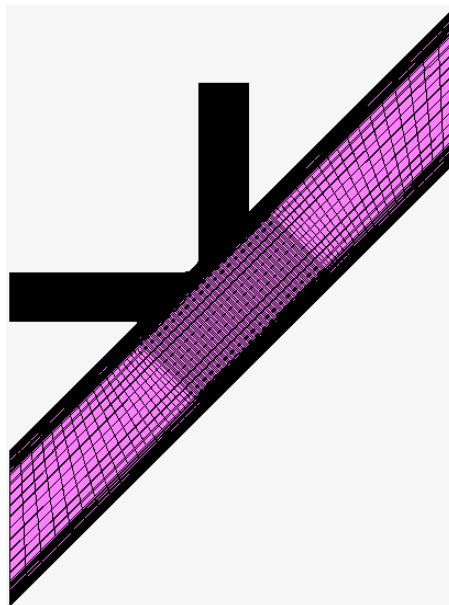
(a) FE model
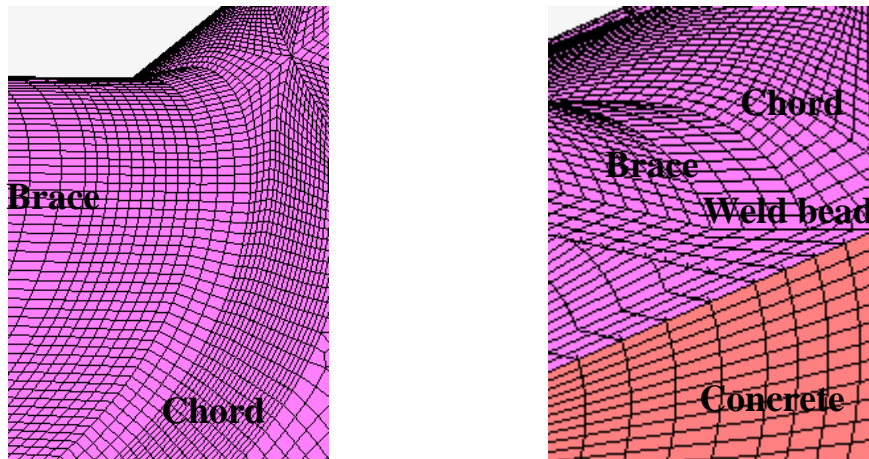
(b) Local mesh of steel tube around crown toe　(b) Local mesh around crown toe

Fig. 3.13 FE model and local mesh of CFST K-joint

3.3.3 Comparison of FE results with the experimental ones

The calculated methods of SCF in the FE replication are the same as those in the tests [81]. The comparison of SCF between the experimental and FEA results is shown in **Table 3.7**. The difference from -27% to +50% can be observed between FEA and test results. Except the SCFs at chord saddle in K-300-4 and at brace crown toe in K-300-4R, the differences are not more than 20%. When comparing the SCFs between specimens K-300-4 and K-300-4R having the same geometric parameters, the SCFs at chord show 33% difference. It indicates that such amount of difference in SCFs can occur even in the experiment due to some kinds of errors. Considering this fact, it can be thought that the FEA relatively well reproduce the test results.

To sum up in conclusion, combined with the finding that the FE modelling has sufficient accuracy to evaluate the SCFs of CFST T-joints under axial loading in the brace in the previous section, it can be thought that the FE modelling is also applicable to the evaluation of SCFs distribution of CFST K-joints.

Table 3.7 Numerical SCFs and comparison with experimental ones

Specimen		SCFs		
		Chord saddle	Brace crown toe	Brace saddle
K-300-4	Test	2.4	2.0	0.9
	FEA	3.6	1.6	0.9
K-300-4R	Test	3.2	2.2	1.1
	FEA	3.6	1.6	0.9

K-300-5	Test	3.9	2.1	1.3
	FEA	3.8	1.7	1.1

3.4 Summary

The validity of the developed FE models to determine the SCFs of CFST T-joints and the principle strain distribution around the intersection of CFST K-joints was evaluated by comparison with the existing experimental results. The main conclusions of this work can be summarized as follow.

(1) Since the measured HSS was much lower than yield stress in the experiment, the linear elastic analysis in terms of material properties in FE analysis was conducted to determine the HSS of CFST T- and K-joints.

(2) The linear full-integration eight-node hexahedron solid element was used for the whole model, i.e. steel tube, concrete and weld bead.

(3) The mesh size of approximately 2 mm was adopted for the elements around the chord-brace intersection. The number of element layers in the tube thickness direction were determined so that the edge length ratio of elements around the intersection is approximately 1.

(4) "Touch" function with the friction coefficient ($\mu = 0.3$) between concrete and steel was adopted to simulate the interface behavior between chord tube and concrete, which allows contact bodies to touch and separate each other in normal direction, and slide with the friction behavior in tangential direction.

(5) The HSS around the chord-brace intersection was obtained numerically by linear extrapolation, the positions of two nodes for HSS calculation of 1st and 2nd nodes are determined based on the specification in CIDECT Design Guide.

CHAPTER 4

Formulation of SCFs for CFST T-joints under Various Loading Conditions

4.1 Introduction

Very limited studies have been conducted on the SCF formulae of CFST T-joints. Mashiri [76] found that the SCFs of CFST T-joint are generally lower than those of CHS T-joint under in-plane bending in the brace. By means of static test for CFST T-joints, Wang [77, 78], Chen [79, 80] and Xu [81] determined the SCFs and compared them with those estimated by some existing formulae for CHS T-joints.

Wang [78] and Chen [80] considered that filled-concrete can improves the local stiffness at the chord-brace intersection of CFST T-joints and its effect can be equivalent to the increase of chord wall thickness. They proposed a determination method of the equivalent chord wall thickness to use the existing SCF formulae for CHS T-joints. However, the SCFs calculated by the method were generally larger than the experimental investigation, especially under axial compressive force in the brace. In addition, the validity range of diameter to thickness ratio of chord (2γ) in the method does not match its practical range of bridge structures. Furthermore, the influence of relative chord length (α) on SCFs is not investigated. Although any bending moment in the brace is generally small and the SCFs associated with forces in the chord are minor, parametric SCF formulae for these loading conditions, which can be treated as supplementary in the overall fatigue design of CFST T-joints, are also necessary for accurate evaluations.

In this chapter, the validated FE modeling was provided for the parametric analysis of SCFs for CFST T-joint (see **Fig. 4.1**) under various loading conditions. Then, based on the parametric analysis results, SCF formulae of CFST T-joints subjected to various loading conditions were proposed as functions of key non-dimensional geometric parameters. Finally, the accuracy of the formulae was verified by comparing the SCFs obtained by the formulae and FE analysis.

(a) Three-dimensional diagram   (b) Geometric parameters
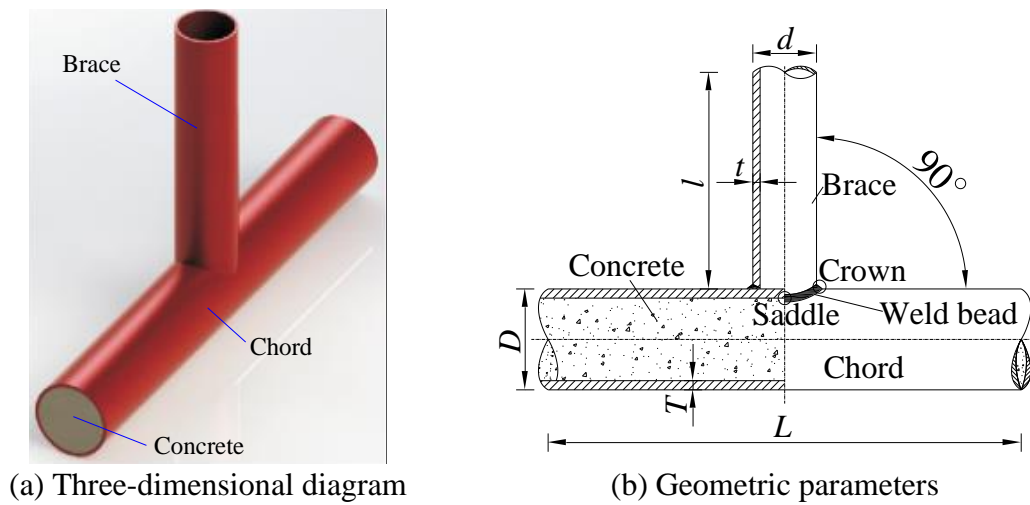
Fig. 4.1 Geometric parameters of CFST T-joints
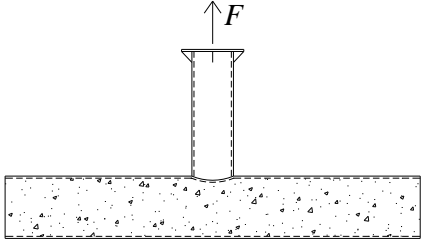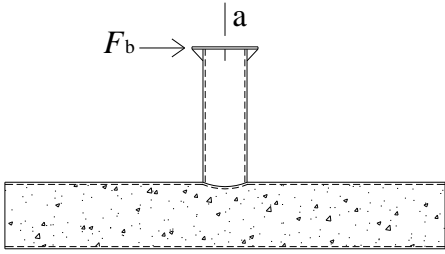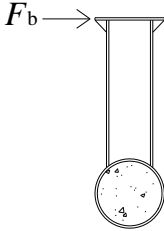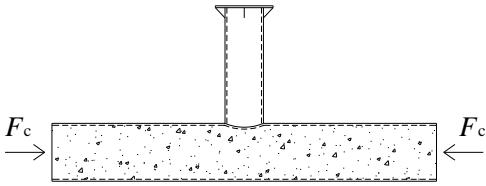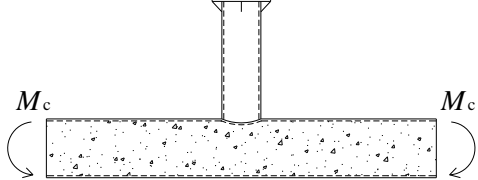
4.2 Description of parametric analysis on SCFs

4.2.1 Loading conditions

Six loading conditions were taken into account for parametric analysis referring to those for CHS T-joints in [14]: (1) axial tension in the brace; (2) axial compression in the brace; (3) in-plane bending (IPB) in the brace; (4) out-of-plane bending (OPB) in the brace; (5) axial compression in the chord; (6) IPB in the chord.

When subjected to axial tension or compression in the brace, the hot spot can occur at chord crown (CC), chord saddle (CS), brace crown (BC) or brace saddle (BS). When subjected to IPB in the brace, the hot spot always occurs at the location CC or BC, while the SCFs at the location CS and BS are very small. Under OPB in the brace, the hot spot always occurs at the CS or BS, while the SCFs at the CC and BC were very small. IPB and axial compression in the chord always induced the hot spot at the CC, while the SCFs at the CS, BC and BS were very small. SCFs were calculated at these maximal locations. The loading conditions and their associated hot spot locations are shown in **Table 4.1**. The values of F, F_b, F_c and M_c in Table 1 are 20 kN, 1000 N, 1×10^6 N and 1×10^8 N·mm, respectively.

Table 4.1 Loading conditions and their hot spot locations

Loading condition	Hot spot locations
 Axial force in the brace	CC, CS, BC and BS
 In-plane bending in the brace	CC, BC
 a-a Out-of-plane bending in the brace	CS, BS
 Axial force in the chord	CC
 In-plane bending in the chord	CC

4.2.2 FE models

The general-purpose FE analysis software MSC.Marc was used in the numerical investigation. Linear elastic analysis in terms of material properties was applied. The settings used in the FE models for the element types, the mesh specifications and generation process, and the modeling of the chord tube-concrete interface are the same as in Chapter 3. The leg sizes of weld bead at the brace and chord were set to t and $0.5t$ (t: the wall thickness of brace), respectively, according to AWS code [17].

Young's modulus of steel tube and concrete were set to 2.05×10^5 MPa and 3.45×10^4 MPa, and their Poisson's ratio were set to 0.3 and 0.2, respectively. Wang [77] experimentally presented that the effect of concrete strength on the SCFs of CFST T-joints was not significant, even can be neglected. Since concrete with the strength between 30 and 60 MPa has been applied to the arch ribs of CFST arch bridges in China [4], the concrete of 50 MPa grade was assumed for the determination of Young's modulus of concrete [102]. In addition, the chord is assumed to be simply supported and chord torsion is fixed in all FE models. The whole FE model and local mesh around the intersection are shown in **Fig. 4.2**.

Based on the SCF formulae of CHS T-joints [14] and the existing experimental results [77, 79, 81], the diameter ratio β ($= d/D$), diameter to thickness ratio of chord 2γ ($= D/T$), thickness ratio τ ($= t/T$) and relative chord length α ($= 2L/D$) are considered to be the key parameters to determination of SCFs for CFST T-joints under axial force in the brace. The parameters β, 2γ and τ are the key to determination of SCFs for CFST T-joints under IPB in the brace and under axial compression and IPB in the chord. However, parameter α is considered to be an additional key parameter when the brace is subjected to OPB. Therefore, for cases where there were IPB in the brace, axial compression and IPB in the chord, parameters β, 2γ and τ were changed but parameter α was kept constant ($\alpha = 12$). Meanwhile, when the model was subjected to axial force in the brace and OPB in the brace, parameters β, 2γ, τ and α were all varied. Ranges of non-dimensional parameters for the parametric analysis were set to $\beta = [0.3 - 0.6]$, $2\gamma = [40 - 80]$ and $\tau = [0.4 - 1.0]$, which were determined based on geometric parameter statistics of CFST K-joints in 119 CFST trussed arch bridges in China based on the statistics results in Chapter 2. Parameter α was set to $[12 - 20]$ and $[8 - 16]$ under axial force in the brace and OPB in the chord, respectively. Length (l) was unchanged during the parametric analysis at $3d$.

The geometric dimensions of standard FE model, which was set referring to the common dimensions of CFST trussed arch bridges [4], are shown in **Table 4.2**. Two hundred and twelve FE models with different combination of geometric parameters were prepared and analyzed.

<p align="center">**Table 4.2** Geometric parameters of standard FE model</p>

Structural dimensions					
D/mm	d/mm	T/mm	t/mm	L/mm	l/mm
600	300	12	12	3600	900
Non-dimensional geometric parameters					
β		2γ		τ	α
0.5		50		1.0	12

4.2.3 HSS calculation and definition of SCFs

The determination method of HSS around the chord-brace intersection was obtained numerically by linear extrapolation. The boundaries of extrapolation region is same to the description in Chapter 3. The SCF is generally defined as the ratio of the HSS at the joint to the nominal stress in the member due to the basic member load causing this HSS [14]. Therefore, the nominal stress of the brace subjected to the axial force F was determined using a simple formula ($\sigma_n = F/A$), where A is the cross-sectional area of the brace. The nominal stresses under bending moment in the brace (M_b), axial compression in the chord (F_c) and bending moment in the chord (M_c) were determined as M_b/W_b, F_c/A_c and M_c/W, respectively. M_b is the applied bending moment in the brace, obtained as the product of the applied load F_b at the brace end and the distance from the loading point to the chord-brace intersection. W_b is the section modulus of the brace. A_c and W are the area and section modulus of the equivalent steel tube section of the concrete-filled chord, respectively.

4.3 Results and discussions

4.3.1 Influence of diameter ratio β

(1) Under axial force in the brace

The influences of β on SCFs under axial force in the brace are illustrated in **Fig. 4.2**.

For the location CS (**Fig. 4.2 (a)**), the SCF_{CS} decreases as the value of β increases under tensile force. However, under compressive force, it increases for larger values of β.

For the location CC (**Fig. 4.2 (b)**), the SCF_{CC} increases as the value of β increases under tensile and compressive force.

For the location BS (**Fig. 4.2 (c)**), the SCF_{BS} decreases as the value of β increases from 0.3 to 0.5 under tensile force, but it increases as the value of β increases from 0.5 to 0.6. Moreover, it increases as the value of β increases under compressive force.

For the location BC (**Fig. 4.2 (d)**), the SCF_{BC} decreases as the value of β increases under tensile force. However, the influence of β on SCF_{BC} is not significant under compressive force.

(a) SCF_{CS} vs. β

(b) SCF_{CC} vs. β

(c) SCF$_{BS}$ vs. β

(d) SCF$_{BC}$ vs. β

- ○ - 2γ=40, τ=0.4, α=12
- □ - 2γ=40, τ=0.7, α=12
- △ - 2γ=40, τ=1.0, α=12
- ● - 2γ=60, τ=0.4, α=12
- ■ - 2γ=60, τ=0.7, α=12
- ▲ - 2γ=60, τ=1.0, α=12

- ⊕ - 2γ=80, τ=0.4, α=12
- ⊞ - 2γ=80, τ=0.7, α=12
- ⍙ - 2γ=80, τ=1.0, α=12
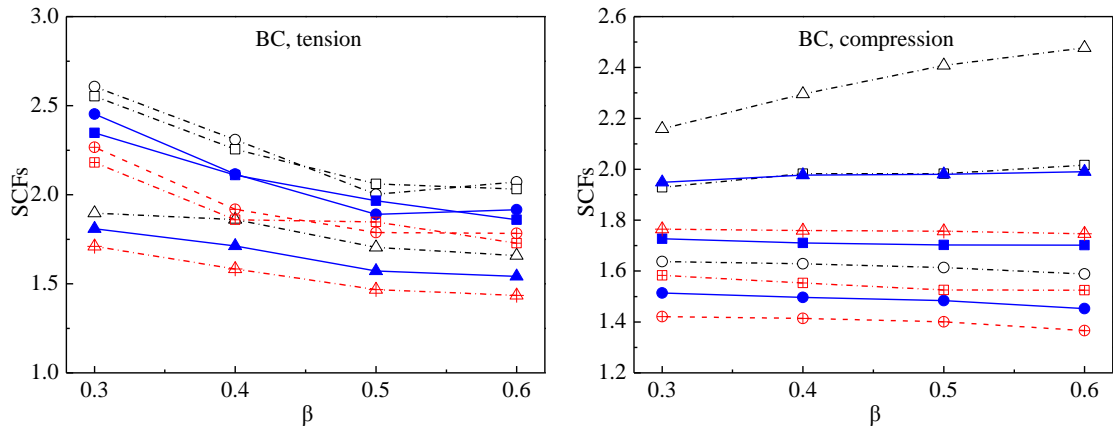
Fig. 4.2 Influence of β on SCFs under axial force in the brace

(2) Under IPB in the brace

The influences of β on SCFs under IPB in the brace are illustrated in **Fig. 4.3**.

For the location CC (**Fig. 4.3(a)**), SCFs decreases as the value of β increases at tensile side as well as compressive side.

For the location BC (**Fig. 4.3(b)**), SCFs decreases as the value of β increases at tensile and compressive sides.

(a) SCF$_{CC}$ vs. β

(b) SCF$_{BC}$ vs. β

- $\circ$ - 2γ=40, τ=0.4, α=12
- $\square$ - 2γ=40, τ=0.7, α=12
- $\triangle$ - 2γ=40, τ=1.0, α=12
- $\bullet$ - 2γ=60, τ=0.4, α=12
- $\blacksquare$ - 2γ=60, τ=0.7, α=12
- $\blacktriangle$ - 2γ=60, τ=1.0, α=12

- $\oplus$ - 2γ=80, τ=0.4, α=12
- $\boxplus$ - 2γ=80, τ=0.7, α=12
- $\triangle$ - 2γ=80, τ=1.0, α=12

Fig. 4.3 Influence of β on SCFs under IPB in the brace

(3) Under OPB in the brace

The influences of β on SCFs under OPB in the brace are illustrated in **Fig. 4.4**.

For the location CS (**Fig. 4.4(a)**) and location BS (**Fig. 4.4(b)**), SCFs increase as the value of β increases approximately from 0.3 to 0.4 at tensile side, while they decrease as the value of β increases approximately from 0.4 to 0.6. In addition, they decrease as the value of β increases at compressive side.

(a) SCF$_{CS}$ vs. β

(b) SCF$_{BS}$ vs. β

- 2γ=40, τ=0.4, α=12
- 2γ=40, τ=0.7, α=12
- 2γ=40, τ=1.0, α=12
- 2γ=60, τ=0.4, α=12
- 2γ=60, τ=0.7, α=12
- 2γ=60, τ=1.0, α=12

- 2γ=80, τ=0.4, α=12
- 2γ=80, τ=0.7, α=12
- 2γ=80, τ=1.0, α=12

Fig. 4.4 Influence of β on SCFs under OPB in the brace

(4) Under axial compression in the chord

The influences of β on SCFs under axial compression in the chord are illustrated in
Fig. 4.5.

For the location CC (**Fig. 4.5**), SCFs decreases as the value of β increases.

52
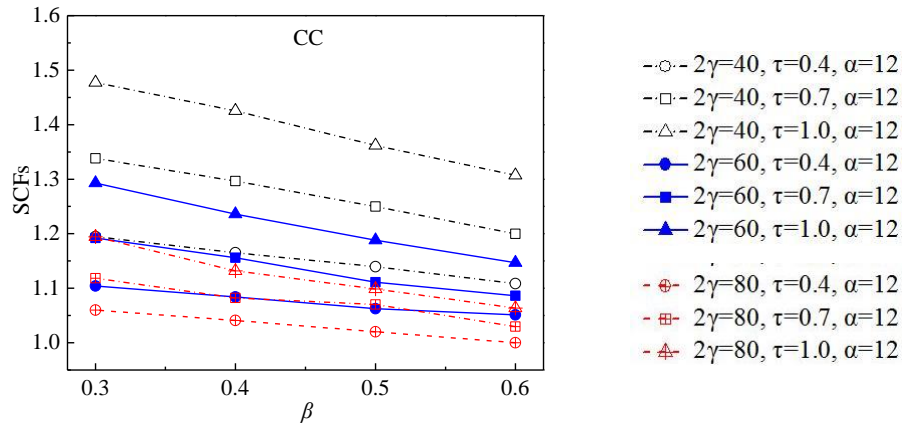
Fig. 4.5 Influence of β on SCFs under axial compression in the chord

(5) Under IPB in the chord
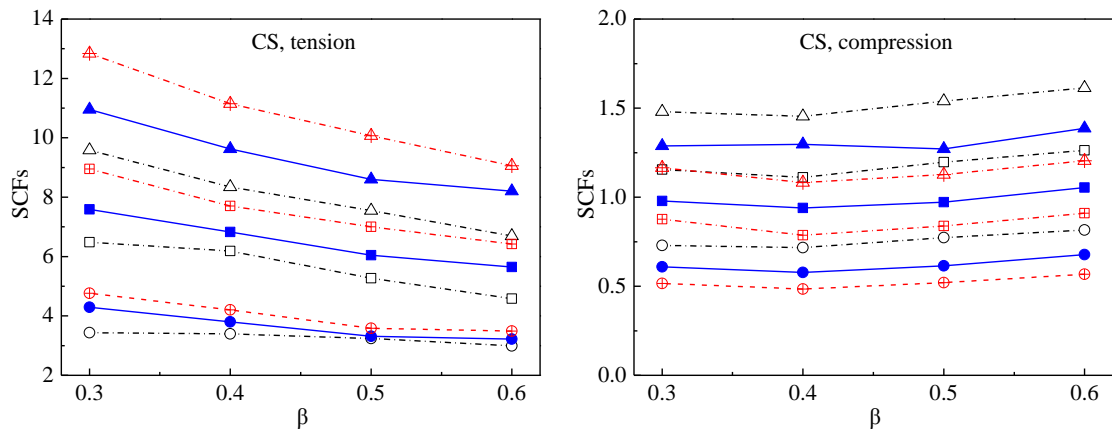
The influences of β on SCFs under IPB in the chord are illustrated in **Fig. 4.6**.

For the location CC (**Fig. 4.6**), SCFs decreases as the value of β increases.
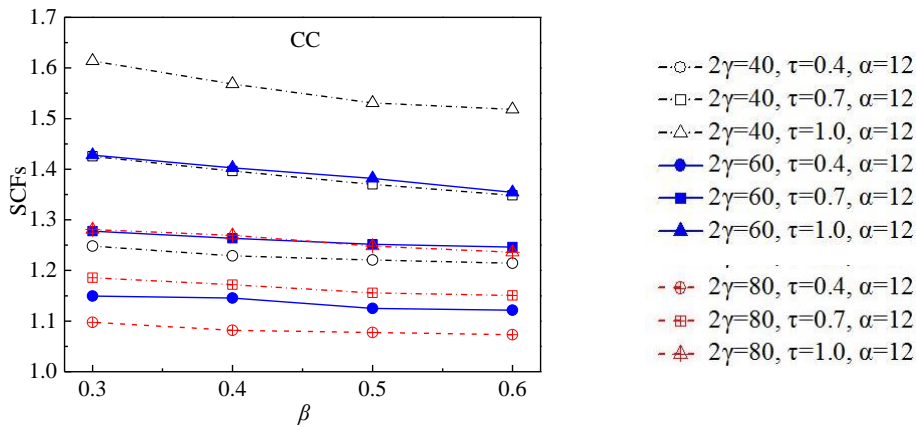
Fig. 4.6 Influence of β on SCFs under IPB in the chord

4.3.2 Influence of diameter to thickness ratio of chord 2γ

(1) Under axial force in the brace

The influences of 2γ on SCFs under axial force in the brace are illustrated in **Fig. 4.7**.

For the location CS (**Fig. 4.7(a)**), the SCF_{CS} increases as the value of 2γ increases under tensile force. However, it decreases as the value of 2γ increases under compressive force.

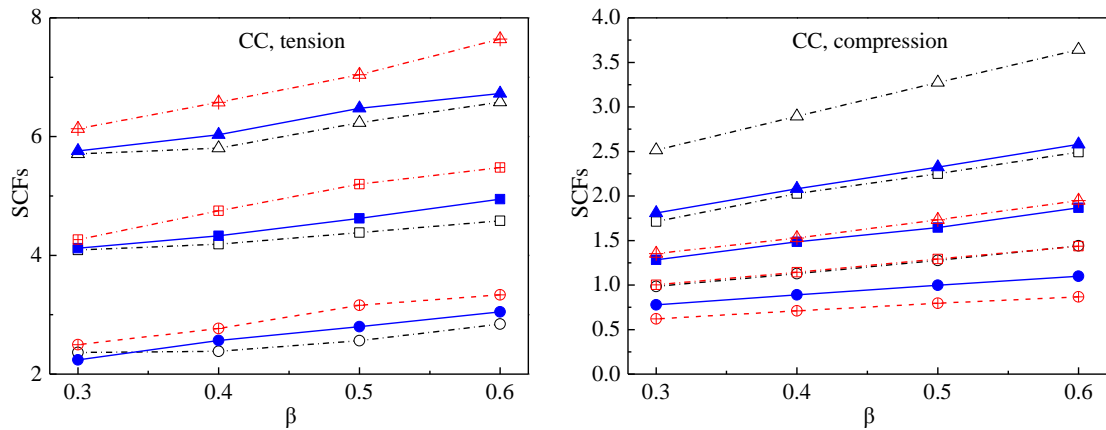For the location CC (**Fig. 4.7(b)**), the SCF_{CC} increases as the value of 2γ increases under tensile force. However, it decreases as the value of β increases under compressive force.
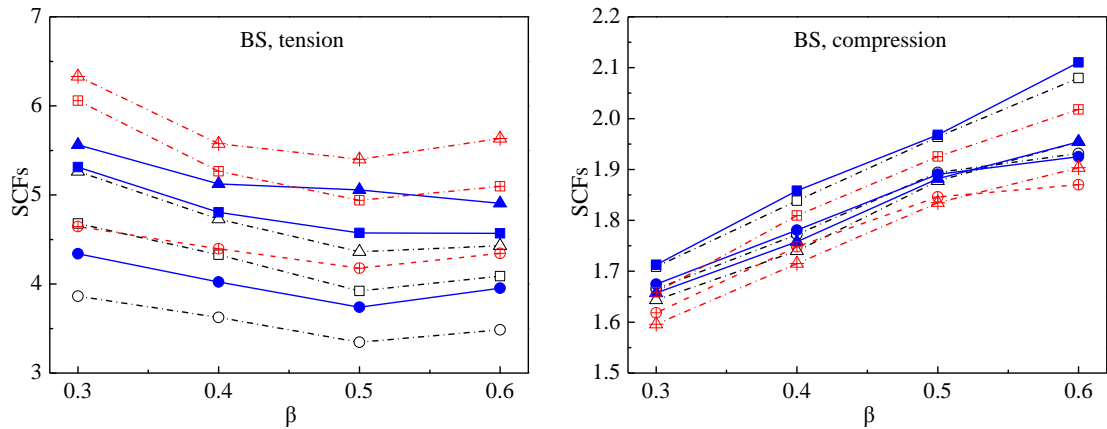
For the location BS (**Fig. 4.7(c)**), the SCF_{BS} increases as the value of 2γ increases under tensile force. Moreover, it increases as the value of 2γ increases from 40 to 50 under compressive force, but it decreases as the value of 2γ increases from 50 to 80.

For the location BC (**Fig. 4.7(d)**), the SCF_{BC} decreases as the value of 2γ increases under tensile and compressive force.

(a) SCF_{CS} vs. 2γ
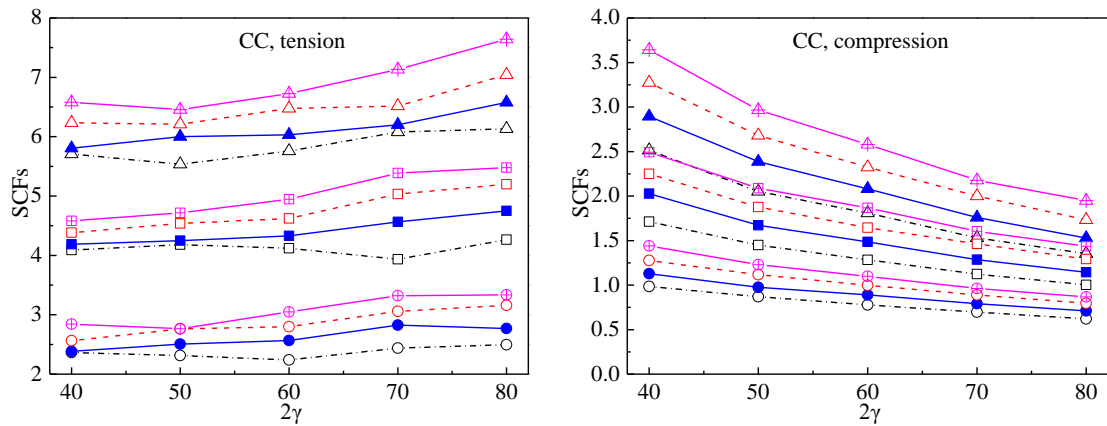
(b) SCF_{CC} vs. 2γ
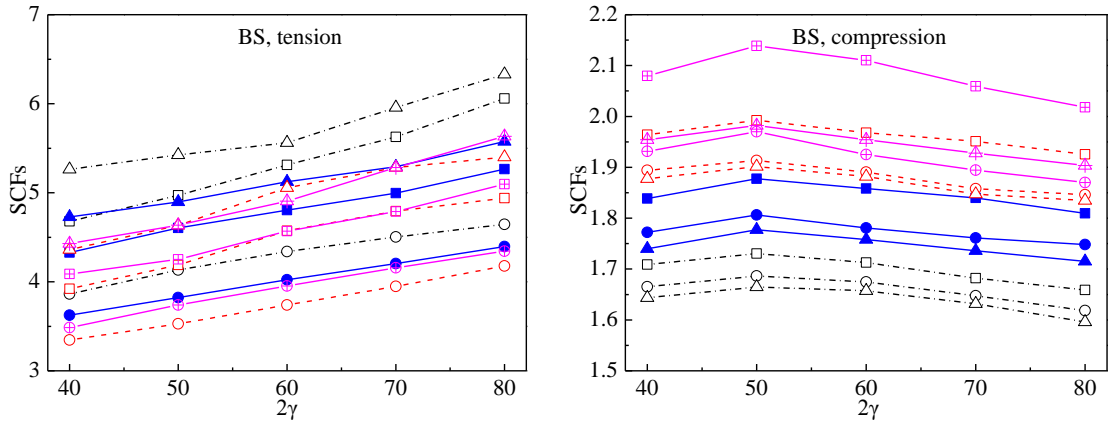
(c) SCF$_{BS}$ vs. 2γ
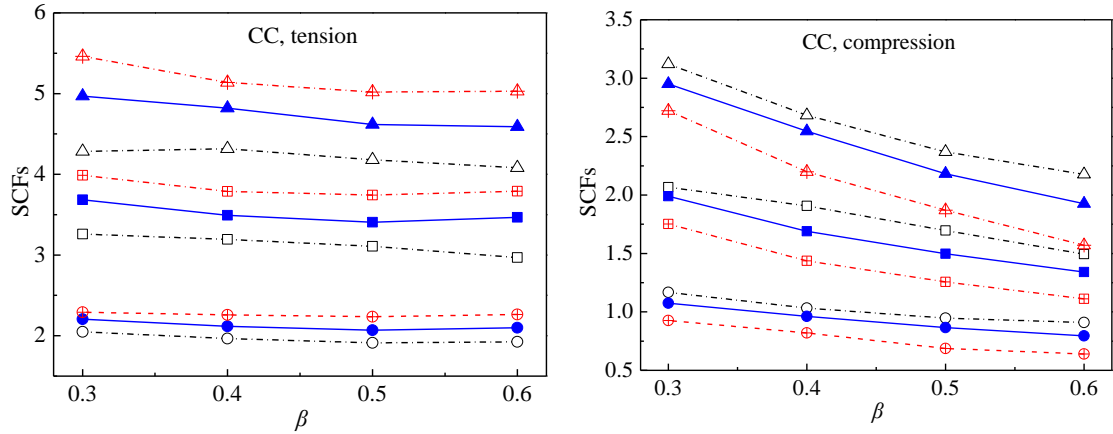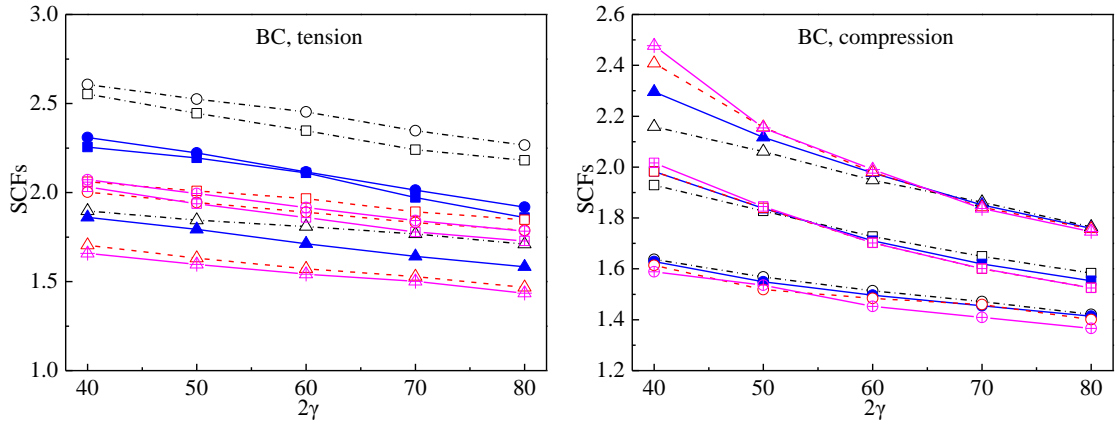

(d) SCF$_{BC}$ vs. 2γ

Fig. 4.7 Influence of 2γ on SCFs under axial force in the brace

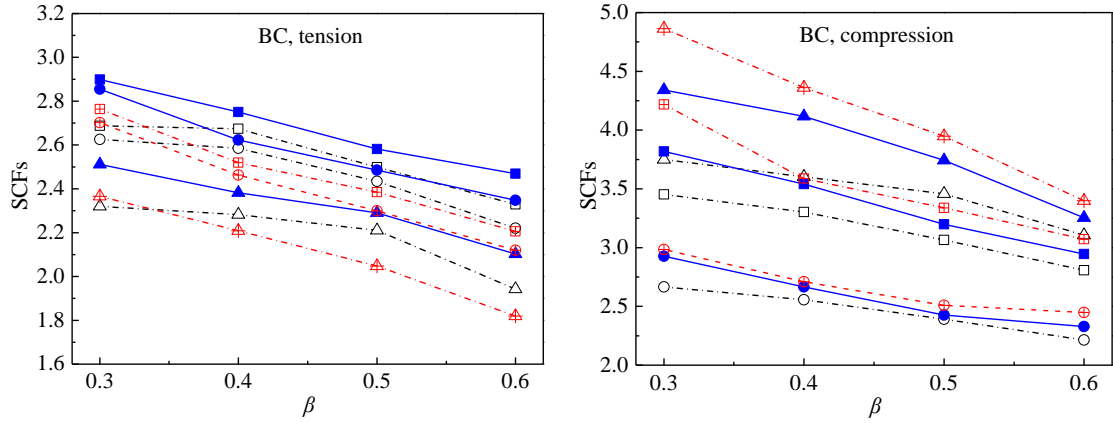**(2) Under IPB in the brace**

The influences of 2γ on SCFs under IPB in the brace are illustrated in **Fig. 4.8**.

For the location CC (**Fig. 4.8(a)**), SCFs increase as the value of 2γ increases at tensile side, but it decreases as the value of 2γ increase at compressive side.

For the location BC (**Fig. 4.8(b)**), SCFs increase as the value of 2γ increases approximately from 40 to 60 at tensile side, while they decrease as the value of 2γ increases approximately from 60 to 80. In addition, they increase as the value of 2γ increases at compressive side.

(a) SCF$_{CC}$ vs. 2γ
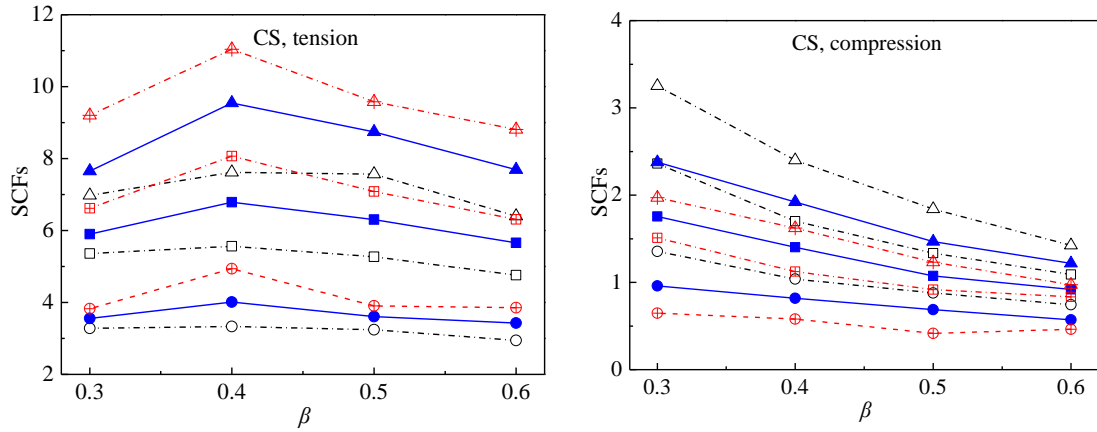

(b) SCF$_{BC}$ vs. 2γ

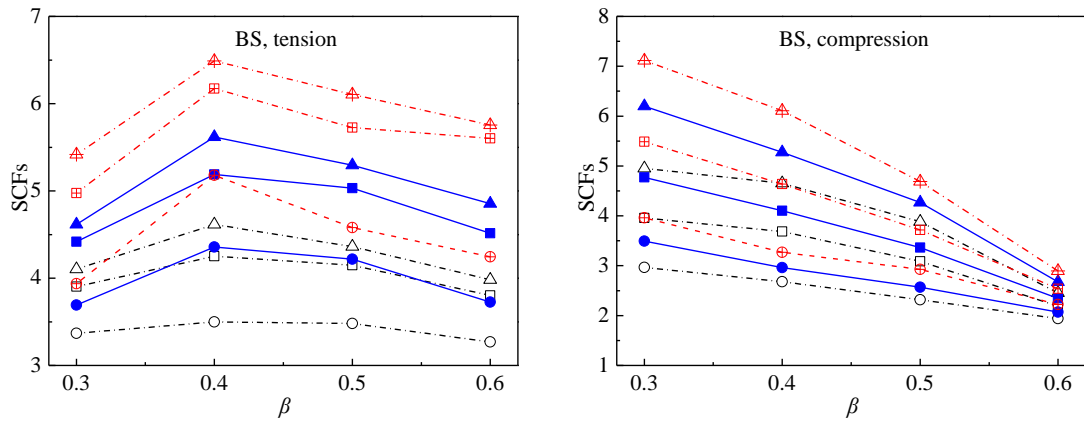**Fig. 4.8** Influence of 2γ on SCFs under IPB in the brace

(3) Under OPB in the brace

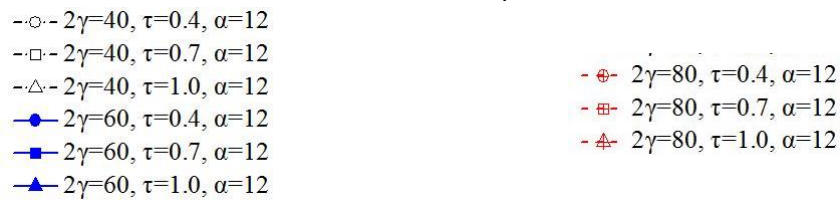The influences of 2γ on SCFs under OPB in the brace are illustrated in **Fig. 4.9**.

For the location CS (**Fig. 4.9(a)**), SCFs increase as the value of 2γ increases at tensile side, while they decrease as the value of 2γ increases at compressive side.

For the location BS (**Fig. 4.9(b)**), SCFs increase as the value of 2γ increases at tensile side as well as compressive side.

(a) SCF_CS vs. 2γ

(b) SCF_BS vs. 2γ

- –○– β=0.3, τ=0.4, α=12
- –□– β=0.3, τ=0.7, α=12
- –△– β=0.3, τ=1.0, α=12
- ●– β=0.4, τ=0.4, α=12
- ■– β=0.4, τ=0.7, α=12
- ▲– β=0.4, τ=1.0, α=12
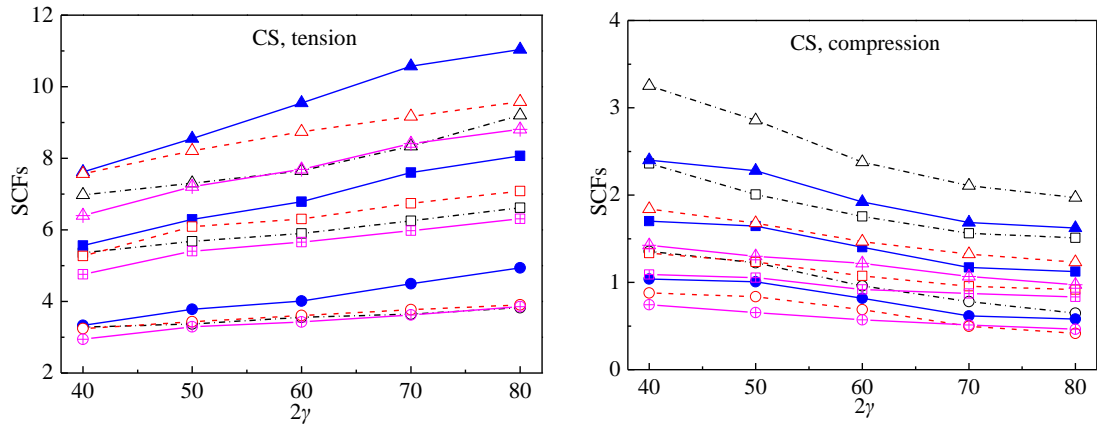
- –○– β=0.5, τ=0.4, α=12
- –□– β=0.5, τ=0.7, α=12
- –△– β=0.5, τ=1.0, α=12
- ⊕– β=0.6, τ=0.4, α=12
- ⊞– β=0.6, τ=0.7, α=12
- △– β=0.6, τ=1.0, α=12

Fig. 4.9 Influence of 2γ on SCFs under OPB in the brace

(4) Under axial compression in the chord

The influences of 2γ on SCFs under axial compression in the chord are illustrated in **Fig. 4.10**.

For the location CC (**Fig. 4.10**), SCFs decrease as the value of 2γ increases.

Fig. 4.10 Influence of 2γ on SCFs under axial compression in the chord

(5) Under IPB in the chord

The influences of 2γ on SCFs under IPB in the chord in the chord are illustrated in **Fig. 4.11**.

For the location CC (**Fig. 4.11**), SCFs decrease as the value of 2γ increases.
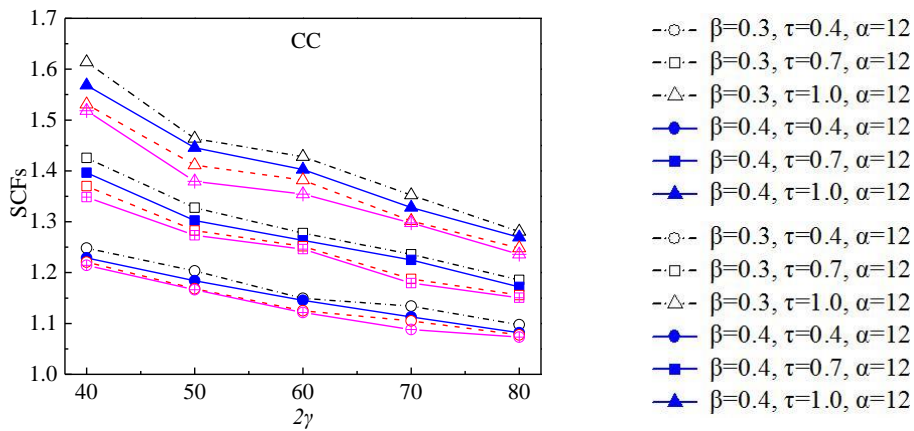
Fig. 4.11 Influence of 2γ on SCFs under IPB in the chord

4.3.3 Influence of thickness ratio τ
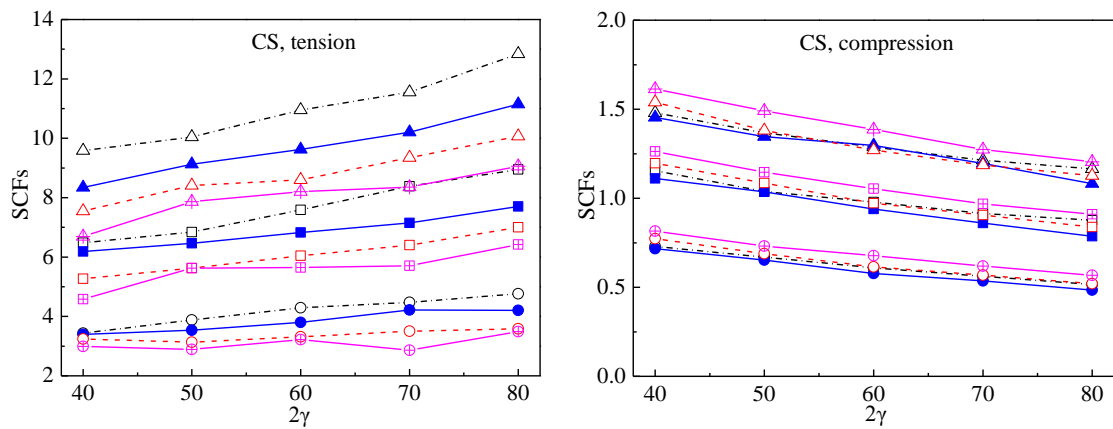
(1) Under axial force in the brace

The influences of τ on SCFs under axial force in the brace are illustrated in **Fig. 4.12**.

For the location CS (**Fig. 4.12(a)**), the SCF_{CS} increases as the value of τ increases under tensile and compressive force.

For the location CC (**Fig. 4.12 (b)**), the SCF_{CC} increases as the value τ increases

under tensile and compressive force.

For the location BS (**Fig. 4.12 (c)**), the SCF$_{BS}$ increases as the value of τ increases under tensile force. Moreover, it increases as the value of τ increases from 0.4 to 0.7 under compressive force, but it decreases as the value of τ increases from 0.7 to 1.0.

For the location BC (**Fig. 4.12 (d)**), the SCF$_{BC}$ increases as the value of τ increases from 0.4 to 0.5 under tensile force, but it decreases as the value of τ increases from 0.5 to 1.0. In addition, it increases as the value of τ increases under compressive force.

(a) SCF$_{CS}$ vs. τ

(b) SCF$_{CC}$ vs. τ

(c) SCF$_{BS}$ vs. τ

(d) SCF$_{BC}$ vs. τ

Legend:
- $2\gamma=40$, $\beta=0.3$, $\alpha=12$
- $2\gamma=40$, $\beta=0.4$, $\alpha=12$
- $2\gamma=40$, $\beta=0.5$, $\alpha=12$
- $2\gamma=40$, $\beta=0.6$, $\alpha=12$
- $2\gamma=60$, $\beta=0.3$, $\alpha=12$
- $2\gamma=60$, $\beta=0.4$, $\alpha=12$
- $2\gamma=60$, $\beta=0.5$, $\alpha=12$
- $2\gamma=60$, $\beta=0.6$, $\alpha=12$
- $2\gamma=80$, $\beta=0.3$, $\alpha=12$
- $2\gamma=80$, $\beta=0.4$, $\alpha=12$
- $2\gamma=80$, $\beta=0.5$, $\alpha=12$
- $2\gamma=80$, $\beta=0.6$, $\alpha=12$
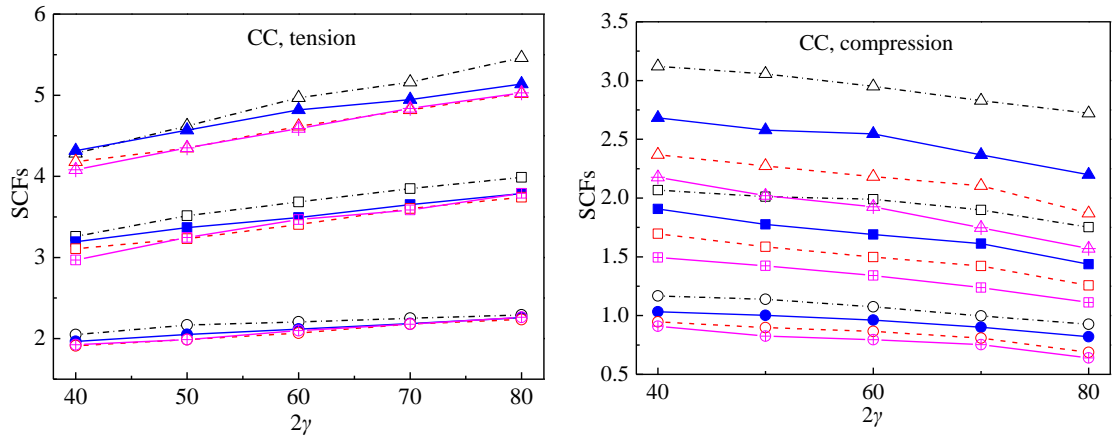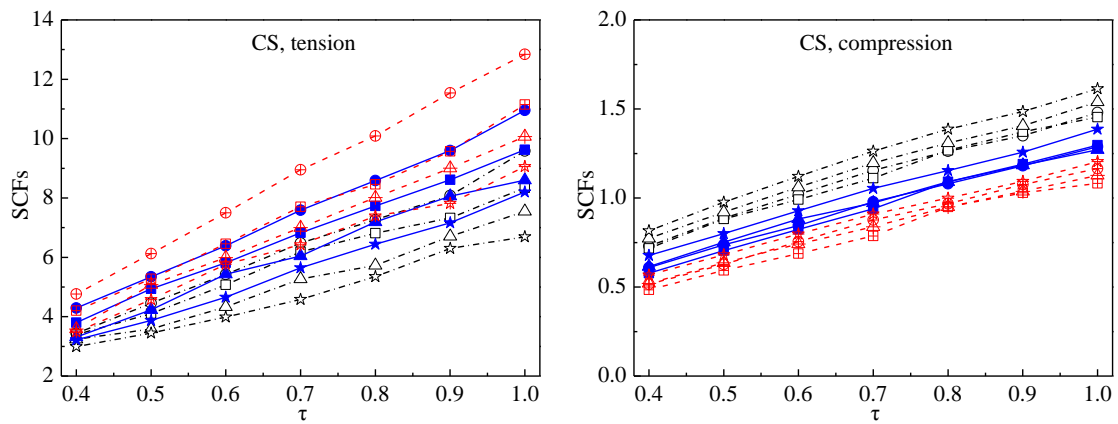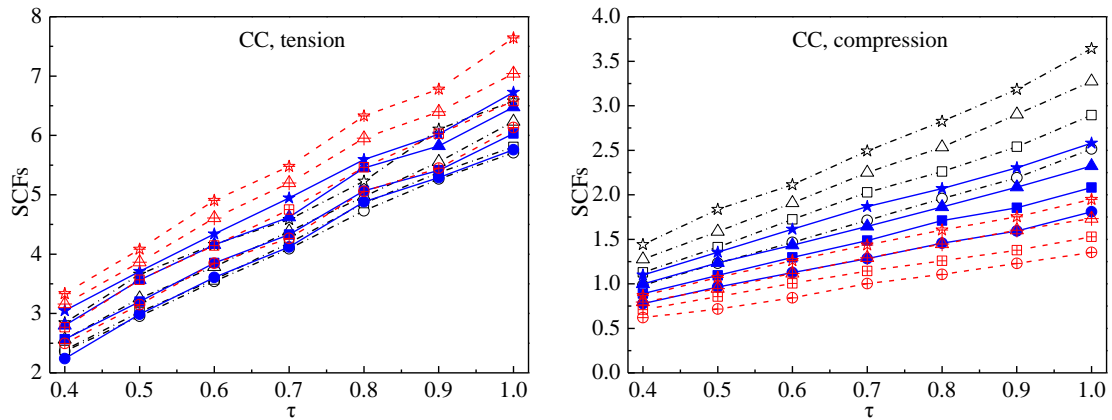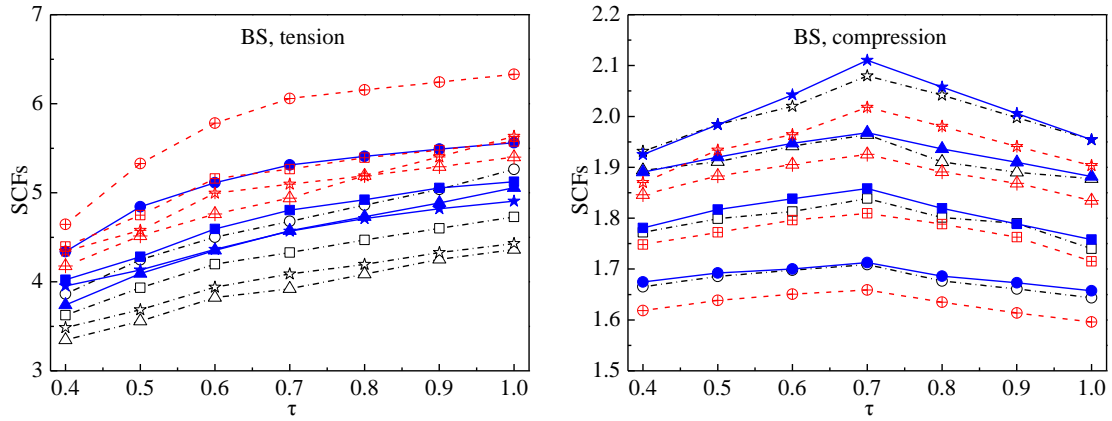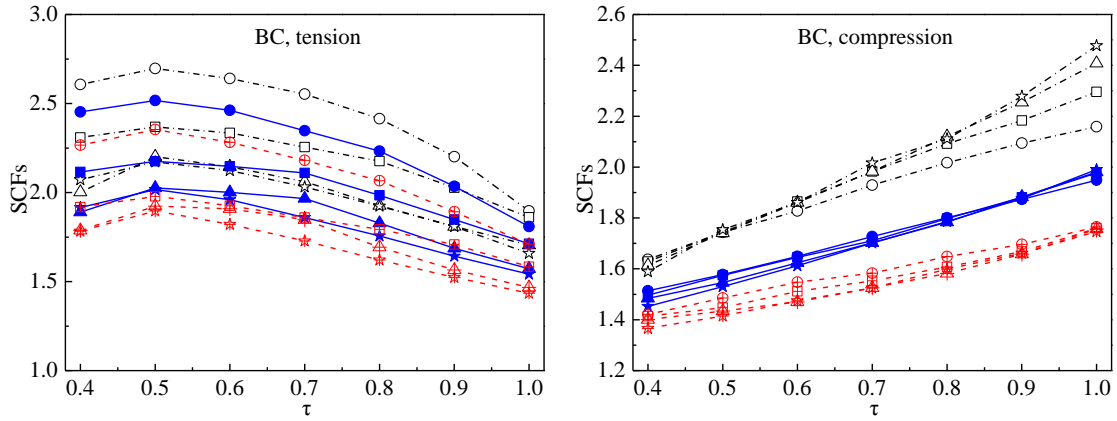
Fig. 4.12 Influence of τ on SCFs under axial force in the brace

(2) Under IPB in the brace

The influences of τ on SCFs under IPB in the brace are illustrated in **Fig. 4.13**.

For the location CC (**Fig. 4.13(a)**), SCFs increase as the value of τ increases at tensile side as well as compressive side.

For the location BC (**Fig. 4.13(b)**), SCFs increase as the value of τ increases approximately from 0.4 to 0.6 at tensile side, while they decrease as the value of τ increases approximately from 0.6 to 1.0. In addition, they increase as the value of τ increases at compressive side.
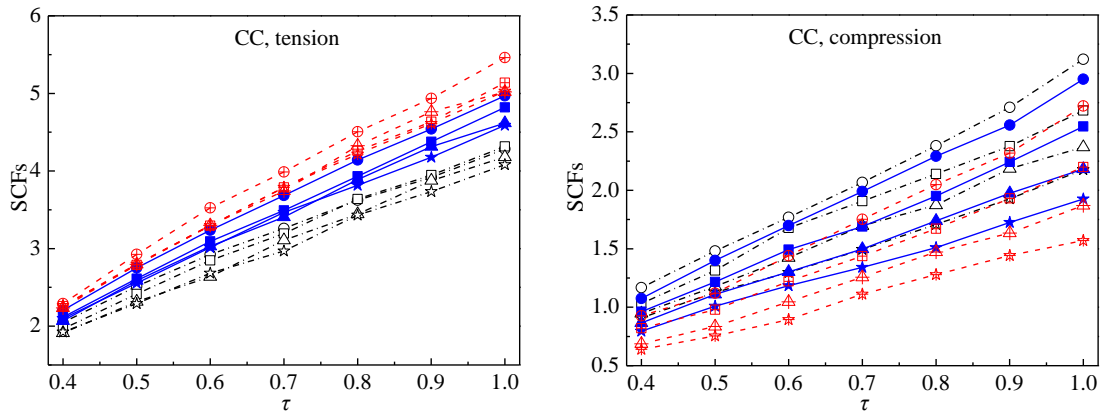
(a) SCF$_{CC}$ vs. τ
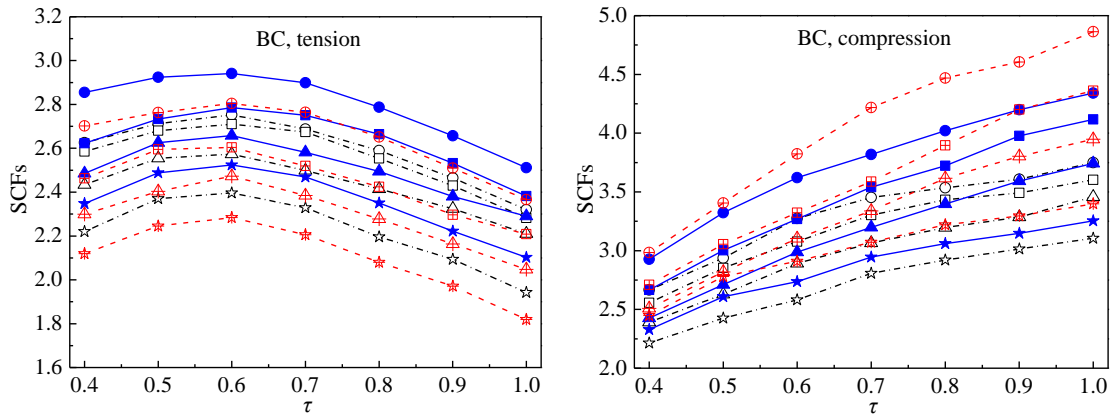
(b) SCF$_{BC}$ vs. τ

Fig. 4.13 Influence of τ on SCFs under IPB in the brace

(3) Under OPB in the brace

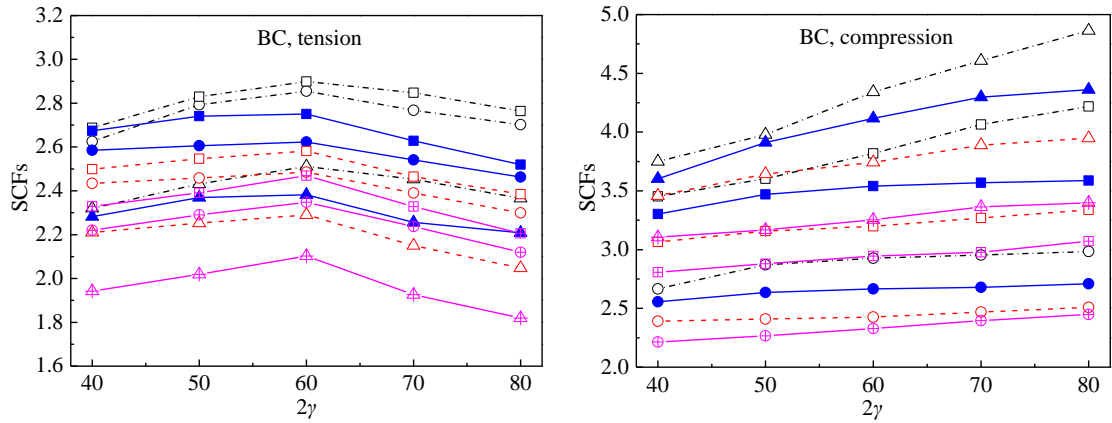The influences of τ on SCFs under OPB in the brace are illustrated in **Fig. 4.14**.

For the location CS (**Fig. 4.14(a)**), SCFs increase as the value of τ increases at tensile side as well as compressive side.

For the location BS (**Fig. 4.14(b)**), SCFs increase as the value of τ increases at tensile side as well as compressive side.

(a) SCF$_{CS}$ vs. τ

(b) SCF$_{BS}$ vs. τ

Fig. 4.14 Influence of τ on SCFs under OPB in the brace

(4) Under axial compression in the chord

    The influences of τ on SCFs under axial compression in the chord are illustrated in **Fig. 4.15**.

    For the location CC (**Fig. 4.15**), SCFs increase as the value of τ increases.
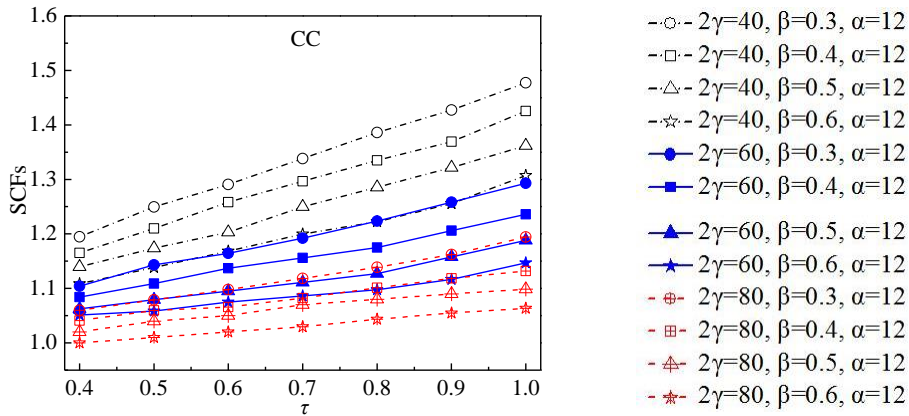
Fig. 4.15 Influence of τ on SCFs under axial compression in the chord

(5) Under IPB in the chord
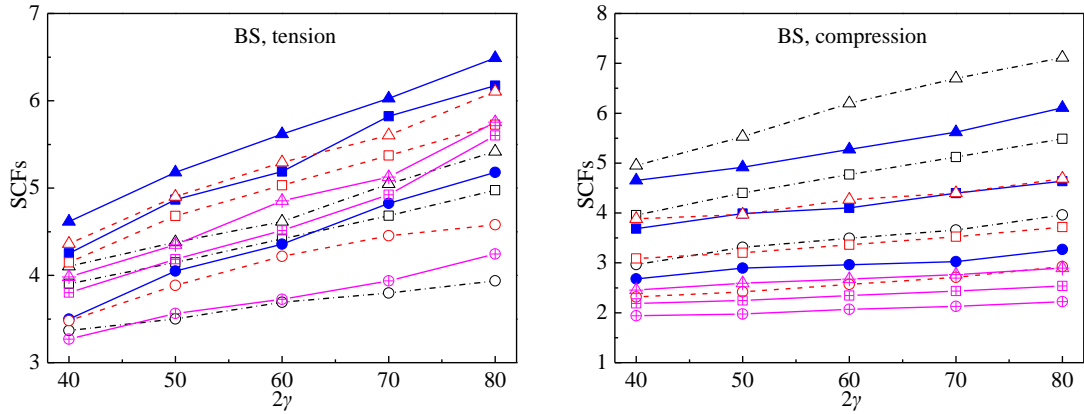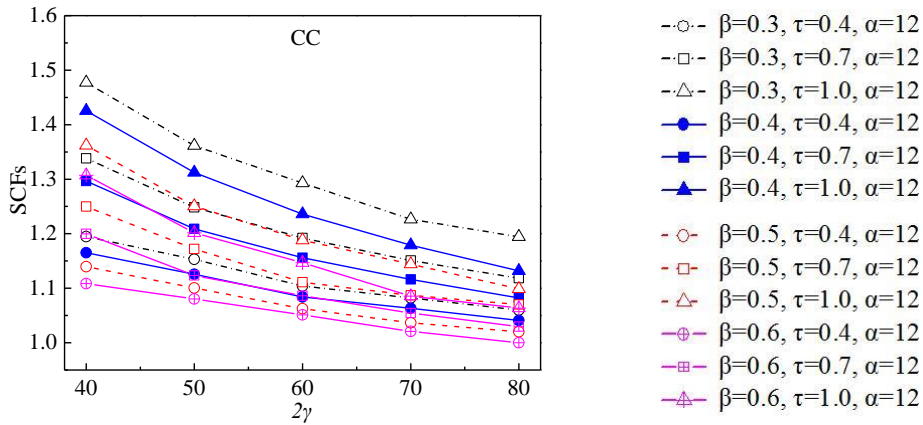
The influences of τ on SCFs under IPB in the chord are illustrated in **Fig. 4.16**.

For the location CC (**Fig. 4.16**), SCFs increase as the value of τ increases.
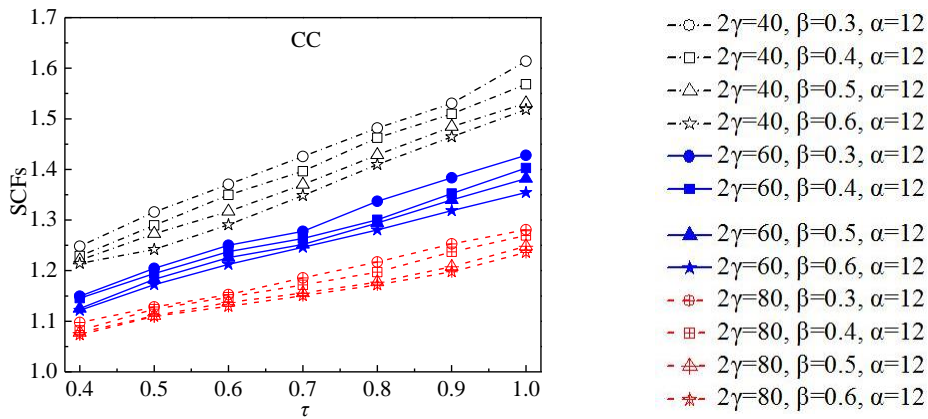
Fig. 4.16 Influence of τ on SCFs under IPB in the chord

4.3.4 Influence of relative chord length α

(1) Under axial force in the brace

The influences of α on SCFs under axial force in the brace are illustrated in **Fig. 4.17**.

For the location CS (**Fig. 4.17(a)**), the influence of α on the SCF$_{CS}$ can be neglected under tensile force. In addition, the influence is also not significant under compressive force.

For the location CC (**Fig. 4.17(b)**), the SCF$_{CC}$ increases as the value of α increases

under tensile and compressive forces.

For the location BS (**Fig. 4.17(c)**), the influence of α on the SCF$_{BS}$ can be neglected under tensile force. Moreover, the influences of α is not significant under compressive force.

For the location BC (**Fig. 4.17(d)**), the influence of α on the SCF$_{BC}$ can be neglected under tensile and compressive forces.

(a) SCF$_{CS}$ vs. α

(b) SCF$_{CC}$ vs. α

(c) SCF$_{BS}$ vs. α

(d) SCF$_{BC}$ vs. α

- -○- $\beta=0.3$, $2\gamma=40$, $\tau=0.4$ - ○- $\beta=0.5$, $2\gamma=80$, $\tau=0.4$
- -□- $\beta=0.3$, $2\gamma=40$, $\tau=0.7$ - □- $\beta=0.5$, $2\gamma=80$, $\tau=0.7$
- -△- $\beta=0.3$, $2\gamma=40$, $\tau=1.0$ - △- $\beta=0.5$, $2\gamma=80$, $\tau=1.0$
- ●- $\beta=0.4$, $2\gamma=60$, $\tau=0.4$ - ⊕- $\beta=0.6$, $2\gamma=40$, $\tau=0.4$
- ■- $\beta=0.4$, $2\gamma=60$, $\tau=0.7$ - ⊞- $\beta=0.6$, $2\gamma=40$, $\tau=0.7$
- ▲- $\beta=0.4$, $2\gamma=60$, $\tau=1.0$ - △- $\beta=0.6$, $2\gamma=40$, $\tau=1.0$
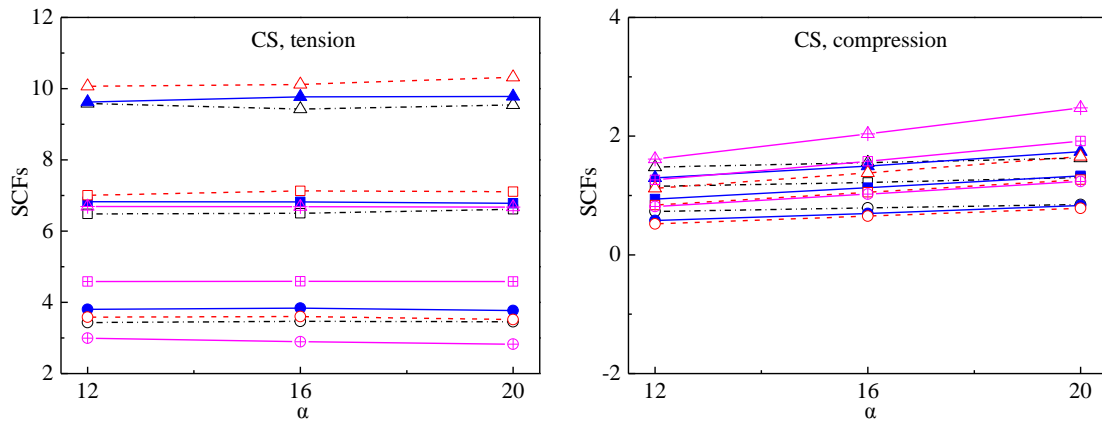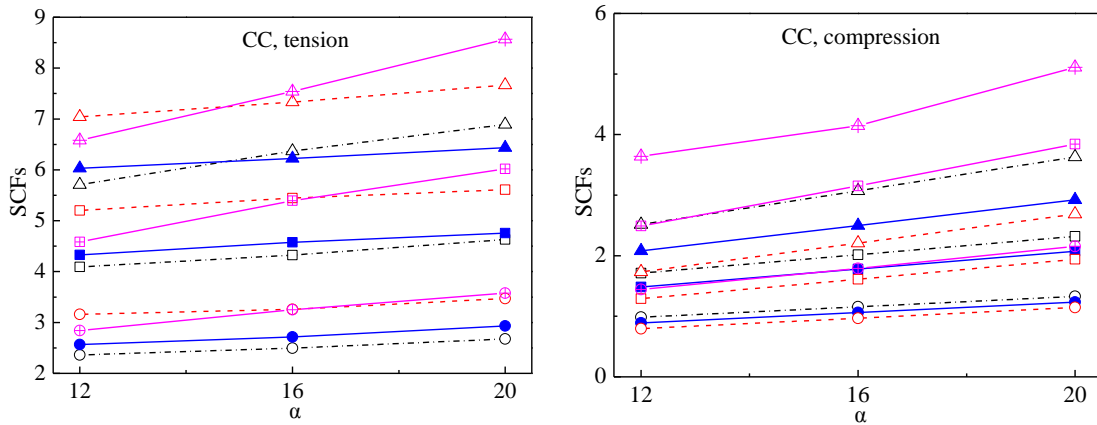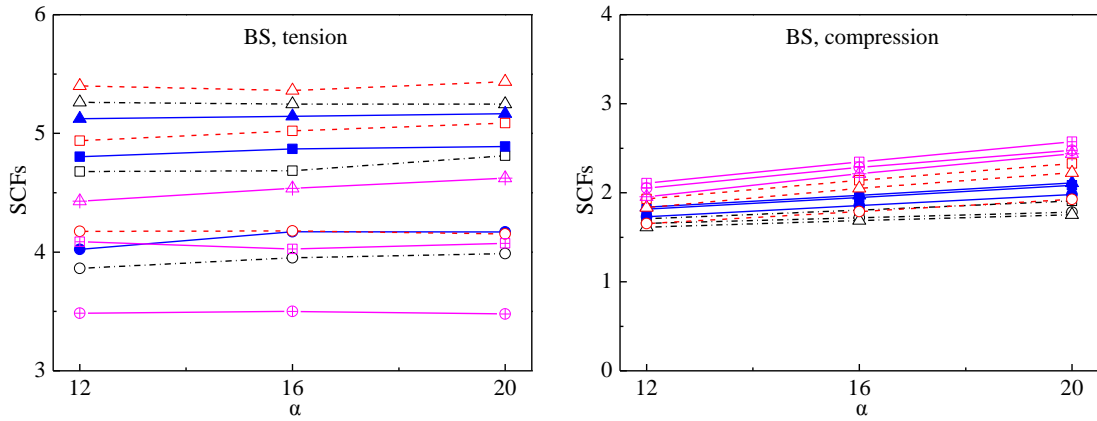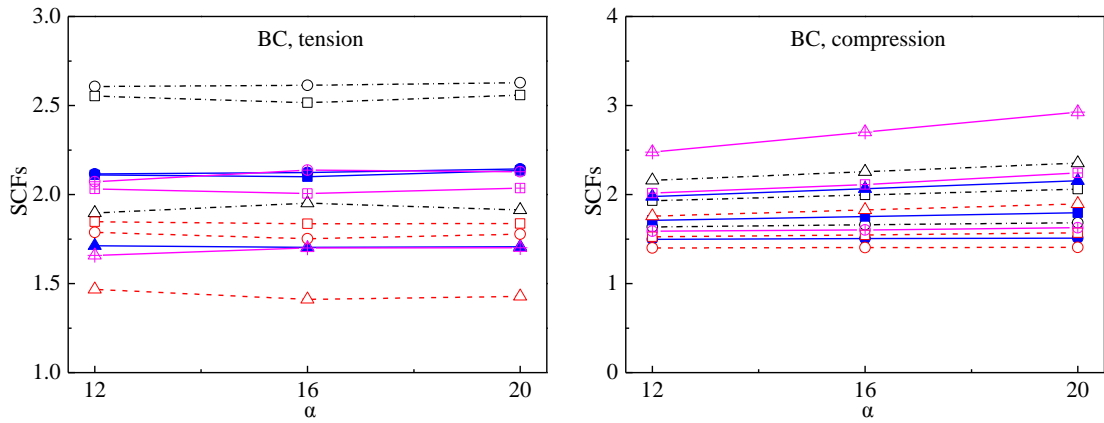
Fig. 4.17 Influence of α on SCFs under axial force in the brace

(2) Under OPB in the brace

The influences of α on SCFs are illustrated in **Fig. 4.18**. It shows that the influences of α on SCFs can be neglected for the locations CS and BS under OPB in the brace.

65

(a) SCF$_{CS}$ vs. α

(b) SCF$_{BS}$ vs. α

- -○- β=0.3, 2γ=40, τ=0.4
- -□- β=0.3, 2γ=40, τ=0.7
- -△- β=0.3, 2γ=40, τ=1.0
- -●- β=0.4, 2γ=60, τ=0.4
- -■- β=0.4, 2γ=60, τ=0.7
- -▲- β=0.4, 2γ=60, τ=1.0
- -○- β=0.5, 2γ=80, τ=0.4
- -□- β=0.5, 2γ=80, τ=0.7
- -△- β=0.5, 2γ=80, τ=1.0
- -⊕- β=0.6, 2γ=40, τ=0.4
- -⊞- β=0.6, 2γ=40, τ=0.7
- -⬭- β=0.6, 2γ=40, τ=1.0

Fig. 4.18 Influence of α on SCFs under OPB in the brace

4.3.5 Discussions

(1) Under axial force in the brace

By comparing the SCFs caused by tensile force with those caused by compressive force shown in **Figs. 10-13**, it can be noticed that the former is generally much larger than the latter. Since the adhesion between the steel and concrete was not strong, the inner wall of chord tube around the intersection tended to separate from the surface of filled-concrete when the brace was subjected to tensile force, as shown in **Fig. 3.7**. Consequently, the

out-of-plane bending deformation of the chord tube around the intersection became larger, which induced higher HSS under tensile force than under compressive force. In addition, the influence of τ on SCFs is much larger than that of β, 2γ and α for all four locations in most cases.

By comparing the SCF_{CS} with SCF_{CC}, it can be also noticed that the SCF_{CS} are larger under tensile force, while the SCF_{CC} are larger under compressive force in most cases. It indicates that the maximum SCFs in the chord generally occur at the saddle (CS) and crown (CC) under tensile and compressive force, respectively. Meanwhile, the maximum SCFs of CHS T-joints generally occur at location CS, regardless of whether the axial force applied to the brace is compression or tension [77]. The mechanical behavior around the intersection of CFST T-joints under tensile force is considered to be similar to that of CHS T-joints since the separation between chord tube and filled-concrete can occur in CFST T-joint. In contrast, the filled-concrete greatly increases the stiffness of CFST T-joint against compressive force in the brace and makes the stress distribution around the intersection more uniform. Furthermore, the position of the maximum SCFs changed from the saddle (CS) to crown (CC).

By comparing the SCF_{BS} with SCF_{BC}, it can be noticed that the SCF_{BS} are generally larger under tensile force, while the magnitudes of SCF_{BS} and SCF_{BC} are similar under compressive force. In other words, the maximum SCFs in the brace occur at the saddle (BS) under tensile force in general. However, they can occur at the saddle (BS) or crown (BC) under compressive force. The difference of maximum SCF location in the brace can be explained similarly to the above discussions.

(2) Under the bending in the brace

By comparing the SCFs shown in **Figs. 5-7**, it can be observed that the location of maximum SCFs is usually location CC (tension) and CS (tension) under in-plane and out-of-plane bending, respectively. Since the adhesion between the chord tube and concrete was not strong, the inner wall of chord around the intersection tended to separate from the filled-concrete at tensile side, while the filled-concrete would provide strong support to chord wall at compressive side, as shown in **Fig. 4.19**. Consequently, the local bending deformation around the intersection at tensile side became much larger than that at compressive side, resulting in higher SCFs at tensile side than at compressive side.
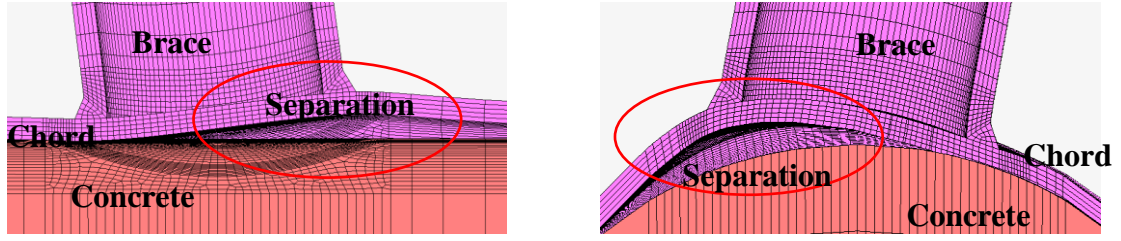
(a) Under in-plane bending in the brace   (b) Under out-of-plane bending in the brace

Fig. 4.19 Amplified deformation between chord tube and concrete

4.4 SCF formulae for CFST T-joints

4.4.1 Formulation

(1) Under axial force in the brace

Based on the results of parametric analysis as well as the SCF formulae given in the CIDECT Design Guide [14] for CHS T-joints subjected to axial force in the brace, the SCF formulae at locations CS and CC under tensile or compressive force can be expressed as **Eqs. (4.1)** and **(4.2)**, respectively. Those at locations BS and BC under tensile and compressive force can be expressed as **Eqs. (4.3)** and **(4.4)**, respectively.

The axial loading in the brace results in a bending moment in the chord. The bending moment is the main cause of the stress at location CC, and it changes with chord length which can be represented by α. Therefore, the influence of α on SCFs at location CC needs to be considered. Referring to [103], the last term corresponding to the SCF at location CC due to global bending is introduced in **Eq. (4.2)**. The direction of stress caused by the bending moment in the chord is the longitudinal direction along the chord tube and perpendicular to the weld toe at location CC, while parallel to the weld toe at location CS. Therefore, the influence of α on SCFs at location CS is not considered in **Eq. (4.1)**.

$$\mathrm{SCF_{CS}} = A_{\mathrm{CS}} \cdot \gamma^{B_{\mathrm{CS}}} \cdot \tau^{C_{\mathrm{CS}}} \cdot [D_{\mathrm{CS}} + E_{\mathrm{CS}} \cdot (\beta + F_{\mathrm{CS}})^2] \tag{4.1}$$

$$\mathrm{SCF_{CC}} = A_{\mathrm{CC}} \cdot \gamma^{B_{\mathrm{CC}}} \cdot \tau^{C_{\mathrm{CC}}} \cdot [D_{\mathrm{CC}} + E_{\mathrm{CC}} \cdot (\beta + F_{\mathrm{CC}})^2] + \frac{M_{\mathrm{Chord}}}{W_e \sigma_n} \tag{4.2}$$

$$\mathrm{SCF_{BS}} = A_{\mathrm{BS}} \cdot \gamma^{B_{\mathrm{BS}}} \cdot \tau^{C_{\mathrm{BS}}} \cdot [D_{\mathrm{BS}} + E_{\mathrm{BS}} \cdot (\beta + F_{\mathrm{BS}})^2] \qquad \text{(tension)} \tag{4.3a}$$

$$= A_{\mathrm{BS}} \cdot \gamma^{B_{\mathrm{BS}}} \cdot \beta^{C_{\mathrm{BS}}} \cdot [D_{\mathrm{BS}} + E_{\mathrm{BS}} \cdot (\tau + F_{\mathrm{BS}})^2] \qquad \text{(compression)} \tag{4.3b}$$

$$\mathrm{SCF_{BC}} = A_{\mathrm{BC}} \cdot \gamma^{B_{\mathrm{BC}}} \cdot \beta^{C_{\mathrm{BC}}} \cdot [D_{\mathrm{BC}} + E_{\mathrm{BC}} \cdot (\tau + F_{\mathrm{BC}})^2] \qquad \text{(tension)} \quad (4.4a)$$

$$= A_{\mathrm{BC}} \cdot \gamma^{B_{\mathrm{BC}}} \cdot \tau^{C_{\mathrm{BC}}} \cdot \beta^{D_{\mathrm{BC}}} \qquad \qquad \text{(compression)} \quad (4.4b)$$

where, the constants A_{CS} to F_{CS}, A_{CC} to F_{CC}, A_{BS} to F_{BS} and A_{BC} to F_{BC} would be determined by multiple regression analysis. M_{Chord} is the global bending moment in the chord around the intersection, W_{e} is the section modulus for equivalent steel tube section, and σ_{n} is the nominal stress in the brace.

Assuming a small wall thickness compared with the diameter of brace, the relation between the force F and the nominal stress in the brace (σ_{n}) is derived as follows.

$$F = \pi dt \sigma_{\mathrm{n}} \qquad (4.5)$$

The flexural stiffness EI of concrete-filled chord is determined according to the **Eq. (4.6)** [97].

$$EI = E_c I_c + E_s I_s \qquad (4.6)$$

where, E_c and E_s, I_c and I_s are the Young's moduli and moments of inertia of filled-concrete and steel tube, respectively.

The moment of inertia of steel tube and filled-concrete are calculated by **Eqs. (4.7)** and **(4.8)**, respectively.

$$I_s = \frac{\pi[D^4 - (D-2T)^4]}{64} \qquad (4.7)$$

$$I_c = \frac{\pi(D-2T)^4}{64} \qquad (4.8)$$

From **Eqs. (6)-(8)**, the wall thickness T_{e} of the equivalent steel tube section is derived as follows.

$$T_e = \frac{D - (D-2T) \cdot \sqrt[4]{\dfrac{m-1}{m}}}{2} \qquad (4.9)$$

$$m = \frac{E_s}{E_c} \qquad (4.10)$$

Consequently, the section modulus for equivalent steel tube section W_{e} is obtained as follows.

$$W_e = \frac{\pi D^3}{32}(1 - n^4) \qquad (4.11)$$

$$n = \frac{D - 2T_e}{D} \qquad (4.12)$$

According to the results of the multiple regression analysis, the formulae for determining SCFs in the chord and brace of CFST T-joints under axial force in the brace are given as follows,

Location CS

$$\text{SCF}_{\text{CS}} = 2.351\gamma^{0.39}\tau^{1.03}[0.818+1.254(\beta-0.878)^2] \qquad \text{(tension)} \quad (4.13a)$$

$$= 6.767\gamma^{-0.482}\tau^{0.79}[0.984+1.255(\beta-0.198)^2] \qquad \text{(compression)} \quad (4.13b)$$

Location CC

$$\text{SCF}_{\text{CC}} = 1.401\gamma^{0.365}\tau^{0.916}[1.028+0.883(\beta-0.29)^2]+\frac{M_{\text{Chord}}}{W_e\sigma_n} \qquad \text{(tension)} \quad (4.14a)$$

$$= 37.077\gamma^{-1.096}\tau^{0.895}[1.122-0.095(\beta+0.274)^2]+\frac{M_{\text{Chord}}}{W_e\sigma_n} \qquad \text{(comp.)} \quad (4.14b)$$

Location BS

$$\text{SCF}_{\text{BS}} = 0.636\gamma^{0.308}\tau^{0.28}[2.751+8.645(\beta-0.531)^2] \qquad \text{(tension)} \quad (4.15a)$$

$$= 0.989\gamma^{-0.044}\beta^{0.316}[2.942-0.638(\tau-0.759)^2] \qquad \text{(compression)} \quad (4.15b)$$

Location BC

$$\text{SCF}_{\text{BC}} = 1.122\gamma^{-0.228}\beta^{-0.317}[3.154-3.121(\tau-0.519)^2] \qquad \text{(tension)} \quad (4.16a)$$

$$= 6.025\gamma^{-0.329}\tau^{0.326}\beta^{-0.007} \qquad \text{(compression)} \quad (4.16b)$$

The validity ranges of the proposed parametric formulae in **Eqs. (4.13)-(4.16)** are $0.3 \leq \beta \leq 0.6$, $40 \leq 2\gamma \leq 80$, $0.4 \leq \tau \leq 1.0$ and $12 \leq \alpha \leq 20$ since the validity of the formulae has been confirmed only for those ranges.

(2) The rest loading conditions

By using the multiple regression analysis, formulae for determining SCFs in the chord and brace of CFST T-joints under different loading conditions are obtained as follows.

(2.1) Under IPB in the brace

Location CC

$$\text{SCF}_{\text{CC}} = 1.765\gamma^{0.268}\tau^{0.869}\beta^{-0.100} \qquad \text{(tension)} \quad (4.17a)$$

$$= 4.948\gamma^{-0.363}\tau^{1.036}\beta^{-0.550} \qquad \text{(compression)} \quad (4.17b)$$

Location BC

$$\text{SCF}_{\text{BC}} = 1.575\gamma^{0.121}\beta^{-0.289}[0.901 - 0.867(\tau - 0.591)^2] \quad 40 \le 2\gamma \le 60 \quad \text{(tension)} \quad (4.18\text{a})$$

$$= 6.373\gamma^{-0.290}\beta^{-0.289}[0.901 - 0.867(\tau - 0.591)^2] \quad 60 < 2\gamma \le 80 \quad \text{(tension)} \quad (4.18\text{b})$$

$$= 1.536\gamma^{0.184}\tau^{0.431}\beta^{-0.361} \qquad\qquad\qquad\qquad \text{(comp.)} \quad (4.18\text{c})$$

(2.2) Under OPB in the brace

  Location CS

$$\text{SCF}_{\text{CS}} = 2.102\gamma^{0.396}\tau^{0.904}[1.145 - 6.927(\beta - 0.434)^2] \qquad\qquad \text{(tension)} \quad (4.19\text{a})$$

$$= 7.737\gamma^{-0.671}\tau^{0.914}\beta^{-0.928} \qquad\qquad\qquad \text{(compression)} \quad (4.19\text{b})$$

  Location BS

$$\text{SCF}_{\text{BS}} = 1.082\gamma^{0.447}\tau^{0.259}[1.141 - 6.761(\beta - 0.451)^2] \qquad\qquad \text{(tension)} \quad (4.20\text{a})$$

$$= 0.655\gamma^{0.324}\tau^{0.504}\beta^{-0.948} \qquad\qquad\qquad \text{(compression)} \quad (4.20\text{b})$$

(2.3) Under axial compression in the chord

  Location CC

$$\text{SCF}_{\text{CC}} = 2.425\gamma^{-0.237}\tau^{0.135}\beta^{-0.134} \tag{4.21}$$

(2.4) Under IPB in the chord

  Location CC

$$\text{SCF}_{\text{CC}} = 2.927\gamma^{-0.240}\tau^{0.204}\beta^{-0.060} \tag{4.22}$$

   The validity ranges of these proposed parametric formulae in **Eqs. (4.17)-(4.22)** are $0.3 \le \beta \le 0.6$, $40 \le 2\gamma \le 80$ and $0.4 \le \tau \le 1.0$ since the validity of the formulae has been confirmed only for those ranges.

4.4.2 Accuracy verification

(1) Under axial force in the brace

   The SCFs obtained by the proposed formulae, SCF$_{\text{FOR}}$, were compared with those by FEA, SCF$_{\text{FEA}}$, for all locations to verify the accuracy of the formulae. The comparisons under axial tensile force and compressive force are shown in **Figs. 4.20(a)-(d)** and **Figs. 20(e)-(h)**, respectively. They include the statistical values of the ratio of SCF$_{\text{FOR}}$ to SCF$_{\text{FEA}}$, SCF$_{\text{FOR}}$/SCF$_{\text{FEA}}$, as well. The graphs show the good agreement between SCF$_{\text{FOR}}$ and SCF$_{\text{FEA}}$ in general. The mean values of SCF$_{\text{FOR}}$/SCF$_{\text{FEA}}$ are very close to 1.0 for all locations, and the corresponding coefficients of variance (COV) are relatively small.
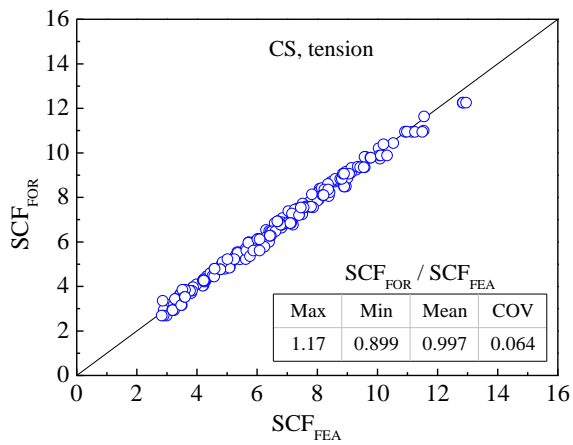
(a) CS: axial tensile fore in brace
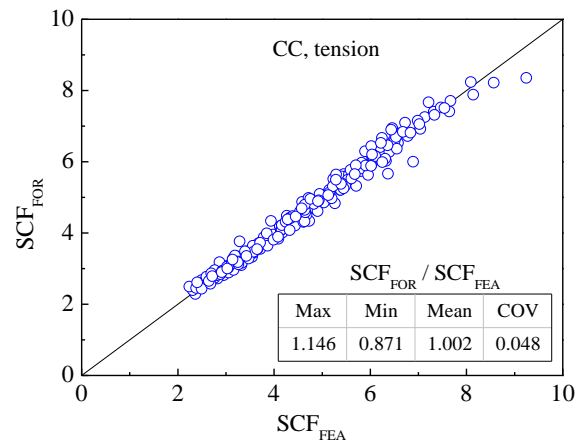
(b) CC: axial tensile fore in brace
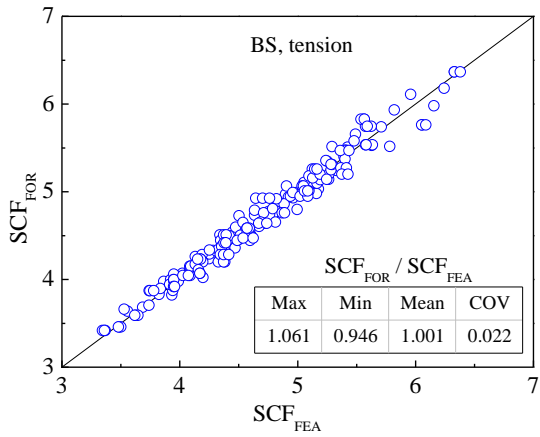
(c) BS: axial tensile fore in brace
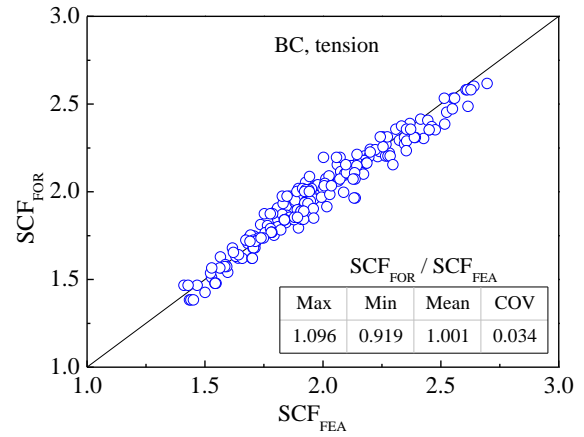
(d) BC: axial tensile fore in brace
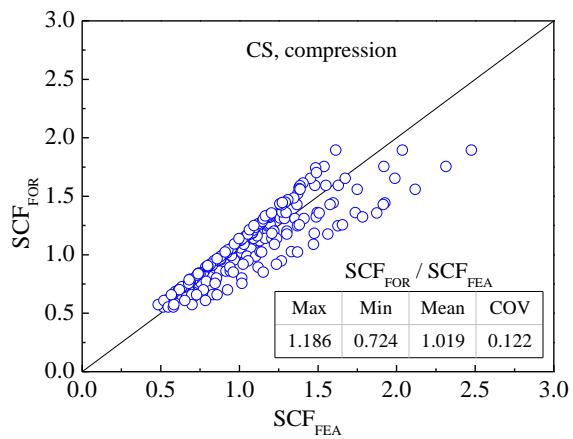
(e) CS: axial compressive fore in brace
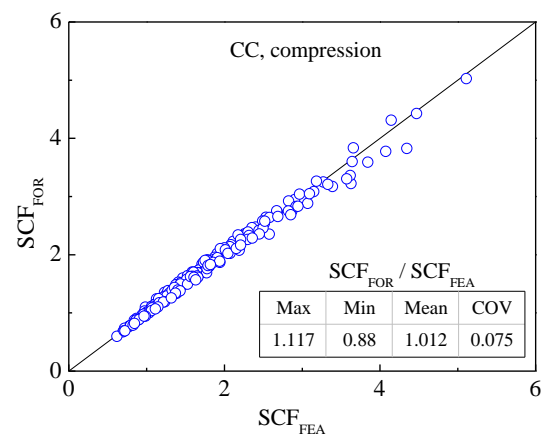
(f) CC: axial compressive fore in brace
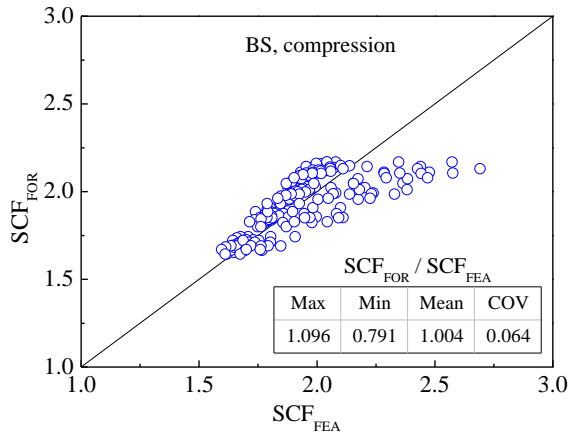
(g) BS: axial compressive fore in brace   (h) BC: axial compressive fore in brace
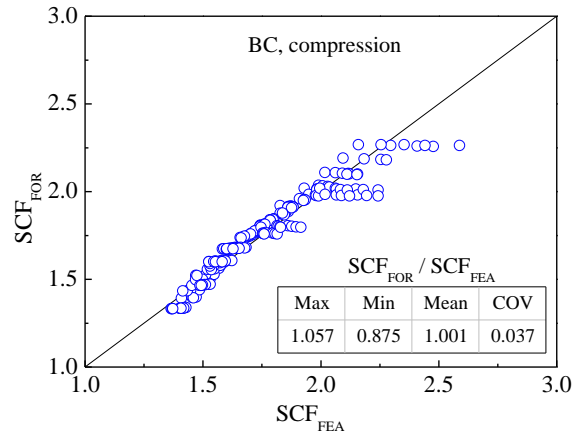
Fig. 4.20 Comparison of SCF$_{FOR}$ with SCF$_{FEA}$

However, conspicuous disagreements and different trends are observed at locations CS and BS under compressive axial force. In order to examine the reason, **Figs. 4.20(e)** and **(g)** are divided into three graphs by α-value, respectively, as shown in **Fig. 4.21**. Then, most different trends disappear. It indicates that the different trends are mainly caused by ignoring the influence of α-value in the developed formulae for locations CS and BS. Although the accuracy can be improved by considering the influence of α-value, the authors do not think that it is necessary due to much smaller SCFs than those at the same locations under tension.

(a) $\alpha = 12$

(b) $\alpha = 16$

(c) $\alpha = 20$
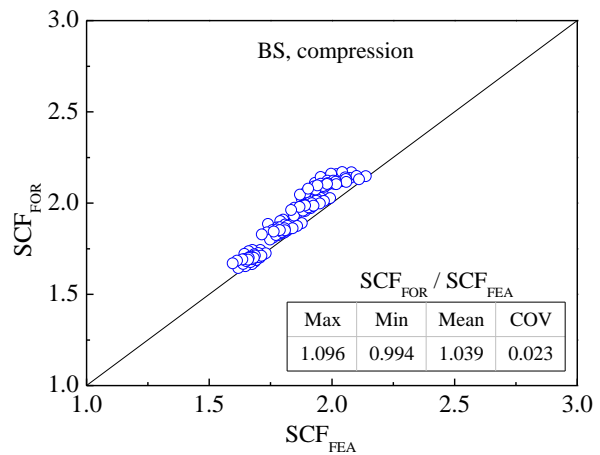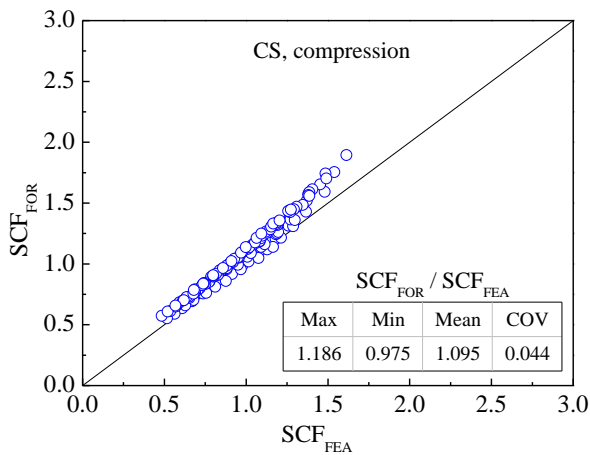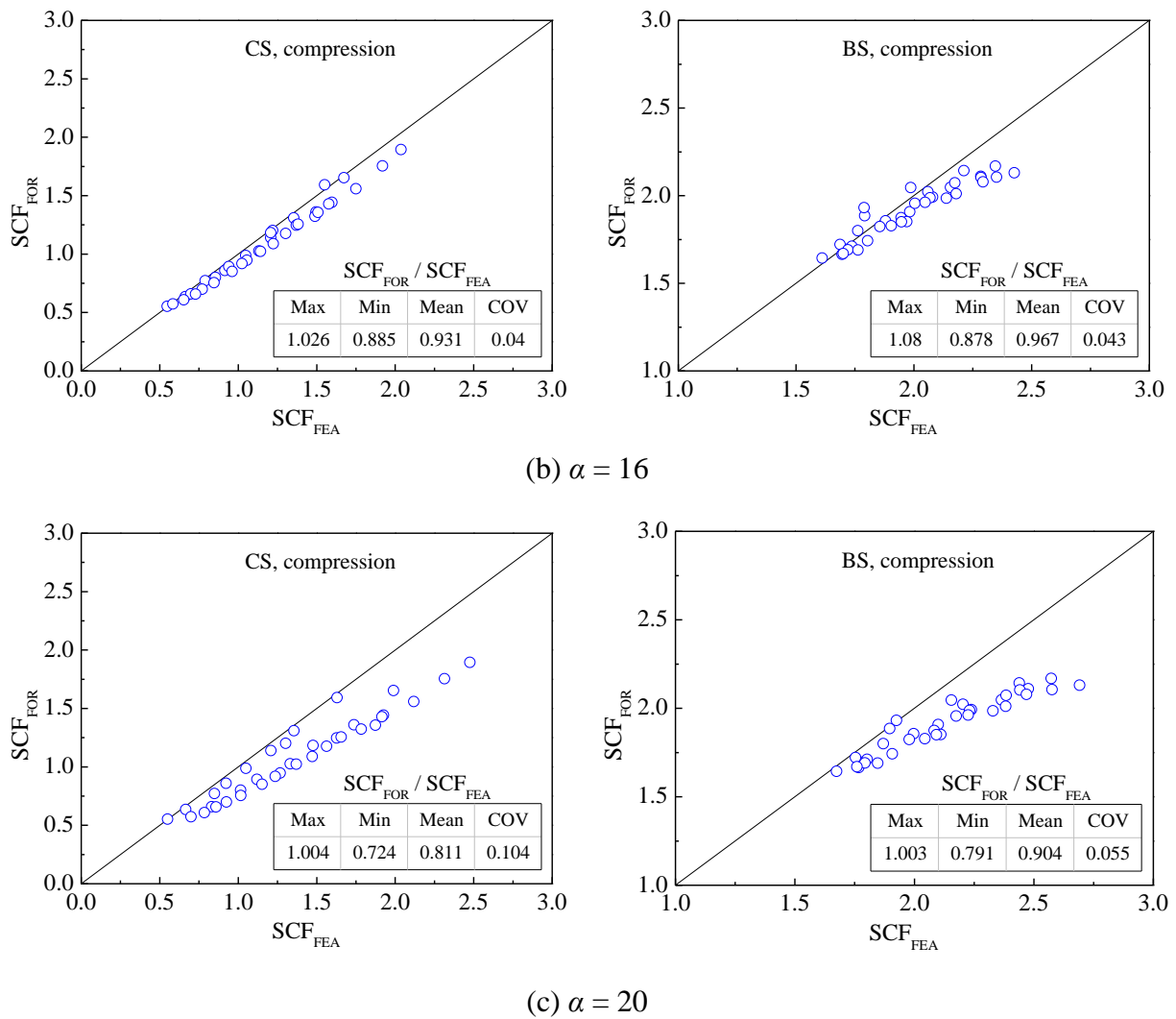
Fig. 4.21 Comparison of SCF_{FOR} with SCF_{FEA} at locations CS and BS under compression for each α-value

Therefore, it can be concluded that the proposed SCFs formulae in **Eqs. (4.13)-(4.16)** have sufficient accuracy and reliability for CFST T-joints under axial force in the brace.

(2) The rest loading conditions

SCFs obtained using the proposed formulae, SCF_{FOR}, were compared with those from FE analysis, SCF_{FEA}, for all locations so as to verify the accuracy of the formulae. The results are shown in **Fig. 4.22**. Also shown in the figure are statistical measures of the ratio SCF_{FOR}/SCF_{FEA}. Overall, there is good agreement between the two sets of SCFs. The mean values of SCF_{FOR}/SCF_{FEA} listed in **Fig. 4.22** are very close to 1.0 for all locations, and the corresponding coefficients of variance (COV) are relatively small. Therefore, it can be concluded that the proposed SCF formulae in **Eqs. (4.17)-(4.22)** have

sufficient accuracy and reliability for CFST T-joints under the four loading conditions analyzed.

(a) SCF_{CC} under IPB in the brace

(b) SCF_{BC} under IPB in the brace

(c) SCF_{CS} under OPB in the brace

(d) SCF_{BS} under OPB in the brace

(e) SCF_{CC} under axial force in the chord

(f) SCF_{CC} under IPB in the chord
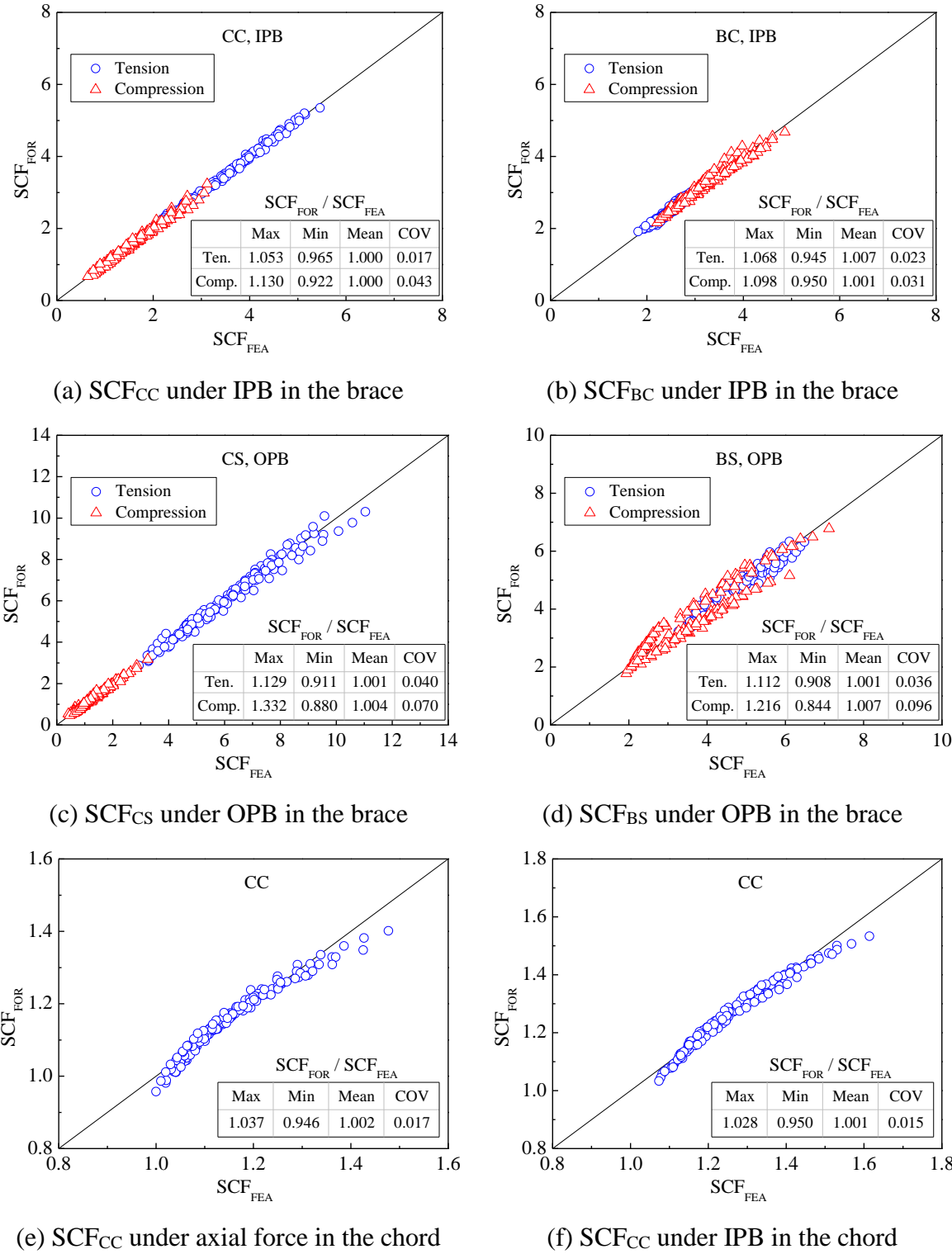
Fig. 4.22 Comparison of SCF_{FOR} with SCF_{FEA}

4.5 Summary

This study focuses on the SCFs of CFST T-joints under six loading conditions, i.e. axial tension in the brace; axial compression in the brace; in-plane bending (IPB) in the brace; out-of-plane bending (OPB) in the brace; axial compression in the chord; IPB in the chord. Parametric analysis was conducted by using the validated FE model to reveal the effects of the key four non-dimensional geometric parameters (β, 2γ, τ and α) on the SCFs. Based on the numerical results from 424 FE analyses, a series of parametric formulae were proposed to determine the SCFs of CFST T-joints. The main conclusions are summarized as follows.

(1) The influences of non-dimensional geometric parameters (β, 2γ, τ and α) on SCFs of CFST T-joints under six loading conditions have been revealed. Moreover, the influence of τ on the SCFs is generally larger than that of β, 2γ and α in most cases.

(2) The SCFs in the chord caused by axial tension in the brace are much larger than that under axial compression in the brace. The maximum SCFs in the chord generally occur at locations CS and CC under axial tensile and compressive force, respectively. The maximum SCFs in the brace occur at location BS under axial tensile force in general. However, they can occur at locations BS or BC under axial compressive force.

(3) The SCFs along the intersection of tensile side under in-plane or out-of-plane bending in the brace are in general much larger than that on compressive side. The maximum SCFs under in-plane and out-of-plane bending in the brace usually occur at locations CC and CS both on tensile side, respectively. Under the axial compressive force or in-plane bending in the chord, they usually occur at location CC.

(4) Using multiple regression analysis, parametric formulae to determine the SCFs for CFST T-joints under six loading conditions were developed. Sufficient accuracy and reliability of the proposed formulae were demonstrated by comparison with FE analysis results.

CHAPTER 5

Formulation of SCFs for CFST K-joints under Various Loading Conditions

5.1 Introduction

In present, there has been very limit effort to develop SCF formulae for CFST K-joints. Tong et al. [75] experimentally investigated the SCFs of CFST K-joints, and revealed that they have more uniform distribution and obviously smaller values than those of CHS K-joints. Udomworarat et al. [82, 83] revealed that CFST K-joints have less SCFs values than CHS K-joints by using the experimental and finite element (FE) methods. Huang et al. [84] also experimentally found that CFST K-joints have more uniform and lower peak strain than those in CHS K-joints with the same geometry by comparison of their principal strain distributions around the chord-brace intersections. Nevertheless, the SCF formulae for CFST K-joints have been not proposed because of few studies devoted to the SCFs determination. Moreover, the validity ranges of diameter to thickness ratio of chord (2γ) in [75] and thickness ratio (τ) in [81] do not match the practical ranges of bridge structures. Therefore, the development of a series of parametric formulae for calculating SCFs has been awaited to simplify HSS calculations for CFST K-joints.

In this chapter, a case-based analysis was carried out by employing the local CFST K-joint in a half-through CFST trussed arch bridge under the loading of a fatigue vehicle. The loading conditions of parametric analysis include the basic balanced axial forces, axial compressive force in the chord and in-plane bending in the chord. Based on the results of parametric analysis, parametric formulae to determine SCF were proposed as functions of four key geometric parameters (see **Fig. 5.1**), i.e. the diameter ratio β ($= d/D$), diameter to thickness ratio of chord 2γ ($= D/T$), thickness ratio τ ($= t/T$) and the angle (θ) between the axis of the chord and brace. Finally, the accuracy of parametric formulae was verified by comparing with the FE results.

(a) Three-dimensional diagram   (b) Geometric parameters
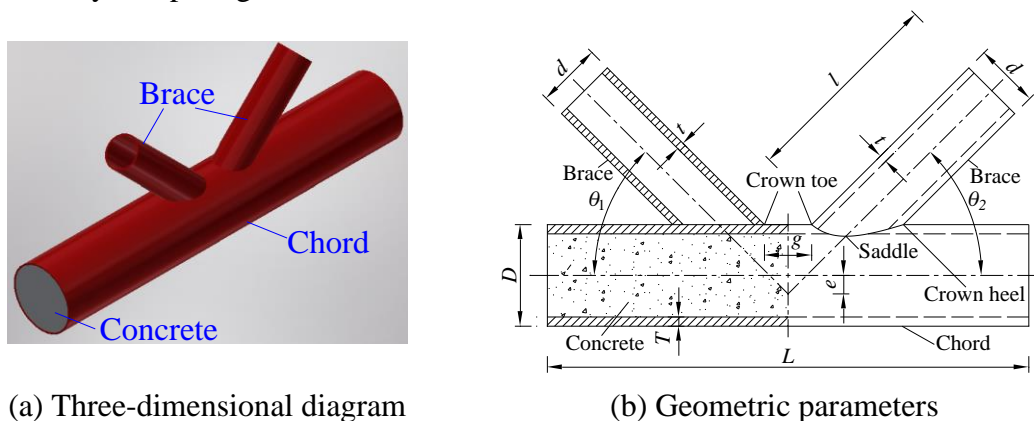
Fig. 5.1 Geometric parameters of CFST K-joints

5.2 Case-based analysis

In this section, case-based analysis to reveal the influences of five geometric parameters on SCFs corresponding to hot spot stress (HSS) of CFST K-joints in a half-through CFST trussed arch bridge under the loading of a fatigue vehicle was performed under axial force in the chord and braces. The information of half-through CFST trussed arch bridge was described in [5]. The geometric parameters considered are diameter ratio ($\beta = d/D$), diameter to thickness ratio of chord ($2\gamma = D/T$), thickness ratio ($\tau = t/T$), the angle (θ) between chord and brace, and the eccentricity ratio ($\rho = e/D$) (see **Fig. 5.1**). The results were discussed aiming at revealing their influence on SCFs for CFST K-joint in the bridge.

5.2.1 FE modelling

(1) FE models

A general-purpose FE analysis software MSC.Marc was used for the analysis. FE models were applied to the numerical investigation of HSS distribution of CFST K-joints under axial force. Young's modulus of steel tube and concrete was set to 2.05×10^5 MPa and 3.25×10^4 MPa, and their Poisson's ratio was set to 0.3 and 0.2, respectively, which were same as the design values for the half-through CFST trussed arch bridge. The material properties same as the steel tube were assigned to the weld bead. An average weld size at the brace and chord of t and $0.5t$, respectively, was used for the modelling of weld bead.

The settings used in the FE models for the element types, the mesh specifications and generation process, and the modeling of the chord tube-concrete interface are the same as in Chapter 3. The linear full-integration 8-node hexahedron solid element with "assumed strain" was used for the whole model, i.e. steel tube, concrete and weld bead. The element layers in the tube thickness direction were determined so that the edge length ratio of elements around the intersection is approximately 1, and the mesh size of approximately 2 mm was used for the elements around the intersection.

The interface behavior between chord tube and concrete was simulated by "Touch" functions. It allows that contact bodies can touch and separate each other in normal direction and slide with the friction behavior in tangential direction. The friction coefficient $\mu = 0.3$ was arbitrarily adopted since the effect of μ on SCF of CFST joints can

be neglected. One chord end is fixed. Another chord end and two brace ends are free. The axial tensile and compressive forces applied to the braces were 37.50 kN, and the axial compressive force applied to the chord was 109.84 kN. These values were determined referring to the analysis results for the bridge in which fatigue cracks were found under the loading of a fatigue vehicle [5]. The FE model and local mesh around the intersection are shown in **Figs. 5.2** and **5.3**, respectively.
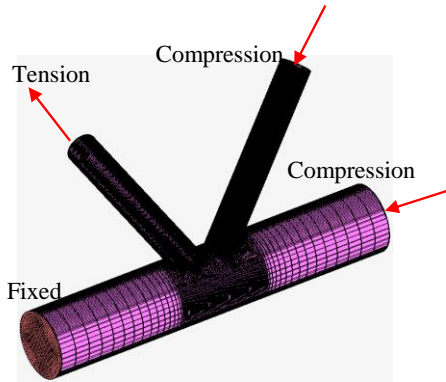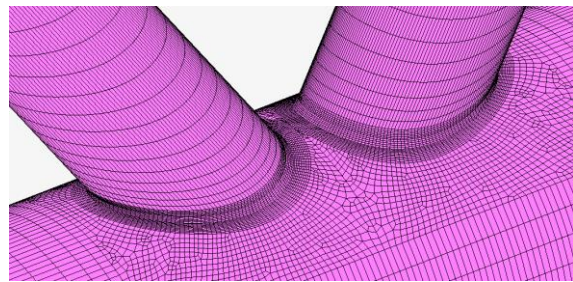
| **Fig. 5.2** FE model | **Fig. 5.3** Local mesh around the intersection |

(2) HSS and SCFs calculation

The determination method of HSS around the chord-brace intersection was obtained numerically by linear extrapolation. The boundaries of extrapolation region and the definition of SCFs is same to the description in Chapter 3. The nominal stress σ_n of CFST K-joints caused by the axial force F_b in the brace was determined using a simple formula ($\sigma_n = F_b / A$), where A is the cross-sectional area of the brace.

(3) Dimensions of FE models

The geometric dimensions of standard FE model are shown in **Table 5.1**. The ranges of each parameter for parametric analysis are $\gamma = [20, 40]$, $\tau = [0.4, 1.0]$, $\beta = [0.3, 0.45]$, $\theta = [30°, 57°]$ and $\rho = [-0.13, 0.43]$, respectively. When changing the value of one parameter in the parametric analysis, the value of other parameters is fixed to the same value as the standard model. In total, 19 FE models were prepared and analyzed, the detailed parameter combinations of FE models in the parametric study are shown in **Table 5.2**.

Table 5.1 Standard model of CFST K-joint

Structural dimensions				
D/mm	d/mm	T/mm	t/mm	θ/°
550	219	8	8	57
Dimensionless parameters				
γ	τ		β	ρ
34.38	1.0		0.4	0

Table 5.2 Values of each parameter

Parameters	Values						
γ	20		30	34.38		40	
τ	0.4		0.6	0.8		1.0	
β	0.30		0.35	0.40		0.45	
θ	30°		40°	50°		57°	
ρ	-0.13	-0.11	-0.09	-0.045	0	0.09	0.43

5.2.2 Results and discussions

(1) Comparison between CFST and CHS

The maximum SCFs along the chord-brace intersection in both CFST and CHS K-joints were obtained by FE analysis. The deformation around the chord-brace intersection in CFST K-joints is illustrated in **Fig. 5.4**. The mechanical behavior around the intersection with tensile brace in CFST K-joints is considered to be similar to that in CHS K-joints since the separation between chord tube and concrete occurs. However, the concrete can provide strong support for chord tube against compression in the brace. The contact surface between chord tube and concrete at location crown toe is flatter, which leads to bear more loads than other locations. Therefore, the maximum SCF of the chord with tensile brace in CFST K-joints generally occurs at location saddle, which is the same as that in CHS K-joint. But it occurs at location crown toe in the chord with compressive brace in CFST K-joints.
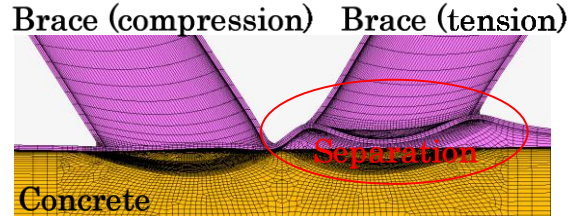
Fig. 5.4 Amplified deformation between chord tube and concrete

The SCF parametric formula for CHS K-joints in the CIDECT Design Guide [14] is shown in **Eq. (5.1)**.

$$\mathrm{SCF} = [\frac{\gamma}{12}]^{\chi_1}[\frac{\tau}{0.5}]^{\chi_2} \cdot \mathrm{SCF_o} \qquad (5.1)$$

The exponents χ_1, χ_2 depend on the loading type and the location of interest. The value of χ_1, χ_2 and $\mathrm{SCF_0}$ are given in Appendix D of the design guide [14]. The validity ranges of the formula are $2\gamma = [24, 60]$, $\tau = [0.25, 1.00]$, $\beta = [0.30, 0.60]$, $\theta = [30°, 60°]$. It should be noted that 2γ-value of some models in this study is a little larger than the applicable range.

The maximum SCFs along the chord-brace intersection in CHS joint obtained by FE analysis were compared with those calculated using **Eq. (5.1)**, as shown in **Figs. 5.5-5.8**. The maximum SCFs only of the chord are shown in the figures since the SCFs of chord are larger than those of braces in both CFST and CHS joints. The SCFs by **Eq. (5.1)** show good agreement with those by FE analysis.

Figs. 5.5-5.9 also show the comparison of the maximum SCFs in CFST joint with those in CHS joint, and it indicates the maximum SCFs in CFST joint are much smaller than that in CHS joint, especially the maximum SCFs around the intersection with compressive brace. In addition, the influence of each parameter on the maximum SCFs around the intersection with tensile brace in CFST joint is similar to those in CHS joint. Meanwhile, the influence of γ-, β- and ρ-values on the maximum SCFs around the intersection with compressive brace in CFST joint was different from those in CHS joint.
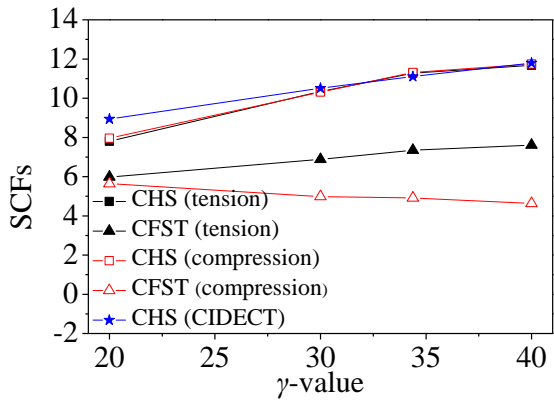
Fig. 5.5 Maximum SCF versus γ
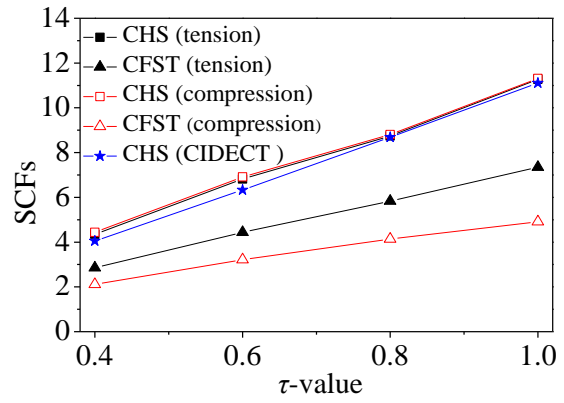
Fig. 5.6 Maximum SCF versus τ
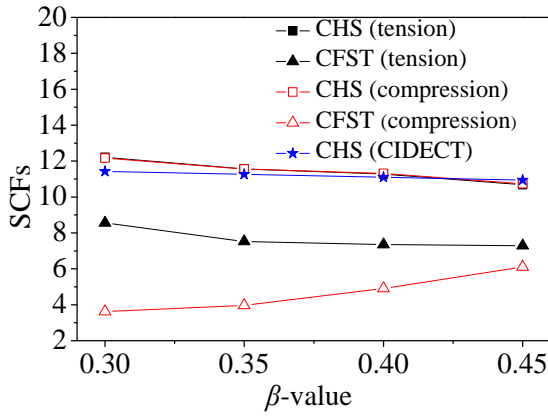
Fig. 5.7 Maximum SCF versus β
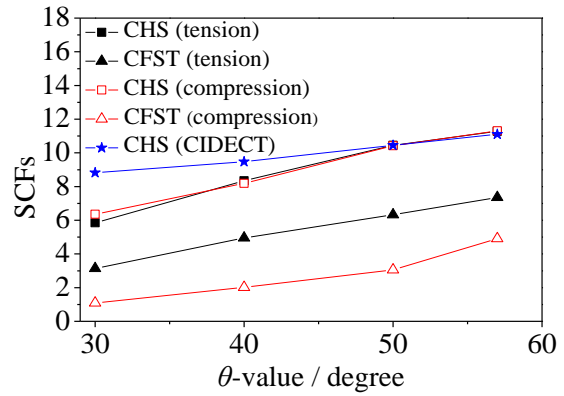
Fig. 5.8 Maximum SCF versus θ
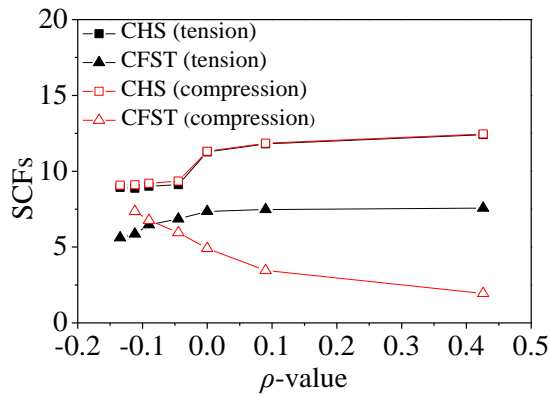
Fig. 5.9 Maximum SCF versus ρ

(2) Influence of parameters in CFST joint

(a) Influence of γ (= $D/2T$) on maximum SCF

With the increase of γ-value, the maximum SCF increases with the slope of 0.0815 around the intersection with tensile brace in CFST K-joints, whereas it decreases with the slope of -0.0505 around the intersection with compressive brace as shown in **Fig. 5.5**.

Under unchanged D-value and τ-value, the T-value and t-value decrease with increasing γ-value. The decrease of T-value results in the decrease of local stiffness of the chord around the intersection with the tensile brace against bending, which makes the hot spot stress (HSS) in the chord larger since the separation occurs there. The decrease of t-value results in the increase of the nominal stress under unchanged axial force. The increasing degree of the HSS may be larger than that of the nominal stress since the decreasing degree of bending stiffness is generally larger than that of axial stiffness with the decrease of thickness. It can cause higher stress concentration.

However, the local stiffness of the chord around the intersection with the compressive brace against bending hardly decreases due to the strong support by concrete infill. Therefore, the HSS also hardly decreases. Since the nominal stress becomes larger with the increase of γ -value, the stress concentration becomes smaller.

(b) Influence of τ ($= t/T$) on maximum SCF

With the increase of τ-value, the maximum SCFs increase with the slopes of 3.92 and 4.67 around the intersections with tensile and compressive braces in CFST K-joints, respectively, as shown in **Fig. 5.6**.

It can be caused by the change of relative stiffness between the chord and brace. The t-value increases relative to the T-value with the increasing τ-value. Local stiffness of the chord around the intersection reduces relative to that of the brace, leading to higher stress concentration in the chord.

(c) Influence of β ($= d/D$) on maximum SCF

With the increase of β-value, the maximum SCF decreases with the slope of -8.47 around the intersection with tensile brace in CFST K-joints, whereas it increases with the slope of 16.53 around the intersection with compressive brace as shown in **Fig. 5.7**.

The increase of β-value results in the decrease of the nominal stress and HSS under unchanged axial force. The decreasing degree of the maximum HSS around the intersection with the tensile brace, which occurs at the saddle, may be larger than that of the nominal stress since the local bending deformation induced by the component of force

perpendicular to the chord surface becomes smaller with the increase of β-value. Consequently, the stress concentration becomes smaller.

However, the maximum HSS around the intersection with the compressive brace, which occurs at the crown toe, hardly decreases since g-value becomes smaller and the stress transfer between the chord and tensile brace becomes less uniform with the increase of β-value. Consequently, the stress concentration becomes larger. The influence of g-value on the maximum SCF is explained in **(e)**.

(d) Influence of θ on maximum SCF

With the increase of θ-value, the maximum SCFs increase with the slopes of 0.16 and 0.14 around the intersections with tensile and compressive braces in CFST K-joints, respectively, as shown in **Fig. 5.8**. The vertical component of force in brace increases from $0.5F$ to $0.84F$ with the increasing θ from 30° to 57°, i.e. the vertical component becomes 1.68 times. The SCFs around the intersections with tensile and compressive braces become 2.34 and 4.50 times. The change of SCFs can be mainly caused by the change of the vertical component of force in the brace, and caused by the change of g-value under different θ-value together. The g-value decrease from 515 mm to 96 mm with the increasing θ from 30° to 57°, i.e. the g-value becomes 1/5.36 times. The influence of g-value on the maximum SCF is explained in **(e)**.

(e) Influence of ρ (= e/D) on maximum SCF

With the increase of ρ-value, the maximum SCF decreases with the slope of -9.66 around the intersection with compressive brace in CFST K-joints, whereas it increases with the slope of 3.48 around the intersection with tensile brace as shown in **Fig. 5.9**.

The hot spot of chord tube with the compressive brace under different ρ-value always locates around crown toe since the combined action of both the flatter contact surface and the bending deformation around crown toe induced by the separation under the small ρ-value, the bending deformation around crown toe is shown in **Fig. 5.9**. When the ρ-value is small, the separation between chord tube and concrete under tension not only occurs below the tensile brace but also compressive brace, as illustrated in **Fig. 5.10**. When the ρ-value is very large, the separation only occurs below the tensile brace, and the influence of separation on the chord tube with compressive brace can be neglected. The stress concentration around the intersection with compressive brace can be relieved since the

strong support from concrete without the separation.

The hot spot of the chord tube with tensile brace under different ρ-values always locates around saddle since it has the large out-of-plane bending deformation as shown in **Fig. 5.10**. When the ρ-value becomes large, the gap becomes also large and two braces can be further away from each other. The out-of-plane bending deformation of chord tube around the intersection becomes larger, which induces higher stress concentration of chord with tensile brace.

(a) $\rho = -0.13$, $g = 0$

(b) $\rho = -0.045$, $g = 8t$

(c) $\rho = 0.43$, $g = 50t$
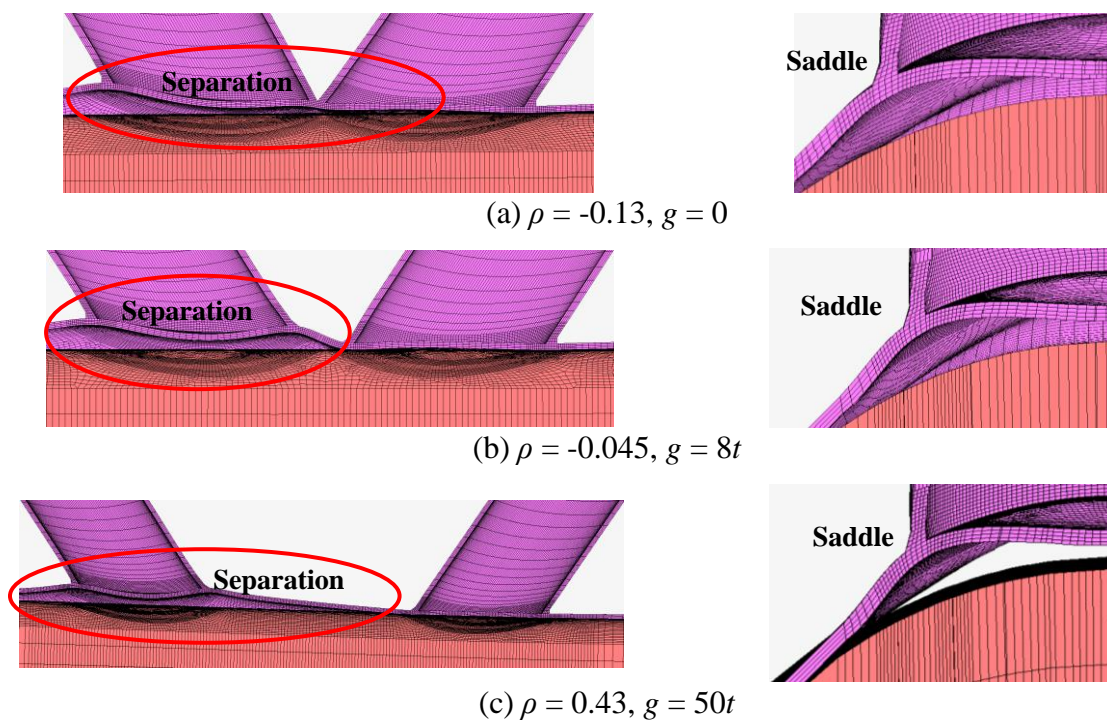
Fig. 5.10 Amplified deformation between chord tube and concrete under different ρ-value

(f) Summary of parametric analysis

The influences of the geometric parameters on SCFs of CFST K-joint can be summarized in **Table 5.3**. The influence of β on SCFs is the most significant among the five parameters since it has the most largest curve slope. In addition, the influence of γ on SCFs is very little since it has the minimal curve slope.

Table 5.3 Influences of geometric parameters on maximum SCF

Geometric parameters	Tension		Compression	
	SCFs	Slope	SCFs	Slope

γ-value	20 → 40 (↗)	5.98 → 7.61 (↗)	0.0815	5.64 → 4.63 (↘)	-0.0505
τ-value	0.4 → 1.0 (↗)	5.00 → 7.35 (↗)	3.92	2.11 → 4.91 (↗)	4.67
β-value	0.30 → 0.45 (↗)	8.56 → 7.29 (↘)	-8.47	3.62 → 6.10 (↗)	16.53
θ-value	30° → 57° (↗)	3.14 → 7.35 (↗)	0.16	1.09 → 4.91 (↗)	0.14
ρ-value	-0.13→0.43 (↗)	5.62 → 7.57 (↗)	3.48	7.35 → 1.94 (↘)	-9.66

Where, → is from one value to other value, ↗ is increasing, ↘ is decreasing.

5.3 Parametric analysis on SCFs

5.3.1 FE modelling

(1) FE models

The SCF formulae for CHS K-joints [14] and the published experimental researches [75] indicate that the parameters β, 2γ, τ and θ are the key to determination of SCFs for CFST K-joints. Ranges of the four key parameters for the parametric analysis were set to $\beta = [0.3 - 0.6]$, $2\gamma = [40 - 80]$, $\tau = [0.4 - 1.0]$ and $\theta = [30° - 60°]$ based on the geometric parameters statistics of CFST K-joint in 119 CFST trussed arch bridges in Chapter 2. Besides the above limitations, some other limitations are also adopted for the parametric analysis, i.e. (1) equal braces; (2) equal angles between the axis of the chord and braces ($\theta = \theta_1 = \theta_2$); (3) no eccentricity ($e = 0$ or $\rho = 0$); (4) the gaps are positive ($g > 0$), but $\geq$ $2t$; (5) full penetration butt welds are adopted for the chord-brace intersection.

The combination of geometric parameters is listed in **Table 5.4**. A total of 272 models, 240 models for developing SCF formulae and 32 models for additional validation of the formulae, were prepared. The geometric dimensions of the standard FE model were set in reference to the typical dimensions of CFST trussed arch bridges [4], as shown in **Table 5.5**. Length of the brace (l) and length of the chord (L) were unchanged during the parametric analysis at $3d$ and $6D$, respectively. The leg sizes of weld bead at the brace and chord were set to t and $0.5t$, respectively, according to AWS code [17].

Table 5.4 Combination of geometric parameters

Number of Models	$\theta/°$	β	2γ	τ
240	30, 45, 60	0.3, 0.4, 0.5, 0.6	40, 50, 60, 70, 80	0.4, 0.6, 0.8, 1.0
32	35, 40, 50, 55	0.3, 0.4, 0.5, 0.6	40, 80	1.0

Table 5.5 Geometric parameters of standard FE model

Structural dimensions						
D/mm	d/mm	T/mm	t/mm	L/mm	l/mm	$\theta/°$
600	300	15	6	3600	900	45
Non-dimensional geometric parameters						
β		2γ		τ		ρ
0.5		40		0.4		0

The existing researches [78] presented that the effect of Young's modulus of common-used concrete on the SCFs of CFST joints was not significant, even can be neglected. Since concrete with the strength between 30 and 60 MPa has been applied to the arch ribs of CFST arch bridges in China [4], the concrete of 50 MPa grade was assumed for the determination of Young's modulus of concrete [102]. The load in the concrete-filled chord was applied through the loading rigid plates set at the chord ends. The thickness of loading rigid plates are 20 mm, and their diameters are the same as the chord diameter (*D*). Linear elastic analysis in terms of material properties was applied. The material properties were set as shown in **Table 5.6**.

Table 5.6 Material Properties for parametric analysis

Material	Young's modulus (MPa)	Poisson's ratio
Steel tube and weld bead	2.05×10^5	0.3
Concrete	3.45×10^4	0.2
Loading rigid plate	1.00×10^8	0.3
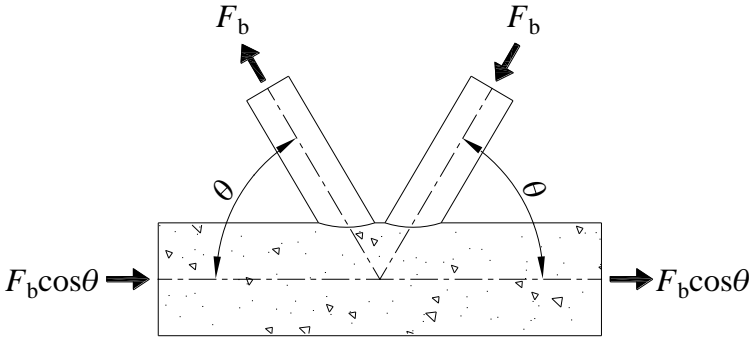
The setting used in the FE models for the element types, the mesh specification and
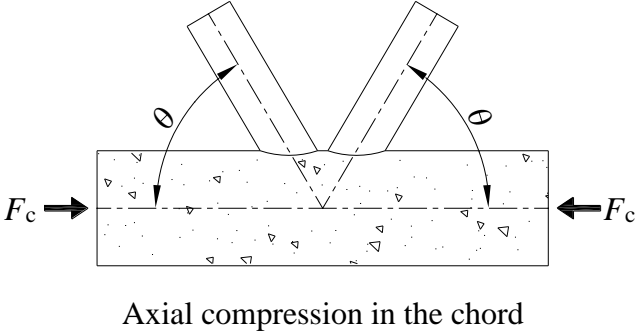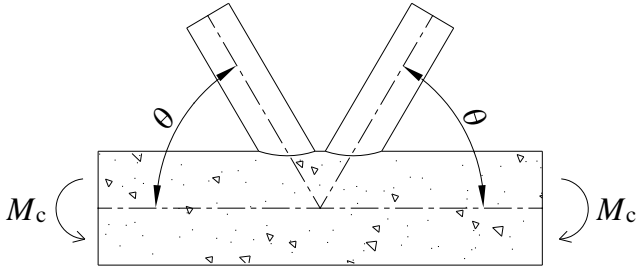
generation process, the modeling of the chord tube-concrete interface, and the modeling of the interface between loading rigid plate and concrete-filled chord are the same as those described in Section 3.3. The chord is simply supported.

(2) Loading conditions

In general, the braces mainly bear axial forces and the chords bear axial compression and in-plane bending in the arch ribs of CFST trussed arch bridges. Therefore, three loading conditions were taken into account for parametric analysis referring to those for CHS K-joints in [14]: (1) basic balanced axial forces; (2) axial compression in the chord; (3) in-plane bending in the chord. Under basic balanced axial forces, the maximum SCFs can occur at following locations; chord crown toe (CC), chord saddle (CS), chord crown heel (CH) around the tensile and compressive braces, and brace crown toe (BC) brace saddle (BS) and brace crown heel (BH) in tension and compression. Axial compression and in-plane bending in the chord always induce the maximum SCFs at location CC or CH, while the SCFs at other locations are very small. Therefore, the SCFs were calculated at these locations. The loading conditions and their associated hot spot locations are shown in **Table 5.7**. The values of F_b, F_c and M_c in **Table 5.7** are 2×10^5 N, 1×10^6 N and 1×10^8 N·mm, respectively.

Table 5.7 Loading conditions and their hot spot locations

Loading condition	Hot spot locations
Basic balanced axial forces	CC, CS, CH BC, BS, BH

 Axial compression in the chord	CC, CH
 In-plane bending in the chord	CC, CH

(3) HSS calculation and definition of SCFs

The determination method of HSS around the chord-brace intersection was obtained numerically by linear extrapolation. The boundaries of extrapolation region and the definition of SCFs is same to the description in Chapter 3.

Refering to the nominal stress for CHS K-joints [104], the nominal stresses of CFST K-joints under the basic balanced axial forces, axial compression in the chord (F_c) and In-plane bending moment in the chord (M_c) were determined as F_b / A_b, F_c / A and M_c / W, respectively. A_b is the area of the brace tube section. A and W are the area and section modulus of the equivalent steel tube section of the concrete-filled chord, respectively.

5.3.2 Results and discussions

(1) Hot spot of each member under basic balanced axial forces

The position of hot spot in each member along the chord-brace intersection under basic balanced axial forces is summarized in **Table 5.8**. In general, the hot spot in the chord is mainly at either location CC or CS around the tensile brace, and always at location CC around the compressive brace. The hot spot locations in the tensile brace vary depending on the joint parameters. The location BC or BS is, however, often the hot spot. In the compressive brace, the hot spot is mainly at either location BC or BH.

By comparing the SCF among the hot spot in each member, it can be observed that the maximum SCF generally occurs at the chord around the tensile brace, which is much larger than that around the compressive brace. Due to low adhesion between the chord tube and concrete, the inner wall of chord would tend to separate from the concrete filling around the chord-brace intersection under tensile brace, while the concrete filling would provide strong support for the chord wall under the compressive brace, as illustrated in **Fig. 5.11**. Consequently, local bending deformation around the intersection under tension is much larger than that under compression, resulting in higher SCF under tension than that under compression. The hot spot positions between the intersections under tension and compression can be different by the influence of concrete filling and the behavior of the chord tube-concrete interface explained above. Hence, the SCF formulae need to be developed independently for each possible hot spot position.

Table 5.8 Distribution of hot spot position in each member under basic balanced axial forces

Chord (tension)			
Location	CC	CS	CH
Percentage	55%	45%	0%
Chord (compression)			
Location	CC	CS	CH
Percentage	100%	0%	0%
Brace (tension)			
Location	BC	BS	BH
Percentage	35%	41%	24%
Brace (compression)			
Location	BC	BS	BH
Percentage	59%	0%	41%
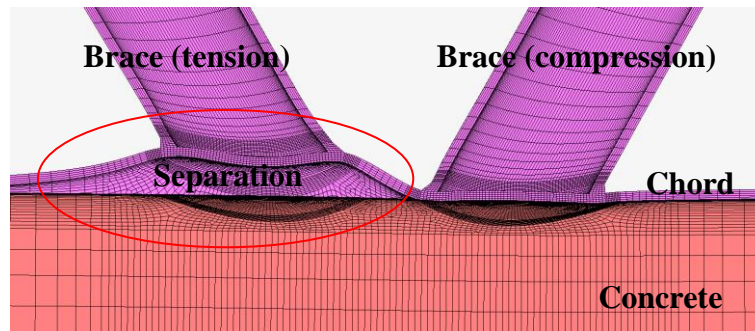
Fig. 5.11 Amplified deformation between chord tube and concrete

(2) Comparison of SCF between locations CC and CH under chord loading

The position of hot spot in each member along the chord-brace intersection under chord loading is summarized in **Table 5.9**. In general, the hot spot in the chord is at either location CC or CH, but mainly at location CH.

Table 5.9 Distribution of hot spot position under the chord loading

Under axial compression in the chord		
Location	CC	CH
Percentage	32%	68%
Under in-plane bending in the chord		
Location	CC	CH
Percentage	36%	64%

The hot spot can occur at location CC or CH under the chord loading. The comparisons of SCFs between locations CC and CH under the chord loading are shown in **Fig. 5.12**. It can be observed that the SCFs at locations CC and CH are not very different. The mean of their ratio is close to 1 and their maximum difference is approximately 20%. Considering relatively small SCF-values, it can be thought that independent formulation of SCFs for both locations is not necessary.
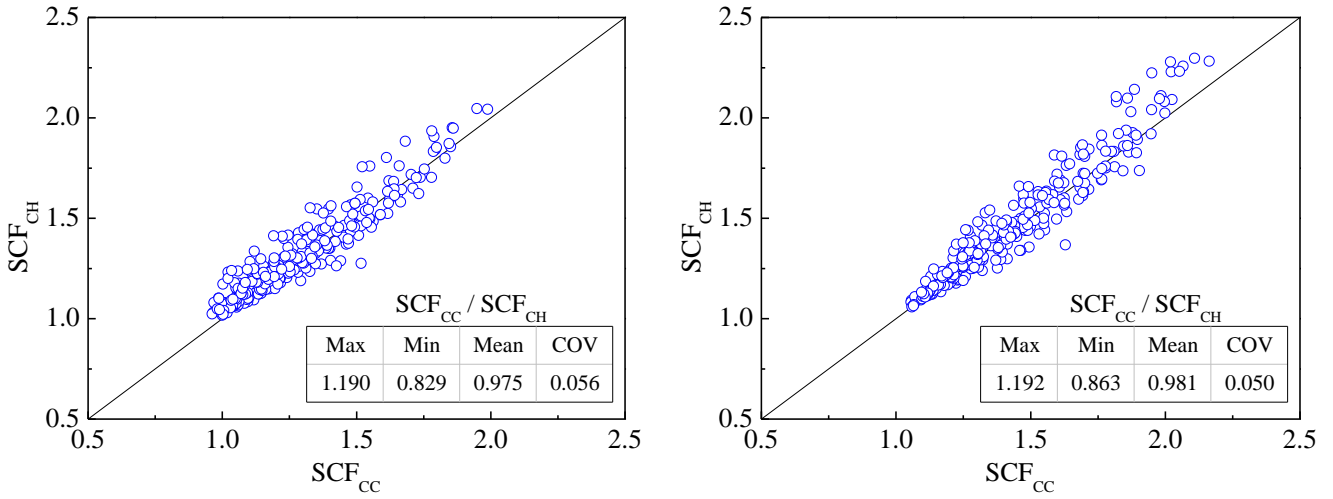
(a) Under axial compression in the chord   (b) Under in-plane bending in the chord

Fig. 5.12 Comparison of SCFs between locations CC and CH

5.4 Proposed formulae and their accuracy verification

5.4.1 Formulation

A typical SCF formula can be expressed in the form of **Eq. (5.2)** based on the proposed parametric formulae for CHS K-joints in CIDECT Design Guide [14, 105], which forms the basis of the multiple regression analysis for the parametric formulae proposed in this study.

$$\text{SCF} = \mu \left(\frac{\gamma}{\gamma_0} \right)^a \left(\frac{\tau}{\tau_0} \right)^b \text{SCF}_0 \qquad (5.2)$$

Where, γ_0 and τ_0 are determined from the standard CFST K-joint in **Table 5.5**, i.e. $\gamma_0 = 20$ and $\tau_0 = 0.4$; SCF_0 is the SCF obtained from the basic combination of geometric parameters, which is a function of parameter β and obtained using a second order polynomial; The constants μ, the exponents a and b would be determined by the multiple regression analysis.

Since the results of the parametric analysis are obtained for the sets of $\theta = 30°$, $45°$ and $60°$, the multiple regression analysis using the FE results of 240 models with $\theta = 30°$, $45°$ and $60°$ in **Table 5.4** has been carried out for each loading condition, location and θ-value. Their results are given in **Table 5.10**.

Table 5.10 Proposed SCF formulae of CFST K-joints

Loading condition	Location		θ (°)	μ	a	b	SCF_0
Under basic balanced axial forces	Chord (ten.)	CC	30	0.565	0.693	0.637	$-1.453\beta^2 + 2.011\beta + 1.539$
			45	0.815	0.425	0.806	$5.185\beta^2 - 3.154\beta + 2.438$
			60	1.025	0.337	0.928	$-3.322\beta^2 + 3.711\beta + 1.169$
		CS	30	0.395	0.508	0.997	$0.617\beta^2 - 1.634\beta + 2.730$
			45	0.687	0.561	1.016	$0.939\beta^2 - 2.299\beta + 2.965$
			60	1.024	0.498	1.031	$-0.962\beta^2 - 0.857\beta + 2.729$
		CH	30	0.157	1.042	-0.434	$7.204\beta^2 - 10.020\beta + 5.185$
			45	0.316	0.755	0.513	$5.151\beta^2 - 4.977\beta + 3.259$
			60	0.488	0.691	0.958	$-1.822\beta^2 + 2.704\beta + 1.306$
	Chord (comp.)	CC	30	0.263	0.359	0.439	$0.964\beta^2 + 0.653\beta + 1.645$
			45	0.471	-0.115	0.743	$12.924\beta^2 - 6.421\beta + 2.365$
			60	0.720	-0.214	0.902	$-3.554\beta^2 + 0.881\beta + 2.519$
		CS	30	0.126	-0.309	0.866	$2.944\beta^2 - 3.567\beta + 3.097$
			45	0.216	-0.086	0.867	$-3.597\beta^2 + 3.281\beta + 1.419$
			60	0.329	-0.113	0.908	$-0.147\beta^2 - 1.658\beta + 2.916$
		CH		SCFs can be de neglected since their values are very small.			
	Brace (ten.)	BC	30	0.651	0.072	-0.153	$8.506\beta^2 - 8.748\beta + 4.239$
			45	1.061	-0.080	-0.198	$20.160\beta^2 - 18.630\beta + 6.190$

			60	1.233	-0.125	-0.187	$6.487\beta^2 - 7.780\beta + 4.250$
		BS	30	0.200	-0.236	1.144	$15.960\beta^2 - 19.725\beta + 7.708$
			45	0.537	0.225	0.618	$12.380\beta^2 - 13.768\beta + 5.694$
			60	0.908	0.307	0.487	$8.084\beta^2 - 9.048\beta + 4.474$
		BH	30	0.629	-0.426	0.554	$4.446\beta^2 - 5.503\beta + 3.655$
			45	0.795	-0.196	-0.352	$4.973\beta^2 - 5.919\beta + 3.729$
			60	0.797	0.093	-0.201	$3.731\beta^2 - 4.086\beta + 3.163$
	Brace (comp.)	BC	30	0.473	0.205	-0.182	$0.207\beta^2 + 2.233\beta + 1.101$
			45	0.663	0.094	0.096	$7.712\beta^2 - 4.656\beta + 2.586$
			60	0.841	-0.031	0.122	$-1.410\beta^2 + 0.857\beta + 2.039$
		BS	30	0.101	-1.261	1.112	$11.957\beta^2 - 21.465\beta + 9.745$
			45	0.303	-0.395	0.285	$0.640\beta^2 - 4.815\beta + 4.243$
			60	0.500	-0.172	0.159	$1.567\beta^2 - 3.451\beta + 3.358$
		BH	30	0.605	-0.267	0.480	$0.698\beta^2 - 1.113\beta + 2.473$
			45	0.615	-0.269	0.311	$8.628\beta^2 - 8.756\beta + 4.216$
			60	0.678	-0.173	0.231	$-1.118\beta^2 + 1.083\beta + 1.874$
Under axial compression in the chord	Chord		30	0.628	-0.266	0.368	$4.369\beta^2 - 5.161\beta + 3.513$
			45	0.571	-0.248	0.282	$1.717\beta^2 - 2.504\beta + 2.885$
			60	0.554	-0.234	0.213	$0.507\beta^2 - 1.179\beta + 2.546$
Under	Chord		30	0.671	-0.286	0.458	$2.605\beta^2 - 3.367\beta + 3.083$

in-plane		45	0.605	-0.262	0.357	$2.140\beta^2 - 2.607\beta + 2.837$
bending						
in the chord		60	0.583	-0.249	0.278	$0.294\beta^2 - 0.697\beta + 2.373$

For the CFST K-joints with other θ-value, the SCF formula is assumed as shown in **Eq. (5.3)**.

$$\mathrm{SCF}_\theta = A\theta^2 + B\theta + C \qquad (5.3)$$

The coefficients A, B and C in **Eq. (5.3)** can be obtained for each combination of β-, γ-, τ-values using the SCF$_{\mathrm{FEA}}$ values for $\theta = 30°$, $45°$ and $60°$ as SCF$_\theta$.

By assuming the coefficients A, B and C in **Eq. (5.3)** as the ternary linear equations in terms of SCF$_{30}$, SCF$_{45}$ and SCF$_{60}$, where SCF$_{30}$, SCF$_{45}$ and SCF$_{60}$ are the SCF value under $\theta = 30°$, $45°$ and $60°$, respectively, **Eq. (5.4)** has been obtained.

$$
\begin{aligned}
A &= \frac{\mathrm{SCF}_{60} - 2\mathrm{SCF}_{45} + \mathrm{SCF}_{30}}{450} \\
B &= \frac{-5\mathrm{SCF}_{60} + 12\mathrm{SCF}_{45} - 7\mathrm{SCF}_{30}}{30} \\
C &= 3\mathrm{SCF}_{60} - 8\mathrm{SCF}_{45} + 6\mathrm{SCF}_{30}
\end{aligned}
\qquad (5.4)
$$

The validity ranges of these proposed parametric formulae are $0.3 \leq \beta \leq 0.6$, $40 \leq 2\gamma \leq 80$, $0.4 \leq \tau \leq 1.0$ and $30° \leq \theta \leq 60°$ since the validity of the parametric formulae has been confirmed only for those ranges.

5.4.2 Accuracy verification

SCFs obtained using the proposed formulae in **Eq. (5.2)** and **Table 5.10**, SCF$_{\mathrm{FOR}}$, were compared with those by FE analysis, SCF$_{\mathrm{FEA}}$, for all locations to verify the accuracy of the parametric formulae for the cases with θ-values of $30°$, $45°$ and $60°$. The results are shown in **Fig. 5.13**. Also shown in the figures are statistical measures of the ratio SCF$_{\mathrm{FOR}}$/SCF$_{\mathrm{FEA}}$. Overall, there is good agreement between the two sets of SCFs. The mean values of SCF$_{\mathrm{FOR}}$/SCF$_{\mathrm{FEA}}$ listed in **Fig. 5.13** are very close to 1.0 for all locations, and the corresponding coefficients of variance (COV) are relatively small.

The parametric formulae for SCF$_\theta$ shown in **Eqs. (5.3)** and **(5.4)** were verified using FEA results of 32 models with other θ-values in **Table 5.4**, for all locations. The comparisons for all loading conditions are shown in **Fig. 5.14**, which shows a good

agreement between SCF$_{FOR}$ and SCF$_{FEA}$.

Therefore, it can be concluded that the proposed SCF formulae have sufficient accuracy and reliability for CFST K-joints under three loading conditions in this chapter.
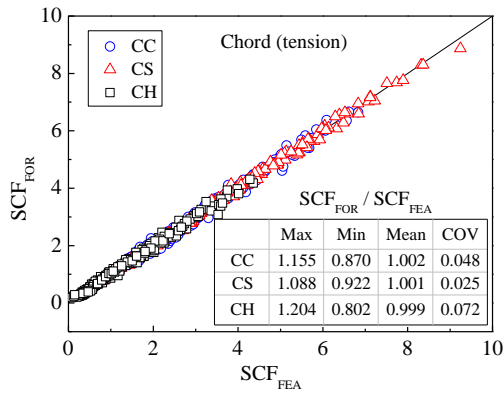
(a) Chord (tension) under basic balanced axial forces
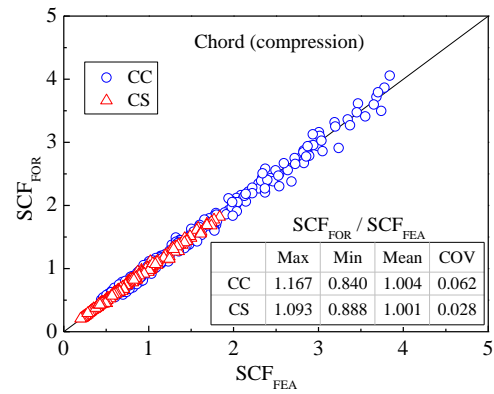
(b) Brace (tension) under basic balanced axial forces
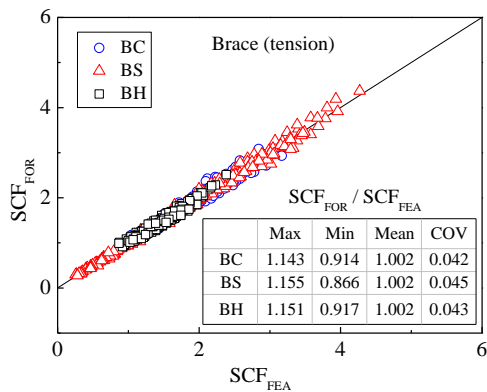
(c) Chord (compression) under basic balanced axial forces
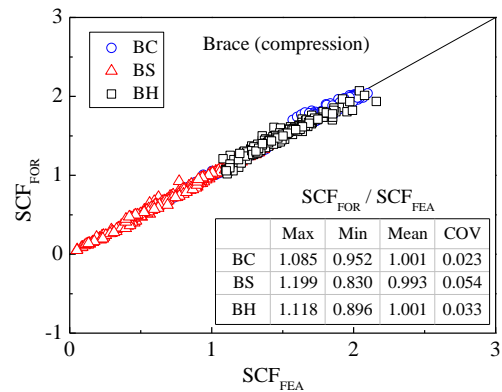
(d) Brace (compression) under basic balanced axial forces
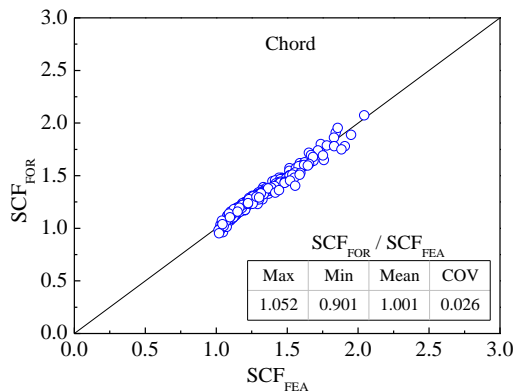
(e) Chord under axial compressive force in the chord
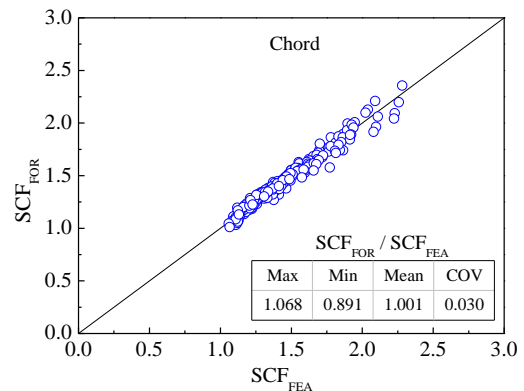
(f) Chord under in-plane bending in the chord

Fig. 5.13 Comparison of SCF$_{FOR}$ with SCF$_{FEA}$ under $\theta = 30°$, $45°$ and $60°$
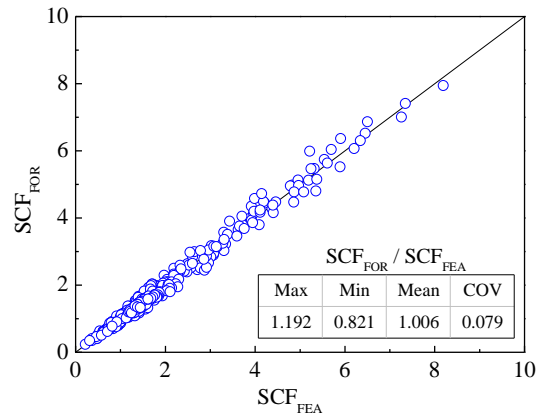
Fig. 5.14 Comparison of SCF$_{FOR}$ with SCF$_{FEA}$ under other θ-values

5.5 Summary

A case-based analysis was carried out firstly by employing the local CFST K-joint in a half-through CFST trussed arch bridge under the loading of a fatigue vehicle. An extensive parametric analysis on the basis of the validated FE model was performed to reveal the effects of the key four geometric parameters β, 2γ, τ and θ on the stress concentration factors (SCFs). According to the results from 816 FE analyses, a series of parametric formulae were proposed to determine the SCFs of CFST K-joints. The main conclusions are summarized as follows.

(1) Based on the results of case-based analysis, the maximum SCFs of CFST K-joint are much smaller than those of CHS K-joint, especially around compressive brace. The influence of β on SCFs is the most significant and that of γ is minimal among the five parameters (β, 2γ, τ, θ and ρ) considered in the analysis.

(2) Under basic balance axial forces, the SCFs around the intersection in tension are much larger than those in compression. In the chord around the intersection with the tensile brace, the hot spot is mainly located at either the crown toe or saddle. In the chord around the intersection with the compressive brace, the hot spot always locates at the crown toe. In the tensile brace, the hot spot locations vary depending on the joint parameters, although the crown toe or saddle is often the hot spot. In the compressive brace, the hot spot is mainly located at either the crown toe or crown heel.

(3) Under the axial compression or in-plane bending in the chord, the hot spot in the chord locates at either crown toe or crown heel, but mainly at crown heel, and their SCFs

are very close.

(4) Parametric SCF formulae including the four key geometric parameters were proposed for CFST K-joints under three loading conditions with sufficient accuracy and reliability.

CHAPTER 6

Concluding Remarks and Future Works

6.1 Concluding remarks

The purpose of this dissertation was to do the study on the stress concentration factors (SCFs) in terms of hot spot stress (HSS) for the concrete-filled steel tubular (CFST) T- and K-joints. Geometric parameters statistics of CFST K-joints in China, validation of numerical replication for the experimental studies on SCFs of CFST T- and K-joints, and formulation of SCFs for CFST T-joints under various loading conditions were conducted. The main findings obtained in this dissertation are summarized as follows.

Firstly, the geometric parameters statistics of CFST K-joints were collected and analyzed using literature review and website investigation. The main findings of this work can be summarized as follows.

(1) CFST K-joints were adopted in CFST trussed arch bridges. The arch ribs can be categorized into four-limbs, transverse dumbbell, two-limbs, three-limbs and six-limbs. Four-limbs and transverse dumbbell are mainly used in CFST trussed arch bridges, which account for 83.2% of the total bridges.

(2) The structural types of CFST K-joints include that full penetration welded CFST K-joint, gusset plate bolted CFST K-joint and full penetration welded CFST K-joint with inner headed studs. Full penetration welded CFST K-joint accounts for 95.8% of the total bridges, which was regarded as the object of statistics.

(3) The practical ranges of β-, 2γ-, τ-, θ- and ρ-values are [0.3, 0.6], [40, 80], [0.4, 1.0], [30°, 60°] and [-0.55, +0.25], respectively.

Secondly, the validity of the developed finite element (FE) models to determine the SCFs of CFST T-joints and the principle strain distribution around the intersection of CFST K-joints was evaluated by comparison with the existing experimental results. The main findings of this work can be summarized as follow.

(1) Since the measured HSS was much lower than yield stress in the experiment, the linear elastic analysis in terms of material properties in FE analysis was conducted to determine the HSS of CFST T- and K-joints.

(2) The linear full-integration eight-node hexahedron solid element was used for the whole model, i.e. steel tube, concrete and weld bead.

(3) The mesh size of approximately 2 mm was adopted for the elements around the

chord-brace intersection. The number of element layers in the tube thickness direction were determined so that the edge length ratio of elements around the intersection is approximately 1.

(4) "Touch" function with the friction coefficient ($\mu = 0.3$) between concrete and steel was adopted to simulate the interface behavior between chord tube and concrete, which allows contact bodies to touch and separate each other in normal direction, and slide with the friction behavior in tangential direction.

(5) The HSS around the chord-brace intersection was obtained numerically by linear extrapolation, the positions of two nodes for HSS calculation of 1st and 2nd nodes are determined based on the specification in CIDECT Design Guide.

Thirdly, it focuses on the SCFs of CFST T-joints under six loading conditions, i.e. axial tension in the brace; axial compression in the brace; in-plane bending (IPB) in the brace; out-of-plane bending (OPB) in the brace; axial compression in the chord; IPB in the chord. Parametric analysis was conducted by using the validated FE model to reveal the effects of the key four non-dimensional geometric parameters (β, 2γ, τ and α) on the SCFs. Based on the numerical results from 424 FE analyses, a series of parametric formulae were proposed to determine the SCFs of CFST T-joints. The main findings are summarized as follows.

(1) The influences of non-dimensional geometric parameters (β, 2γ, τ and α) on SCFs of CFST T-joints under six loading conditions have been revealed. Moreover, the influence of τ on the SCFs is generally larger than that of β, 2γ and α in most cases.

(2) The SCFs in the chord caused by axial tension in the brace are much larger than that under axial compression in the brace. The maximum SCFs in the chord generally occur at locations CS and CC under axial tensile and compressive force, respectively. The maximum SCFs in the brace occur at location BS under axial tensile force in general. However, they can occur at locations BS or BC under axial compressive force.

(3) The SCFs along the intersection of tensile side under in-plane or out-of-plane bending in the brace are in general much larger than that on compressive side. The maximum SCFs under in-plane and out-of-plane bending in the brace usually occur at locations CC and CS both on tensile side, respectively. Under the axial compressive force or in-plane bending in the chord, they usually occur at location CC.

(4) Using multiple regression analysis, parametric formulae to determine the SCFs

for CFST T-joints under six loading conditions were developed. Sufficient accuracy and reliability of the proposed formulae were demonstrated by comparison with FE analysis results.

Fourthly, a case-based analysis was carried out firstly by employing the local CFST K-joint in a half-through CFST trussed arch bridge under the loading of a fatigue vehicle. An extensive parametric analysis on the basis of the validated FE model was performed to reveal the effects of the key four geometric parameters β, 2γ, τ and θ on the stress concentration factors (SCFs). According to the results from 816 FE analyses, a series of parametric formulae were proposed to determine the SCFs of CFST K-joints. The main conclusions are summarized as follows.

(1) Based on the results of case-based analysis, the maximum SCFs of CFST K-joint are much smaller than those of CHS K-joint, especially around compressive brace. The influence of β on SCFs is the most significant and that of γ is minimal among the five parameters (β, 2γ, τ, θ and ρ) considered in the analysis.

(2) Under basic balance axial forces, the SCFs around the intersection in tension are much larger than those in compression. In the chord around the intersection with the tensile brace, the hot spot is mainly located at either the crown toe or saddle. In the chord around the intersection with the compressive brace, the hot spot always locates at the crown toe. In the tensile brace, the hot spot locations vary depending on the joint parameters, although the crown toe or saddle is often the hot spot. In the compressive brace, the hot spot is mainly located at either the crown toe or crown heel.

(3) Under the axial compression or in-plane bending in the chord, the hot spot in the chord locates at either crown toe or crown heel, but mainly at crown heel, and their SCFs are very close.

(4) Parametric SCF formulae including the four key geometric parameters were proposed for CFST K-joints under three loading conditions with sufficient accuracy and reliability.

6.2 Future works

The study in this dissertation has certain deficiencies and needs enhancement through the future work. Some ideas to be done in the future work can be listed as follows.

(1) The validity range of each parameter for the SCF formulae of CFST T- and K-

joints was set to the same as that in the parametric analysis. Examination of the applicability of the parametric formulae for wider range of the parameters can be one of the future work.

(2) Examination of the applicability of the developed FE modeling in this study for CFST Y- and N-joints will be conducted for the formulation of the corresponding SCFs with sufficient accuracy and reliability.

(3) Static and fatigue experiments of CFST joints will be conducted to reveal the general tendency of crack initiation and growth in fatigue process. Finally, S-N curves and fatigue calculation method of CFST joints with common K-type, T-type, Y-type and N-type will be proposed.

References

[1] Chen BC, Wang TL. Overview of concrete filled steel tube arch bridges in China. Practice Periodical on Structural Design and Construction 2009; 14(2): 70-80.

[2] Chen BC, Wei JG, Zhou J and Liu JP. Application of Concrete-filled Steel Tube Arch Bridges in China: Current Status and Prospects. China Civil Engineering Journal 2017; 50(6): 50-61 [in Chinese].

[3] Han LH, Li W, Bjorhovde R. Developments and advanced applications of concrete-filled steel tubular (CFST) structures: Members. Journal of Constructional Steel Research 2014; 100: 211-228.

[4] Wang Q, Nakamura S, Chen KM, Chen BC and Wu QX. Comparison between steel and concrete-filled steel tubular arch bridges in China. Proceedings of Constructional Steel, Japanese Society of Steel Construction 2016; 24: 66-73.

[5] Wang Q, Nakamura S, Chen KM, Chen BC and Wu QX. Fatigue evaluation of K-joint in a half-through concrete-filled steel tubular trussed arch bridge in china by hot spot stress method. Proceedings of Constructional Steel, Japanese Society of Steel Construction 2016; 24: 633-640.

[6] Diao Y. Experimental research on fatigue performance of tubular joints in concrete-filled steel bridge. Ph.D. thesis, Southwest Jiaotong University, Chengdu, China; 2012 [in Chinese].

[7] JTG/T D65-06-2015. Specifications for design of highway concrete-filled steel tubular arch bridge. China Communication Press, Beijing, China, 2015 [in Chinese].

[8] Kuang JG, Potvin AB, Leick RD. Stress concentration in tubular joints. Proceedings of the Seventh Annual Offshore Technology Conference, OTC 2205. Houston, Texas, 1975; 593-612.

[9] Efthymiou M, Durkin S. Stress concentrations in T/Y and gap/overlap K-joints. Behavior of Offshore Structures: Proceedings of the 4th International Conference on Behavior of Offshore Structures. Amsterdam: Elsevier 1985; 429-440.

[10] Hellier AK, Connolly MP, Dover WD. Stress concentration factors for tubular Y-and T-joints. International Journal of Fatigue 1990; 12(1): 13-23.

[11] Smedley PA, Fisher PJ. Stress concentration factors for simple tubular joints. Proceedings of the First International Offshore and Polar Engineering Conference.

International Society of Offshore and Polar Engineers, Edinburgh, UK, 1991; 475-483.

[12] Mashiri FR, Zhao XL, Grundy P. Stress concentration factors and fatigue behaviour of welded thin-walled CHS–SHS T-joints under in-plane bending. Engineering Structures 2004; 26(13): 1861-1875.

[13] Zhao XL, Wilkinson T, Hancock GJ. Cold-formed tubular members and connections: Structural behaviour and design. Elsevier, Oxford, UK, 2005.

[14] Zhao XL, Herion S, Packer JA, Puthli R, Sedlacek G, Wardenier J. et al. Design guide for circular and rectangular hollow section joints under fatigue loading, CIDECT, TUV; 2000.

[15] Hobbacher A. Recommendations for fatigue design of welded joints and components. New York: Welding Research Council; 2009.

[16] API. American Petroleum Institute. Recommended practice for planning, designing and constructing fixed offshore platforms. 21th Ed., API Publishing Services, Washington DC, 2014.

[17] AWS. American Welding Society. Structural welding code-steel. AWS D1.1/1.1M. American Welding Society, Inc., Miami; 2004.

[18] ABS. American Bureau of Shipping. Guide for buckling and ultimate strength assessment for offshore structures. American Bureau of Shipping, Houston; 2004.

[19] DNV. DNV recommended practice RP-C203. Fatigue strength analysis of offshore of steel structures. Det Norske Veritas, Norway; 2010.

[20] SAA. Steel structures, Australian standard AS 4100-1998. Sydney, Australia: Standards Association of Australia; 1998.

[21] JSSC. Japanese Society of Steel Construction. Fatigue design recommendations for steel structures. Gihodoshuppan Press, Tokyo, Japan; 2012 [in Japanese].

[22] Liu YJ, Jiang L, Wang KN. Review of fatigue behavior in welded tubular joints. Journal of Architecture and Civil Engineering 2017; 34(5): 1-20 [in Chinese].

[23] Niemi E (ed.). Stress determination for fatigue analysis of welded components. Woodhead Publishing; 1995.

[24] Saini DS, Karmakar D, Ray-Chaudhuri S. A review of stress concentration factors in tubular and non-tubular joints for design of offshore installations. Journal of Ocean Engineering and Science 2016; 1(3): 186-202.

[25] Gurney TR. A re-analysis of fatigue data for welding joints in steel. Welding Research International 1973; 3: 1-54.

[26] Olivier R, Ritter D. Catalogue of *S-N* curves of welded joints in structural steel. Dusseldorf: DVS-Verlag, 1979.

[27] Van Wingerde AM. The fatigue behaviour of T-and X-joints made of square hollow sections. HERON 1992; 37 (2): 1-182.

[28] Romeijn A. Stress and strain concentration factors of welded multiplanar tubular joints. Ph.D. Thesis, Delft, The Netherlands; 1994.

[29] Fricke W. Evaluation of hot spot stresses in complex welded structures. Proceedings of the IIW Fatigue Seminar. Tokyo Institute of Technology, Tokyo, Japan; 2002: 165-176.

[30] Department of Energy (DEn). Offshore installations: Guidance on design and construction. HMSO, London, UK; 1984.

[31] EC3, Eurocode 3: Design of steel structures-Part 1-1: General rules and rules for buildings. European Committee for Standardisation (CEN), London, UK; 2005.

[32] Marshall PW. Design of welded tubular connections: basis and use of AWS code provisions. Elsevier Science Publishers, Amsterdam, The Netherlands; 2013.

[33] Romeijn A, Puthli RS, De Koning CHM, Wardenier J. Stress and strain concentration factors of multiplanar joints made of circular hollow sections. The Second International Offshore and Polar Engineering Conference, San Francisco, USA; 1992.

[34] Zheng HZ. The fatigue behavior and design method of CHS-SHS welded joints. Ph.D. thesis, Tongji University, Shanghai, China; 2008 [in Chinese].

[35] Sonsino CM, Fricke W, De Bruyne F, et al. Notch stress concepts for the fatigue assessment of welded joints — Background and applications. International Journal of Fatigue 2012; 34(1): 2-16.

[36] Fischer C, Fricke W, Rizzo CM, Review of the fatigue strength of welded joints based on the notch stress intensity factor and SED approaches. International Journal of Fatigue 2016; 84: 59-66.

[37] Schijve J. Fatigue predictions of welded joints and the effective notch stress concept. International Journal of Fatigue 2012; 45: 31-38.

[38] Radaj D, Sonsino CM, Flade D. Prediction of service fatigue strength of a welded tubular joint on the basic of the notch strain approach. International Journal of Fatigue

1998; 20(6): 471-480.

[39] Maddox, SJ. Fatigue strength of welded structures. Woodhead Publishing, 2014.

[40] Tanaka S, Kawahara T, Okada H. Study on crack propagation simulation of surface crack in welded joint structure. Marine Structures 2014; 39: 315-334.

[41] Chen Tao, Xiao ZG, Zhao XL, et al. A boundary element analysis of fatigue crack growth for welded connections under bending. Engineering Fracture Mechanics 2013; 98: 44-51.

[42] Yang ZM, Lie ST, Gho WM. Fatigue crack growth analysis of a square hollow section T-joint. Journal of Constructional Steel Research 2007; 63(9): 1184-1193.

[43] Paris P, Erdogan F. A critical analysis of crack propagation laws. Journal of Basic Engineering 1963; 85(4): 528-533.

[44] Toprac AA, Beale AA. Analysis of in-plane T, Y and K welded tubular connections. Welding Research Council 1967; 125:1.

[45] Saini DS, Karmakar D, Ray-Chaudhuri S. A review of stress concentration factors in tubular and non-tubular joints for design of offshore installations. Journal of Ocean Engineering and Science 2016; 1(3): 186-202.

[46] Kuang JG, Potvin AB, Leick RD, et al. Stress concentration in tubular joints. Society of Petroleum Engineers Journal 1977; 17(4): 287-299.

[47] Wordsworth AC, Smedley GP. Stress concentrations at unstiffened tubular joints. In European Offshore Steels Research Seminar 1978, Volume IX/P31: 1-7.

[48] Wordsworth AC. Stress concentration factors at K and KT tubular joints. In Conference on Fatigue in Offshore Structural Steel, I.C.E, London, UK, 1981.

[49] Dijkstra OD, Van Foeken RJ, Romeijn A, et al. Fatigue design guide for circular and rectangular hollow section multiple joints. Delft University of Technology, The Netherlands, 1996.

[50] Karamanos SA, Romeijn A, Wardenier J. Stress concentrations and joint flexibility effects in multi-planar welded tubular connections for fatigue design. Stevin report 6-98-05, CIDECT report 7R-17/98. Delft University of Technology, The Netherlands, 1997.

[51] Karamanos SA, Romeijn A, Wardenier J. Stress concentrations in tubular gap K-joints: mechanics and fatigue design. Engineering Structures 2000; 22(1): 4-14.

[52] Hellier AK, Connolly MP, Kare RF, Dover WD. Prediction of the stress distribution in tubular Y-and T-joints. International Journal of Fatigue 1990, 12(1): 25-33.

[53] Chang E, Dover WD. Stress concentration factor parametric equations for tubular X and DT joints. International Journal of Fatigue 1996, 18(6): 363-387.

[54] Chang E, Dover WD. Prediction of stress distributions along the intersection of tubular Y and T-joints. International Journal of Fatigue 1999, 21(4): 361-381.

[55] Morgan MR, Lee MMK. New parametric equations for stress concentration factors in tubular K-joints under balanced axial loading. International Journal of Fatigue 1997, 19(4): 309-317.

[56] Morgan MR, Lee MMK. Prediction of stress concentrations and degrees of bending in axially loaded tubular K-joints. Journal of Constructional Steel Research 1998, 45(1): 67-97.

[57] Van Wingerde AM, Packer JA, Wardenier J. New guidelines for fatigue design of HSS connections. Journal of Structural Engineering 1996; 122(2): 125-132.

[58] Van Wingerde AM, Packer JA, Wardenier J. Simplified SCF formulae and graphs for CHS and RHS K-and KK-connections. Journal of Constructional Steel Research 2001, 57(3): 221-252.

[59] Chiew SP, Soh CK, Wu NW. General SCF design equations for steel multiplanar tubular XX-joints. International Journal of Fatigue 2000; 22(4): 283-293.

[60] Gho WM, Fung TC, Soh CK. Stress and strain concentration factors of completely overlapped tubular K (N) joints. Journal of Structural Engineering 2003; 129(1): 21-29.

[61] Shao YB, Du ZF, Lie ST. Prediction of hot spot stress distribution for tubular K-joints under basic loadings. Journal of Constructional Steel Research 2009; 65(10-11): 2011-2026.

[62] Puthli R, Herion S. Stress concentration and secondary moment distribution in RHS joints for fatigue design. University of Karlsruhe, Germany, 1996.

[63] Gandhi P, Berge S.. Fatigue behavior of T-joints: square chords and circular braces. Journal of Structural Engineering 1998; 124(4): 399-404.

[64] Bian LC, Lim JK, Kim YJ. Fatigue strength and fracture behaviour of CHS-to-RHS T-joints subjected to out-of-plane bending. KSME International Journal 2003; 17(2): 207-214.

[65] Bian LC, Lim JK. Fatigue strength and stress concentration factors of CHS-to-RHS T-joints. Journal of Constructional Steel Research 2003; 59(5): 627-640.

[66] Mashiri FR, Zhao XL, Grundy P. Stress concentration factors and fatigue behaviour of welded thin-walled CHS-RHS T-joints under in-plane bending. Engineering Structures 2004; 26(13): 1861-1875.

[67] Tong LW, Zheng HZ, Mashiri FR, Zhao XL. Stress-concentration factors in circular hollow section and square hollow section T-connections: experiments, finite-element analysis, and formulas. Journal of Structural Engineering 2012; 139(11): 1866-1881.

[68] Yin Y, Liu XF, Lei P, Zhou L. Stress concentration factor for tubular CHS-to-RHS Y-joints under axial loads. Journal of Constructional Steel Research 2018; 148: 768-778.

[69] Cheng B, Qian Q. Study on stress concentration characteristics of square bird-beak square-hollow-section T-joints. China Civil Engineering Journal 2015; 48(5):1-10 [in Chinese].

[70] Cheng B, Qian Q, Zhao XL. Numerical investigation on stress concentration factors of square bird-beak SHS T-joints subject to axial forces. Thin-Walled Structures 2015; 94: 435-445.

[71] Cheng B, Qian Q, Zhao XL. Stress concentration factors and fatigue behavior of square bird-beak SHS T-joints under out-of-plane bending. Engineering Structures 2015; 99: 677-684.

[72] Tong LW, Xu GW, Yan DQ, Zhao XL. Fatigue tests and design of diamond bird-beak SHS T-joints under axial loading in brace. Journal of Constructional Steel Research 2016; 118: 49-59.

[73] Tong LW, Fu YG, Liu YQ, Zhao XL. Stress concentration factors of diamond bird-beak SHS T-joints under brace loading. Thin-Walled Structures 2014; 74: 201-212.

[74] Tong LW, Xu GW, Liu YQ, Yan DQ, Zhao, XL. Finite element analysis and formulae for stress concentration factors of diamond bird-beak SHS T-joints. Thin-Walled Structures 2015; 86: 108-120.

[75] Tong LW, Sun CQ, Chen YY, Zhao XL, Shen B and Liu CB. Experimental comparison in hot spot stress between CFCHS and CHS K-joints with gap. Proceedings of 12th International Symposium on Tubular Structures 2008; 389-395.

[76] Mashiri FR, Zhao XL. Square hollow section (SHS) T-joints with concrete-filled chords subjected to in-plane fatigue loading in the brace. Thin-Walled Structures 2010; 48(2): 150-158.

[77] Wang K, Tong LW, Zhu J, Zhao XL, Mashiri FR. Fatigue behavior of welded T-joints with a CHS brace and CFCHS chord under axial loading in the brace. Journal of Bridge Engineering 2011; 18(2): 142-152.

[78] Wang K. Study on the hot spot stress and fatigue strength of welded circular hollow section (CHS) T-joints with concrete-filled chords. Ph.D. thesis, Tongji University, Shanghai, China, 2008 [in Chinese].

[79] Chen J, Chen J, Jin WL. Experiment investigation of stress concentration factor of concrete-filled tubular T joints. Journal of Constructional Steel Research 2010; 66(12): 1510-1515.

[80] Chen J. Experimental and theoretical study of dynamic performance of concrete-filled steel tubular T-joints. Ph.D. thesis, Zhejiang University, Hangzhou, China, 2011 [in Chinese].

[81] Xu F, Chen J, Jin WL. Experimental investigation of SCF distribution for thin-walled concrete-filled CHS joints under axial tension loading. Thin-Walled Structures 2015; 93: 149-157.

[82] Udomworarat P, Miki C, Ichikawa A, Sasaki E, Sakamoto T, Mitsuki K, Hasaka T. Fatigue and ultimate strengths of concrete filled tubular K-joints on truss girder. JSCE Journal Structural Engineering 2000; 46(3): 1627–1635.

[83] Udomworarat P, Miki C, Ichikawa A, Sasaki E, Komechi M, Mitsuki K, Hosaka T. Fatigue performance of composite tubular K-joints for truss type bridge. JSCE Structural Engineering/Earthquake Engineering 2002; 19(2): 65s–79s.

[84] Huang WJ, Fenu L, Chen BC, Briseghella B. Experimental study on K-joints of concrete-filled steel tubular truss structures. Journal of Constructional Steel Research 2015; 107: 182–193.

[85] Kim IG, Chung CH, Shim CS, Kim YJ. Stress concentration factors of N-joints of concrete-filled tubes subjected to axial loads. International Journal of Steel Structures 2014; 14(1): 1–11.

[86] Liu YJ, Xiong ZH, Feng YC, Jiang L. Concrete-filled rectangular hollow section X joint with Perfobond Leister rib structural performance study: Ultimate and fatigue experimental Investigation. Steel and Composite Structures 2017; 24(4): 455–465.

[87] Tong LW, Wang K, Shi WZ, et al. Experimental study on hot spot stress of welded concrete filled CHS T-joints. Journal of Tongji University: Natural Science 2010;

38(3): 329-334 [in Chinese].

[88] Gu M, Tong LW, Zhao XL, Zhang YF. Numerical Analysis of Fatigue Behavior of Welded CFCHST-Joints. Advanced Steel Construction 2014; 10(4): 476-497.

[89] Droogne D. The influence of concrete filling on the fatigue behaviour of tubular steel bridge joints. Master thesis, Ghent University, Ghent, Belgium, 2015.

[90] Jardine B. Fatigue life enhancement of tubular joints by grout injection. Offshore Technology Report-Health and Safety Executive OTH, 1993.

[91] Musa IA, Mashiri FR, Zhu XQ. Parametric study and equation of the maximum SCF for concrete filled steel tubular T-joints under axial tension. Thin-Walled Structures 2018; 129: 145-156.

[92] Diao Y, Fan WL. Experimental research on fatigue life tubular joints in concrete-filled steel tube. Building Structure 2013; 43(5): 45-47 [in Chinese].

[93] Cheng G, Liu YJ, Qiu JL, el al. Analysis of stress concentration factor on concrete-filled rectangular steel tube T-joints stiffened with PBL. Journal of Architecture and Civil Engineering 2014; 31(4): 74-79 [in Chinese].

[94] Li HS. The fatigue behavior of welded rectangular concrete-filled steel tubular X-joints. Master thesis, Chang'an University, Xi'an, China, 2017 [in Chinese].

[95] Liu YJ, Jiang L, Xiong ZH, et al. Hot spot SCF computation method of concrete-filled and PBL-stiffened rectangular hollow section joint subjected to axial sections. Journal of Traffic and Transportation Engineering 2017; 17(5): 1-15 [in Chinese].

[96] Chen BC. Concrete filled steel tubular arch bridges (the third edition). China Communications Press, Beijing, China, 2016 [in Chinese].

[97] Chen BC. Concrete filled steel tubular arch bridges. China Communications Press, Beijing, China, 2007 [in Chinese].

[98] Herion S. Multiplanar K-joints made of RHS. Ph.D. thesis, University of Karlsruhe, Germany, 1994 (in German).

[99] Baltay P, Gjelsvik A. Coefficient of friction for steel on concrete at high normal stress. Journal of Materials in Civil Engineering 1990; 2(1): 46-49.

[100] Marc 2013.1, help system. Volume A: Theory and user information. MSC Software Corporation, 2013.

[101] Marc 2013.1, help system. Volume C: Program input. MSC Software Corporation, 2013.

[102] JTG D62-2004. Code for design of highway reinforced concrete and prestressed concrete bridges and culverts. China Communication Press, Beijing, China, 2004 (in Chinese).

[103] Lotsberg I. On stress concentration factors for tubular Y-and T-Joints in frame structures. Marine Structures 2011; 24(1): 60-69.

[104] Schumacher A, Nussbaumer A. Experimental study on the fatigue behaviour of welded tubular K-joints for bridges. Engineering Structures 2006; 28(5): 745–755.

[105] Shao YB. Proposed equations of stress concentration factor (SCF) for gap tubular K-joints subjected to bending load. International Journal of Space Structures 2004; 19(3): 137–147.